Manuscript Details

Manuscript number	ORGEO_2016_536
Title	Fe-Mn oxide indications in the feeder and mound zone of the Jurassic Mn-carbonate ore deposit, Úrkút, Hungary
Article type	Research paper

Abstract

The Úrkút manganese deposit is one of the largest ones in the World, located in the central part of the Transdanubian Range, western Hungary. The deposit is interbedded with Mesozoic limemarlstone. The Fe-Mn-oxide indications of a feeder and mound zone embedded in limemarlstone at the footwall of the Mn-carbonate ore deposit were studied using 45 samples (Úrkút Mine, Shaft III, deep level). Microstructural and textural (optical microscopy, SEM-EDS) observations, mineralogy (XRD-μXRD), and geochemistry (ICP, C and O by IR-MS) were used to characterize the host marlstone and the Fe-Mn oxides of the feeder and mound zone. High-resolution in situ and bulk organic matter analyses were performed for the first time using GC-MS, FTIR-ATR, and Raman spectroscopy. Stromatolite-like, filamentous and coccoid microstuctures built up of Fe-Mn-oxides (ferrihydrite, goethite, manganite, pyrolusite, hollandite, birnessite, hausmannite) and silica occur in the micritic marlstone host rock among common calcite biodebris (microfossils and Echinozoa fragments) and rare detrital clasts (quartz, feldspar). The clay minerals occur as greenish patches in the limemarlstone and show boring traces. The calcite matrix of the limemarlstone and idiomorphic dolomite are authigenic. δ13CPDB values of the carbonate in the host limemarlstone reflect greater organic matter contributions approaching the mineralized areas (0.64 to -21.35‰). Temperature calculation based on δ18OSMOW values of the carbonate, assuming equilibrium conditions, show elevated temperatures toward the mineralized areas (9.93 to 29.87‰). In places, the Mn oxides appear with Fe oxides in laminated, micro-stromatolite-like structures. In these oxide zones, variable kinds of organic compounds occur as intercalated microlaminae identified by FTIR and Raman line-profile analyses as aromatic hydrocarbons. Results indicate that metal-bearing fluids infiltered the unconsolidated micritic limemarl. Fe-oxide enrichment occurred most probably through iron oxidizing microbes under suboxic, neutrophilic conditions, while Mn oxide formed most probably by active surface catalyses. At the sediment/water interface, Fe-Mn-oxide stromatolite mounds (chimneys) formed in rift zones from the discharge of fluids of elevated temperature. The host marl itself may have originated by microbially mediated reactions (clay minerals and calcite micrite).

Keywords	T-OAE, feeder and mound zone, Mn-carbonate ore, Úrkút, geobiomineralization, hydrothermal, failed rift, Fe-Mn-oxide

Corresponding Author	Márta Polgári
Corresponding Author's Institution	Research Center for Astronomy and Earth Sciences, Institute for Geology and Geochemistry, HAS
Order of Authors	Zsombor Molnár, Márta Polgári, James Hein, Sándor Józsa, József Fekete, Ilidkó Gyollai, Krisztián Fintor, Lóránt Bíró, Máté Szabó, Sándor Rapi, Péter Forgó, Tamás Vigh

Suggested reviewers	Barry J. Maynard, Kirsti Loukola-Ruskeeniemi, Barrie R. Bolton, Jan Pasava

Submission Files Included in this PDF

File Name [File Type]

cov_lett.pdf [Cover Letter]

garph_abs.pdf [Graphical Abstract]

MS_160914.docx [Manuscript]

Fig_1.pdf [Figure]

Fig_2.pdf [Figure]

Fig_3.jpg [Figure]

Fig_4.jpg [Figure]

Fig_5.jpg [Figure]

Fig_6.pdf [Figure]

Fig_7.pdf [Figure]

Fig_8.pdf [Figure]

Fig_9.jpg [Figure]

Table_1.docx [Table]

Table_2.docx [Table]

Table_3.docx [Table]

Table_4.docx [Table]

Table_5.docx [Table]

Supp Mat.pdf [e-Component]

Highlights for submission.doc [Highlights]

To view all the submission files, including those not included in the PDF, click on the manuscript title on your EVISE Homepage, then click 'Download zip file'.

COVER LETTER

ORE GEOLOGY REVIEWS

PROFESSOR FRANCO PIRAJNO
Editor in Chief
University of Western Australia,
Crawley, Western Australia, Australia

Dear Editorial Board,

Dear Professor Pirajno,

We would like to submit our manuscript "Fe-Mn oxide indications in the feeder and mound zone of the Jurassic Mn-carbonate ore deposit, Úrkút, Hungary" for publication in Ore Geology Reviews as an original research paper.

List of authors:
Zsombor Molnár, Márta Polgári, James R. Hein, Sándor Józsa, József Fekete, Ildikó Gyollai, Krisztián Fintor, Lóránt Bíró, Máté Szabó, Sándor Rapi, Péter Forgó, Tamás Vigh

The manuscript reviews the main characteristics of the initial Fe-Mn oxide ore indications of the Úrkút Mn-carbonate ore deposit (Alpine-Mediterranean Tethyan Region), where the industrial mining will celebrate its 100th anniversary this year, 2017. The text provides microtextural, mineralogical and geochemical evidence for the fundamental processes of the formation of the initial ore indications, refine the previous model for the origin of this type of black shale-hosted Mn deposit, and discusses the importance of deposit characteristics for the interpretation of deposit genesis.

The authors confirm that the submitted paper contains original, new results, data, and ideas, not previously published or under consideration for publication elsewhere.

The authors confirm that all have been involved with the work, approved the manuscript, and agree to its submission. ZS.M. and M.P. conceived and planned the study, collected samples, made macroscopic descriptions, thin section microscopy, and summarized data, and interpreted the data and wrote the manuscript together with J.R.H., S.J. and T.V.; T.V. guided sample collection and data interpretation as well as L.B. and I.Gy. calculated and interpreted proxies, M. Sz. and I. GY. made XRD, SEM-EDS and FTIR measurement and interpretations,

S.R. and P.F. measured the inorganic chemical composition, K. F. made analysis with Raman-spectroscopy and interpreted these proxies, J.F. measured organic geochemistry, and C, O isotopes of carbonates and organic matter and offered interpretation.

Samples and documentation are deposited in the Archive of the Research Center for Astronomy and Geosciences, Institute for Geology and Geochemistry, Hungarian Academy of Sciences, Budapest.

The authors declare no competing financial interests. Correspondence and requests for materials should be addressed to M.P. (rodokrozit@gmail.com).

Sincerely yours,

Márta Polgári
corresponding author
Research Center for Astronomy and Geosciences
Institute for Geology and Geochemistry
Hungarian Academy of Sciences
Budapest
Budaörsi str. 45.
1112
Hungary
Phone: +36209284650
e-mail: rodokrozit@gmail.com

Fe-Mn oxide indications in the feeder and mound zone of the Jurassic Mn-carbonate ore deposit, Úrkút, Hungary

Proposed complex genetic model for the Úrkút Mn deposit (a), and the Fe-Mn oxide indications of the feeder and mound zone (b)

Legend

I. Proximal feeder zone (Csárdahegy)
II. Distal feeder zone
III. Zone of distal enzymatic Mn(II) oxidation
1.) Dissolved limemarlstone footwall with sedimentary dikes, and metalliferous clay minerals above Mn-oxide infiltrated limestone (black).
2.) Proximal cherty, Fe-rich Mn oxide blocks (high Ba and Sr content) in metalliferous clay mineral assemblage.
3.) Flourishing microbial system, sequestration of metals in the form of oxides (proto-ore), selective enrichment of elements.
4.) Distal accumulation of MnOOH and FeOOH proto-ore, green clay minerals (celadonite), organic matter
5.) Mn nodules, Fe- and Mn-encrustations, hard grounds.

General key

6.) Triassic shallow platform.
7.) Lower-Middle Liassic limestone (a) and limemarlstone (b), shallow marine pelagic sequence.
8.) Submarine (a) and terrestrial (b) volcanic activity in distal areas.
9.) Bioherms.
10.) Biodebris (*Ammonites*), *Brachiopoda*, *Mollusca*, *Crinoidea*, *Echinoidea*, *Porifera*, *Ostracoda*, fish, etc.).
11.) Plankton organisms (*Radiolaria, Foraminifera, Bositra*, etc.).
12.) Resedimentation.
A. Considerable bioproductivity on the seafloor
B. Hydrothermal diffuse discharge system of elevated temperature effecting the unconsolidated sediment, resulting Fe and Mn oxide indication (feeder and mound zone)
C. Diagenesis
Arrows show the direction of energy and ore forming fluid input.

Modified after Polgári et al. (2004); not to scale

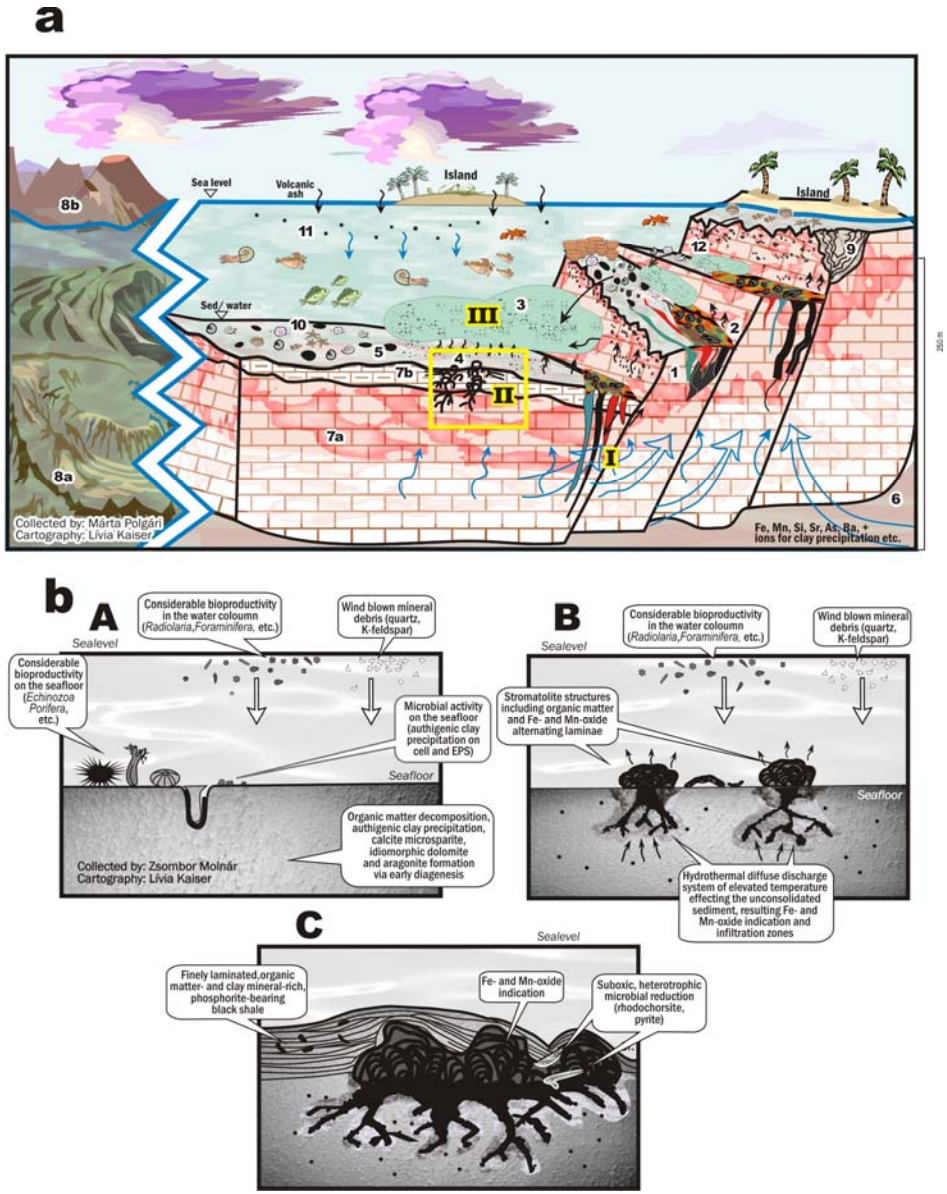

Fe-Mn oxide indications in the feeder and mound zone of the Jurassic Mn-carbonate ore deposit, Úrkút, Hungary

Zsombor Molnár[1], Márta Polgári[2,3*], James R. Hein[4], Sándor Józsa[1], József Fekete[2], Ildikó Gyollai[2], Krisztián Fintor[5], Lóránt Bíró[2], Máté Szabó[2], Sándor Rapi[6], Péter Forgó[7], Tamás Vigh[8]

[1]*Eötvös University, Dept. Petrology and Geochemistry, 1117 Budapest, Pázmány P. s. 1/c, Hungary, e-mail: molnarzs1994@gmail.com*
[2]*Research Center for Astronomy and Geosciences, Geobiomineralization and Astrobiological Research Group, Institute for Geology and Geochemistry, Hungarian Academy of Sciences, 1112 Budapest, Budaörsi út. 45, Hungary, e-mail: rodokrozit@gmail.com*
[3]*Eszterházy Károly University, Dept. of Natural Geography and Geoinformatics, 3300 Eger, Leányka str. 6/C, Hungary*
[4]*USGS, 2885 Mission St., Santa Cruz, CA 95060, U.S.A., jhein@usgs.gov*
[5]*Szeged University, Dept. of Mineralogy, Geochemistry and Petrology, 6722 Szeged, Egyetem, str. 2-6, Hungary, e-mail: efkrisz@gmail.com*
[6]*Eszterházy Károly University, Regional Research Centre, 3300 Eger, Leányka str. 6/G, Hungary, e-mail: raps@ektf.hu*
[7]*Eszterházy Károly University, Food Science Institute, 3300 Eger, Leányka Str. 6, Hungary, e-mail: forgop@ektf.hu*
[8]*Mangán Ltd, Úrkút, Külterület 1. 8409 Hungary, e-mail: manganvigh@gmail.com*

**corresponding authors:*
rodokrozit@gmail.com

Abstract. (**329 words**)

The Úrkút manganese deposit is one of the largest ones in the World, located in the central part of the Transdanubian Range, western Hungary. The deposit is interbedded with Mesozoic limemarlstone. The Fe-Mn-oxide indications of a feeder and mound zone embedded in limemarlstone at the footwall of the Mn-carbonate ore deposit were studied using 45 samples (Úrkút Mine, Shaft III, deep level). Microstructural and textural (optical microscopy, SEM-EDS) observations, mineralogy (XRD-μXRD), and geochemistry (ICP, C and O by IR-MS) were used to characterize the host marlstone and the Fe-Mn oxides of the feeder and mound zone. High-resolution *in situ* and bulk organic matter analyses were performed for the first time using GC-MS, FTIR-ATR, and Raman spectroscopy. Stromatolite-like, filamentous and coccoid microstuctures built up of Fe-Mn-oxides (ferrihydrite, goethite, manganite, pyrolusite, hollandite, birnessite, hausmannite) and silica occur in the micritic marlstone host rock among common calcite biodebris (microfossils and *Echinozoa* fragments) and rare detrital clasts (quartz, feldspar). The clay minerals occur as greenish patches in the limemarlstone and show boring traces. The calcite matrix of the limemarlstone and idiomorphic dolomite are authigenic. $\delta^{13}C_{PDB}$ values of the carbonate in the host limemarlstone reflect greater organic matter contributions approaching the mineralized areas (0.64 to -21.35‰). Temperature calculation based on $\delta^{18}O_{SMOW}$ values of the carbonate, assuming equilibrium conditions, show elevated temperatures toward the mineralized areas (9.93 to 29.87‰). In places, the Mn oxides appear with Fe oxides in laminated, micro-stromatolite-like structures. In these oxide zones, variable kinds of organic compounds occur as intercalated microlaminae identified by FTIR and Raman line-profile analyses as aromatic hydrocarbons. Results indicate that metal-bearing fluids infiltered the

unconsolidated micritic limemarl. Fe-oxide enrichment occurred most probably through iron oxidizing microbes under suboxic, neutrophilic conditions, while Mn oxide formed most probably by active surface catalyses. At the sediment/water interface, Fe-Mn-oxide stromatolite mounds (chimneys) formed in rift zones from the discharge of fluids of elevated temperature. The host marl itself may have originated by microbially mediated reactions (clay minerals and calcite micrite).

Keywords: T-OAE, feeder and mound zone, Mn-carbonate ore, Úrkút, geobiomineralization, hydrothermal, failed rift, Fe-Mn-oxide

Highlights mandatory

- We studied Fe-Mn-oxide of feeder and mound zone of footwall of Úrkút Mn ore deposite.
- Bulk organic matter analysed first time using GC-MS, FTIR-ATR and Raman spectroscopy.
- Metal-bearing fluids infiltered the unconsolidated micritic limemarl.
- Mn oxides appear with Fe oxides in laminated, micro-stromatolite-like structures.

1 **Introduction**

Formation of sedimentary Mn deposits covers vast time and space in Earth's history (Roy, 1981). The Jurassic (Toarcian) was an important time of Mn-carbonate mineralization and different ideas about the controls on deposit formation have been suggested, including tectonic activity, volcanism, climatic variations, and combinations of those. Mn-carbonate deposits are typically associated with organic carbon-rich beds (Roy, 1981). Stratiform black shale-hosted Mn-carbonate deposits reached maximum development during the Toarcian *tenuicostatum-falciferum* ammonite zones. The important Úrkút deposit is among the 10 largest Mn deposits of its type with current reserves of 80 million tons of Mn-carbonate ore (24 wt. % average Mn and 10 wt. % Fe). The Mn ore-bearing Úrkút black shale (gray shale) reflects different conditions of formation compared to epicontinental sea occurrences (Polgári et al., 2016ab). During the past 100 years, numerous papers addressed the complex formation of the Jurassic black shale-hosted manganese carbonate ore at Úrkút. The ore beds are now thought to have resulted from a two-step, microbially mediated process that generated a microbialite (Polgári et al., 2012ab, 2013, 2016a).

Formulation of models to understand ancient Mn-carbonates hosted in black shale is difficult, even for unmetamorphosed deposits, because of the overprinting effect of different microbially mediated early-diagenetic processes. The Mn-carbonate ore assemblage, its black shale host and the proximal cherty Fe-Mn-oxide type feeder and mound zone were investigated in detail and the results published recently (Polgári et al., 2012ab, 2013, 2016ab). A complex model proposed for the formation of the Úrkút Mn-ore deposit included the different carbonate and oxide ore types, the black shale, and the possible source of metals based on the contemporaneous tectonic framework (Polgári et al., 2012a). Though the Fe-Mn oxide indications of the feeder and mound zone in the footwall of the Mn-carbonate deposit were mentioned (assuming a distal mineralized feeder and mound zone), and preliminary results published, a detailed study of this so-called contact zone (feeder and mound zone) between the footwall limemarlstone and the Mn-carbonate deposit had not been undertaken. This zone can provide important information about the initial stage of ore formation (Polgári et al., 2012a).

Here**,** we review the main characteristics of the feeder and mound zone between the footwall limemarlstone and the black shale-hosted Úrkút Mn deposit, and provide detailed

97 microtextural, mineralogical and geochemical data from which we interpret the fundamental
98 processes of formation, paleoenvironmental conditions, and relationship to the ore beds.
99
100 **2. Geological setting**
101 The Transdanubian Central Range of Hungary is an important region for a series of
102 structurally controlled Jurassic black shales and their associated Mn mineralizations of variable
103 sizes. The Úrkút and Eplény deposits are located in the central part of the Bakony Mountains,
104 which belong tectonically to the North Pannonian unit of the Alps-Carpathians-Pannonian
105 regions (ALCAPA, Fig. 1a; Polgári et al., 2012a). Detailed geological and ore-deposit
106 background are given by Polgári et al. (2012a), and a profile is shown in Fig. 1b.
107 Underlying the carbonate ore bed there is a zone of some meters to tens of meters thick
108 observable in the mine between the footwall limemarlstone and the ore bed, which includes
109 dissolution forms, variable Fe-Mn oxide indications in the form of vein fillings resembling
110 mineralized feeder zones, enrichments along layers, stockwork-like structures, infiltrations and
111 stromatolitic mound-like bodies showing inner concentric structures. The signs of alteration of
112 the limemarlstone (greenish-gray zones reflecting leaching processes) are also characteristic
113 (Fig. 1c-e, SI. 1). In contrast, the Mn-carbonate ore bed overlying the footwall is unaltered. The
114 Fe-Mn oxide of the feeder and mound zone look massive, bluish black or brown, hard, often
115 containing coarser crystalline parts. They generally occur as vertical vein fillings, which mainly
116 end at the zone of the limestone and limemarlstone hosting mounds of a few to 50 cm high. At
117 the contact of the Fe-Mn-oxide indications of the feeder zone, the host rock shows a few cm
118 thick alteration zone which is limonitic, clay mineral-rich, and/or cherty. The thickness of the
119 limonitic zone is a few mm.
120 The Fe-Mn oxide indication of the feeder zone in the footwall begins some tens of cm
121 below the footwall limemarlstone and the ore contact and ends at the contact (Fig. 1cd); it also
122 occurs in the unaltered Mn-carbonate ore bed. The boundary between the Fe-Mn oxide phases
123 and the Mn carbonate is not transitional (Fig. 1e). The typical contact zone from the footwall
124 towards the ore bed consists of the following parts: (i) typical thick, reddish-gray spotted
125 Pliensbachian limestone with chert layers; (ii) reddish-gray limemarlstone with gray-greenish-
126 gray layers, fine texture, often with calcitized *Belemnite* rostrums, green clay mineral vein
127 fillings are common, also with yellowish-brown thin fractures; the thickness is 1-1.2 m; (iii)

greenish-brown limemarlstone, similar to the above described, but with a more homogenous texture, with a thickness of 0.2-0.5 m; (iv) gray, pyritiferous *Radiolarian* claymarlstone, the start of the ore complex; (v) the unaltered Mn-carbonate ore (main ore bed of brown-gray type).

It has been proposed that hydrothermal fluids venting into the depositional basin was involved in the mineralization (Polgári et al., 2012a). The Fe- and Mn-oxides were probably deposited from deep-sourced fluids circulating through basement rocks. Circulation along zones of structural weakness was likely driven by high geothermal gradients (Polgári et al., 2004; 2007, 2012a), but direct evidence for this has not been found.

3. Samples and methods

Five sets of samples were collected at 16 places in the feeder and mound zone between the basement limemarlstone and the black shale-hosted Mn-carbonate ore deposit (total 54 samples; Table 1, Fig. 2b). Sample sets 1-4 were collected at the deep level of the Úrkút manganese mine, set 5 was collected at the Eplény mine from a similar geologic position and used for comparison (Fig. 1a).

Sampling of the footwall contact zone and the manganese proto-ore of the Úrkút manganese-ore deposit was concentrated at the boundaries of different lithofacies (Fig. 2, SI. 1 and 2). Accordingly, two short sections with 30 samples (sets 1 and 2) were studied from the base of the footwall limemarlstone to the overlying black shale, just below the Mn-carbonate ore bed. Eleven samples are from the oxide feeder and mound zone, 18 from the base (footwall) limemarlstone, and one from the overlying black shale. Another 24 samples supplement the short sections, from 6 different parts: 15 from the Mn-oxide indication and nine from the feeder and mound zone between the ore and the limemarlstone (SI. 2).

Petrographic structural-textural studies were made on 10 polished surfaces, and 15 thin sections in transmitted light (NIKON SMZ800 microscope and NIKON ECLIPSE 600 rock microscope, Institute for Geology and Geochemistry, Research Centre for Astronomy and Earth Sciences, Hungarian Academy of Sciences - IGGR RCAES HAS, Budapest, Hungary).

Cathodluminescence (CL) petrography was carried out on 4 thin sections using a Reliotron cold cathode microscope, operating at 5-8 kV and 0.9 mA (IGGR RCAES HAS, Budapest, Hungary).

Mineralogical analyses were performed on 14 bulk samples using a Philips PW 1730 X-ray powder diffractometer (XRD), with carbon monochromator and Cu Kα radiation, at 45 kV

and 35 mA. Mineral composition was determined on randomly oriented powdered samples by semi-quantitative phase analysis using a modified method of Bárdossy et al. (1980) and previously defined intensity factors. For finer-scale *in situ* results, we used micro-X-ray diffractometry on four thin sections (14 spectra) using a D/MAX RAPIDII with Cu K_{α} radiation at 50 kV, IP detector and 300μ collimator using 3 minutes acquisition time (IGGR RCAES HAS, Budapest, Hungary).

Chemical measurements were made on two sets of samples. The first set of samples (n=9) was analyzed for 40 major, minor, and trace elements using 4-acid digestion (hydrochloric, hydrofluoric, nitric, perchloric acids) in conjunction with inductively coupled plasma-atomic emission spectrometry (ICP-AES; SGS Laboratories, Ottawa, Canada). The resulting solutions were dried and the residue dissolved in 1 ml of aqua regia and then diluted to 10.0 g with 1% (volume/volume) nitric acid. Another split of each sample was fused with lithium metaborate then analyzed by ICP-AES after acid dissolution of the fusion disc. This technique provides analysis of all major elements, including Si, and a few minor and trace elements. The accuracy of Si determinations was 2-4% based on the total-oxide sum. Sr and Ba contents were determined by both the 4-acid digestion and fused disc techniques, which produced comparable results. Ti and Cr were also analyzed by both techniques, but only data from the fused-disc technique are used because of the better digestion of refractory minerals that might contain those elements. Se, Te, As, Sb, and Tl concentrations were determined by hydride generation followed by atomic absorption spectrometry (AAS). Mercury was determined by cold vapor AAS.

Trace-element contents of the second set of samples (n=10) were determined using Agilent MP-AES-4200 instrument for selective elements (Al, As, Ca, Co, Cr, Fe, K, Mg, Mn, Na, Ni, Ti, V, Zn). One gram was weighed (accuracy 0.1 mg) to a plastic beaker and 8 ml of 65% nitric acid (JT-Baker; CAS: 7697-37-2) was added. The beaker with the mixture was then placed in a temperature-controlled water bath to assist the dissolution. After the development of nitrous gases, the sample was cooled to room temperature and 8 ml of nitric acid was added again, followed by 2 ml of hydrogen peroxide (30%, Fluka, CAS: 7722-84-1). The dissolution process was repeated and the second step was performed once more. The liquid phase was then evaporated to dryness and the residue was redissolved in 0.1 mol/l nitric acid. The insoluble solid residue portions were separated by centrifugation and the clear solution was filled to 50 ml total volume. Calibration reference solutions were prepared using multi-element stock standard

191 solutions (SCP Cal Plasma Science, CAS: Chemical name 7697-37-2). Three replicates were
192 done for each metal, the detection time was 5 seconds, the rinse time of the system was 35
193 seconds with 15 seconds stabilization time. The concentration of the elements (ppm) were
194 calculated using the corresponding dilution factor. The limit of detection (LOD) and difference
195 between the replicates (% RSD) were also determined.
196 Element composition and microtextural features of four thin sections were determined at
197 1–2 μm spatial resolution on carbon-coated samples using a JEOL Superprobe 733 electron
198 microprobe with an INCA Energy 200 Oxford Instrument Energy Dispersive Spectrometer, run
199 at 20 keV acceleration voltage, 6 nA beam current and count time of 60 s for the spot
200 measurement and 5 min for line-scan analysis. Olivine, albite, plagioclase and wollastonite
201 standards were used; we estimated that the detection limit for the main elements was below 0.5%
202 based on earlier measurements with various samples (IGGR RCAES HAS, Budapest, Hungary).
203 Element distributions and microtextural features were made along line profiles on two
204 selected polished thin sections coated by gold (sample No. 4/C, 4/D; in length; using a Jeol 25
205 electron-microprobe with Quantax EDX system, at 25 kV accelerating voltage and 150-360 pA
206 beam current, with scans at 10 μm intervals, for 5 minutes/4 mm length, and intensity profiles of
207 the elements were used for identification. For Ca, a narrow channel was used and for Fe, Kβ was
208 used for identification to avoid overlap of Mn Kβ and Feα; to get the real Fe intensity, a five-
209 times factor was counted on the FeKα/FeKβ ratio) (Wigner Research Centre for Physics, HAS,
210 Budapest, Hungary).
211 $\delta^{13}C$ and $\delta^{18}O$ were measured on carbonates (calcite, n=21) using a Finnigan Delta V
212 continuous-flow mass spectrometer equipped with a Thermo Flash element analyser (IGG
213 RCAES HAS, Budapest, Hungary). Three sets of samples were measured for comparison. The
214 first set contained 14 and the second set 7 samples; the third set is the same set as the first set, but
215 analyses were done before the samples were dried at 180 °C. Results are given in per mil (‰)
216 versus V-PDB (^{13}C) and SMOW (^{18}O) standards. Standard deviation of the data is below 0.1‰
217 based on the reproducibility of sample triplets and laboratory standard data.
218 Fourier transform infrared spectrometer (FTIR) was used for *in situ* micro-mineralogy
219 and organic material identification on two thin sections (21 spectra, IGGR RCAES HAS,
220 Budapest, Hungary), using a Bruker FTIR VERTEX 70 equipped with a Bruker HYPERION
221 2000 microscope with a 20x ATR objective and MCT-A detector. During attenuated total

reflectance Fourier transform infrared spectroscopy (ATR) analysis, the samples were contacted with a Ge crystal (0.5 micron) tip with 1 N pressure. The measurement was conducted for 32 seconds in the 600–4000 cm^{-1} range with 4 cm^{-1} resolution. Opus 5.5 software was used to evaluate the data. The equipment cannot be used for Mn-oxide determination because those peaks fall in the <600 cm^{-1} range. Contamination by epoxy glue, glass, wood stick, and dichloromethane was taken into consideration.

High resolution in situ micro-Raman spectroscopy was used for micro-mineralogy and organic matter identification on 5 thin sections, resulting in 763 spectra. A Thermo Scientific DXR Raman Microscope was used, with a 532 nm (green) diode pumped solid-state (DPSS) Nd-YAG laser using 1.5 mW laser power, 50x objective lens in confocal mode (confocal aperture 25 µm slit). Acquisition time was 1 min and spectral resolution was ~2 cm^{-1} at each measurement (Szeged University, Hungary); the distance between each point was 100 µm and the measurement time was 10 min. A composite image of thin sections of Raman microscopy measurements and series of Raman spectra acquired along the vertical sections are indicated on thin section photos (arrow points to measurement direction). Diagrams were organized on peak height versus analytical spot number of each of the phases along the Raman scanned section. Intensities were normalized to the highest peak for each spectra. The following Raman bands were used for normalization: quartz: ~463 cm^{-1}; dolomite: ~1096 cm^{-1}; aragonite: ~1085 cm^{-1}; goethite: ~390 cm^{-1}; hollandite: ~580 cm^{-1}; groutite/manganite: ~554 cm^{-1}; cryptomelane: ~184 cm^{-1}; carbonaceous matter: ~1605 cm^{-1}. Identification of minerals was made with the RRUFF Database (Database of Raman – spectroscopy, X-ray diffraction, and chemistry of minerals: http://rruff.info/). Contamination by epoxy glue was taken into consideration. The sensitivity of FTIR is better than that of Raman spectroscopy for organic matter, and also measurements of the extracted samples give more accurate results as the peaks of mineral compounds do not impact the interpretation.

For the bulk characterization of the organic matter (OM), ~25g of the powdered samples were extracted with ASE350 equipment with n hexane at 70° C for 10 minutes. After extraction, 2 samples were sufficient for “fingerprint” GC-MS analyses, and all six samples were measured by FTIR-ATR.

4. Results

253 **4.1. Rock microscopy and SEM-EDS**

254 *Footwall limemarlstone*

255 Polished slabs and thin section observations show stromatolite-like macro and microtextures
256 (Fig. 3a-d). Most of the footwall limemarlstone consists of calcite micrite, which is partly
257 silicified based on CL observations. Variable amounts of biodebris (*Foraminifera*, *Echinoidea*,
258 fish remnants, etc.) and mineral grains (quartz, idiomorphic dolomite, feldspar) are embedded in
259 the micrite together with clay-mineral-rich lenses. Clay mineral patches often show signs of
260 bioerosion in the form of boring of bacteria, fungi or benthic fauna (SI. 3, 2/4-3). Ellipsoid forms
261 with radial complex inner structure and filamentous (vermiform) structures with pearl necklace-
262 like inner texture are also common (Fig. 3e-h, SI. 3).

263 *Ore indication in the limemarlstone*

264 The initial stage of mineralization caused dissolution of calcite micrite matrix, which was
265 followed by disseminated precipitation of fine-grained Fe-Mn oxide in unconsolidated and/or
266 slightly consolidated sediment. The Fe-Mn infiltration proceeded along the margins of the calcite
267 biodebris fragments and mineral grains and affected only the matrix and the pores of the
268 biodebris fragments (Fig. 4). The marginal parts of early diagenetic dolomite showed Mn
269 substitution for Ca and Mg (Fig. 5d.). The calcite tests of the biodebris were replaced by Fe-Mn
270 oxides only in the most intensely mineralized areas (Fig. 5gh). The Fe-rich zones are generally
271 finely laminated resembling stromatolites and consist of alternating laminae of Fe- and Mn-rich
272 phases (Fig. 5a). The Fe-rich stromatolite-like laminae occur presumably at the paleo-
273 sediment/seawater interface. Similar finely laminated textures occurred when the sediment was
274 built up by manganite and Ba- and K-rich manganese oxides. Rock microscopy and SEM-EDS
275 results indicate filamentous mineralized textures with microbial morphologies (Fig. 4cef, 5j).

276 Most of the Mn-rich mineral phases have relatively high contents of Ba (3.21 wt.% to
277 15.3 wt. %) and K (1.01 wt. % to 15.0 wt. %) and lower Sr content, 1.14 wt. % in one sample. In
278 the Fe-rich zones, Si shows a wide range, from 1.51 to 48.3 wt. %) and is likely associated with
279 the clay mineral-rich parts. The Fe-rich zones are enriched in C_{org} comparing to limemarlstone
280 (for details see section 4.4. and SI 4).

281

282 **4.2. Bulk mineralogy (XRD), in situ microXRD**

283 *Footwall limemarlstone*

The main components are calcite and clay minerals (smectite and celadonite). The amount of clay minerals increases toward the ore deposit. Quartz, dolomite, and K-feldspar are also common, but these components do not show trends (SI. 5). K-feldspar occurs mainly in the clay mineral-rich lenses. Kaolinite and chlorite occur as trace components. Apatite is a minor component that originates most probably from fish debris.

Fe-Mn oxide indications consist of Fe-oxyhydroxides such as goethite, and less commonly Mn oxides romanèchite, manganite, groutite, pyrolusite, birnessite, hausmannite, cryptomelane, hollandite, and XRD amorphous Mn oxide, which occur generally alternating with Fe-oxide laminae. These Fe-Mn oxide indications occur as vein fillings and also as mineralized mounds or infiltrations in the limemarlstone. Calcite was commonly detected to occur with the Mn-rich phases, and clay minerals (10 Å phyllosilicates) occur with the Fe-oxyhydroxides. Rarely kutnohorite and rhodochrosite were detected.

4.3. Chemistry

The chemical composition determines the main and trace element content of the Fe-Mn-oxide indications, which is why most of the samples have relatively low Ca contents (Table 2). The Mn and Fe contents are highly variable (Fig. 6). The average content of Mn is 35.9 wt. % (max: 48.6 wt. %), Fe 10.3 wt. % (max: 40.1 wt. %), Si 4.95 wt. % (max: 6.69 wt. %), Al 1.34 wt. % (max: 2.8 wt. %), Ca 1.25 wt. % and K 2.21 wt. % (max: 3.91 wt. %). The P content of the Fe-Mn oxides is relatively high, average 0.3 wt. % (max: 0.86 wt. %). Among trace elements, Ba (0.31 wt. % average, max: 1 wt. %), Sr (0.98 wt. %, max: 0.98 wt. %) and Co (0.077 wt. %, max: 0.14 wt. %) are worthy of mention (Fig. 6).

4.4. Stable isotopes

$\delta^{13}C_{PDB}$ values are around ~0‰, and $\delta^{18}O_{SMOW}$ values are ~29‰ for the footwall limemarlstone (Table 3, Fig. 7). The mineralized zones have negative $\delta^{13}C_{PDB}$ values, between -21.35‰ and -5.13‰, and $\delta^{18}O_{SMOW}$ values between 9.93‰ and 21.41‰. The lower values are associated with the most intense mineralization, and progressively increase to the unmineralized footwall limemarlstone.

Temperature calculations

Based on $\delta^{18}O_{SMOW}$ values, temperature calculations were made following the method of Veizer & Hoefs (1976) and Coplen (2007). We calculated α (fractionation coefficient) as $\alpha=\delta^{18}O_{calcite-}$

316 $_{SMOW}$+1000/ $\delta^{18}O_{water\text{-}SMOW}$+1000, where the $\delta^{18}O_{water\text{-}SMOW}$ is zero. Assuming an oxygen isotope
317 value of −5‰ proposed for Jurassic seawater (Veizer & Hoefs, 1976), unrealistic negative
318 temperatures are produced. Assuming an oxygen isotope value of 0‰ for the extant seawater
319 gives more realistic temperature estimates (Table 3). In this calculation, we assume that isotopic
320 equilibrium was reached. Based on these equations and assumptions, a temperature range from
321 18.4° C to 30.3° C is calculated for the formation of footwall limemarlstone (subtropical
322 environment). For the Fe-Mn oxide indication, the calculation resulted in higher temperatures,
323 from 41.1° C to 160.5° C. Typically, the higher estimated temperatures are within the Fe-Mn-
324 oxide mineralization of the feeder zone and mounds, and the values decrease rapidly toward the
325 contact with the limemarlstone.
326
327 **4.5. FTIR in situ measurements**
328 The peaks for Mn oxide fall out of the detection interval of the equipment. The samples
329 generally contain various Fe-oxide minerals like goethite, ferrihydrite, maghemite and
330 akaganeite (Table 4; SI 6). The mixed Fe-oxide minerals can cause overlapping bands. The
331 rhodochrosite is also a common component on a micrometer scale. Apatite appears in several
332 spectra. The spectra contain traces of montmorillonite, chlorite, and quartz.
333 Most of the spectra include IR bands of organic material (symmetric and asymmetric
334 stretching of CH_2 and CO vibrations at 2360 and 2340 cm^{-1}, and C=C asymmetric stretching near
335 1600 cm^{-1}. Several spectra contain amide bands near 1550 cm^{-1} and at 1640 cm^{-1}. Rarely OH
336 bands near 3510 cm^{-1} were present.
337 These results were confirmed using ATR-FTIR on extracted organic material (vibration
338 bands C-C; C=C; C-H bonds), which also provided new information. *ATR-FTIR* measurements
339 on the six organic matter extracts showed the following major bonds C=C, C=C=O, O=C=C,
340 C=O=C, C-C, C-H, $C=H_2$, $C\equiv H_3$, and OH. Based on the types of bonds, the following organic
341 compounds were determined: esters (aliphatic and acetyl), organic acids (carboxylic acid),
342 aromatic groups and phenols (lignin). The type of polycyclic aromatic hydrocarbons (PAHs),
343 fluerenes, and heterocyclic compounds were not identified in detail. The PAHs and fluorenes
344 would reflect degradation products of charred woody debris, and the heterocyclic aromatic
345 compounds would reflect microbial activity, together with the other measured organic
346 compounds.

347

348 **4.6. Organic geochemistry of bulk samples**

349

350 Extraction from six samples resulted in low yields of total organic matter (0.0045-
351 0.0027%). Only two samples were suitable for GC-MS measurements (2/1 and 4/B) with 1.2 mg
352 total extraction. GC-MS for sample 2/1 showed the signature for terrestrial plants based on
353 significant $C_{27\text{-}31}$ *n*-alkane peaks with strong odd dominance. The pristane to phytane ratio
354 (Pr/Ph) is 1.64, suggesting a suboxic-oxic environment. Pr/n-C17 and Ph/n-C18 values (2.50 and
355 1.90, respectively) are high. Organic matter in sample 4/B is presumably of marine algal origin,
356 without terrestrial plant contribution. The Pr/Ph ratio is 0.72, reflecting reducing conditions.
357 Pr/n-C17 and Ph/n-C18 ratios are 0.47 and 0.66, respectively. Potential bioindicators were below
358 the detection limits.

359

360 **4.7. Raman spectroscopy in situ measurements**

361 Raman spectroscopy measurements were carried out on 5 samples producing 763 spectra
362 (Table 1; Fig. 8; SI. 7). Some of the samples showed laminated textures resembling
363 stromatolites. The main mineral phases in the samples are Mn and Fe oxides (hollandite,
364 cryptomelane, manganite/groutite, goethite) and variable types and amounts of organic matter.
365 The distribution of these components is not random, they show regularity in the alternation of
366 thin laminae (Fig. 9). Most of the samples consist of hollandite, which is intercalated with
367 goethite, groutite/manganite, and cryptomelane, and discrete laminae of organic compounds. In
368 sample No. 3/A, hollandite and cryptomelane show opposite distributions, while goethite and
369 groutite/manganite show fine alternating lamination with organic matter. A similar phase
370 distribution occurs in sample No. 5/1 (SI. 7), but in this sample, goethite and hollandite laminae
371 alternate. Minor organic matter was probably trapped in Fe-Mn oxide minerals as they formed.
372 Dolomite occurs randomly. The oscillation of the quantity of mineral phases and organic
373 compounds fits well with the macroscopically and microscopically observed stromatolite-like
374 textures (microbialite).

375 Raman spectral study of organic matter was made for two samples (3/1, 4/D), which
376 resulted in more variable organic compound types than detected by FTIR. Besides the organic

compounds listed in 4.6, the presence of polycyclic aromatic hydrocarbons (PAHs), fluorenes, and heterocyclic aromatic compounds were detected.

5. Discussion

Study of the feeder zone and mounds is scarce because they have no economic value. On the other hand, they provide key information on the metal source, enrichment processes, and preservation of the ore body. Besides characterization of the complex feeder and mound zone between the ore and the footwall limemarlstone, the direction and source of fluid migration is addressed (Table 5; Fig. 9; SI. 8).

Footwall limemarlstone: Mineralogy, microtexture and paleoenvironmental consideraions

Several papers have reported the heterogeneity of the footwall of the Úrkút manganese ore deposit, mainly the presence of limemarlstone and limestone units (e.g., Bíró, 2014). Based on our results, the major mineralogy of the footwall is microcrystalline calcite and idiomorphic dolomite, with increasing amounts of quartz, 10 Å and 10.5 Å clay minerals (smectite, nontronite, celadonite) from the footwall zone to the ore. Quartz and rare K-feldspar as ash fall particles were also detected. The occurrence of ash falls, the only apparent terrestrial input, is also supported by the presence of terrestrial polyaromatic hydrocarbons (PAHs), however, potential terrestrial components require more detailed study. The sedimentary basin was a starved basin because the input of terrestrial debris was blocked by an intervening sea (Haas, 1994, 2012; Polgári et al., 2012a). The sections are enriched in calcareous bioclasts (*Echinozoa*, *Foraminifera*, etc.) and ellipsoidal forms with radial inner structures interpreted as cyanobacterial perimorphs (observed for the first time in the Úrkút section). Pekker (2005) reported similar microbial biosignatures from the hanging wall of the Mn deposit (Eplény Limestone). Another possibility for these forms can be diagenetically altered sponge spicules, which are also common constitutions in the footwall. The clay minerals appear in spots and patches. On the individual clay mineral patches borings resembling bioerosional traces are observed for the first time. Around the grains, complex arrangements of filaments occur, with 5-10 μm length and globular inner structure as mentioned before (mineralized microbially produced structures-MMPS, Polgári et al., 2012b). The footwall limemarlstone formed in a

409 subtropical environment as a normal marine carbonate platform, where the temperature was in
410 the range of 18.6° C to 26.1° C. These results fit well with the previous conclusions published by
411 Szabó & Grasselly (1980) and Szabó et al. (1981).
412 We infer that there was significant microbiological activity on the surface of the sediment
413 that promoted the formation of clay minerals. Most of the clay minerals are authigenic and may
414 have formed in contact with the surface of cellular organic matter and extracellular polymeric
415 substances (EPS) (Yeshaya & Moshe, 1988; Konhauser & Urrutia, 1999; Zavarzin, 2003). An
416 earlier hypothesis on the formation of the authigenic clay minerals suggested that ore-forming
417 fluids promoted precipitation, and that the Fe-rich character of the clay minerals was thought to
418 confirm this scenario (Polgári, 1993, Polgári et al., 2000). Our work supports the microbially
419 mediated formation of clay minerals (trapping of organic matter and the borings on clay mineral
420 patches) as a more plausible explanation. While the microbiota were living, the binding capacity
421 of EPS for Ca^{2+} was strong, which retained the micritic carbonate. After the death of the
422 microbiota, the degradation of EPS started during early diagenesis and calcite nucleation took
423 place on the surface of the decaying EPS, forming calcite microsparite, as proposed by Dupraz &
424 Veisscher (2005). During diagenesis, calcite was transformed into dolomite (idiomorphic
425 dolomite) and aragonite (Pace et al., 2015). Our observations support this scenario as the
426 idiomorphic dolomite grains are common in the footwall and in the entire Mn deposit. Similar
427 early diagenetic dolomite was reported by others (João et al., 2012; Ayupova et al., 2016). For
428 the dolomite at Úrkút, a different origin was proposed, as wind-blown particles from sabkhas
429 (Pekker, 2005, Cora, 2009), which is not supported by our data.
430 The sedimentary environment was oxic to suboxic and most of the organic matter was
431 oxidized, which is reflected by the extremely low total organic content. This is supported by the
432 $\delta^{13}C_{PDB}$ values, which are around 0‰ in the footwall limemarlstone. This does not contradict the
433 microbially mediated formation of the limemarlstone because some calcite nucleation processes
434 involve mineralization of inorganic carbon (Dupraz & Veisscher, 2005).
435
436 *Mineralized feeder and mound zone in limemarlstone: Mineralogy, microtexture and*
437 *paleoenvironmental considerations*
438 Two types of feeder and mound zone indications were reported by Polgári et al. (2012a):
439 Fe-Mn infiltration similar to vein fillings (stockwork-like feeder zone), and concentric,

stromatolite-like mineralized mounds (chimney-like forms) commonly with brown Fe-oxide-rich outer coating.

Our results indicate that the mineralogical composition of the feeder and mound zone is heterogeneous, and fits well with that reported by Polgári et al. (2012a). The recent mineralogical data partly confirmed previous results and identified new mineral phases like pyrolusite, romanechite, birnessite, hausmannite, hollandite, and in the case of Fe-oxyhydroxides, ferrihydrite, maghemite, akaganeite and also traces of kutnohorite and rhodochrosite. The carbonate composition is variable, as also reported by Hahn (2010).

The initial stage of mineralization of the feeder and mound zone caused dissolution of the calcite micrite matrix transsected by the fluids, which was followed by disseminated precipitation of fine-grained Fe-Mn oxide in unconsolidated and/or slightly consolidated sediment. The Fe-Mn infiltration process went along the calcite biodebris tests (filling first only the pores by Fe-Mn-oxide minerals), sidestep also the mineral grains, and cemented and partly replaced the originally calcite-rich matrix. Traces of akaganeite detected by FTIR indicate a slight sulfidic influence via fluid migration, as was also proposed by Polgári et al. (2012a). Akaganeite forms by alteration of pyrrhotite, representing an intermediate phase via transformation to hematite (Frandsen et al., 2014).

Fe-oxide/oxyhydroxide and Fe-bearing clay minerals in discrete laminae (zones) are intercalated with the Mn-oxide laminae together with variable organic compounds, resulting in finely laminated stromatolite-like textures. Pyrolusite occurs as fine needle-like crystals near pore-filling cryptomelane and hollandite. The transition between the footwall limemarlstone and the feeder and mound zone is continuous on a micrometer scale.

Though it was proposed earlier that these textures reflect stromatolites (Polgári et al., 2012a), the evidence was not conclusive. Based on our results, the microbial mediation is supported by the finely laminated manganite and goethite alternation forming microbialite, and the various embedded organic material (trapped) in the Fe-Mn oxide mineral phases. The aromatic cyclic CH and polycyclic aromatic CH are enriched with Mn (Jehlička et al., 2009), and the filamentous biosignatures also convinsingly support this scenario. Determination of the character of microbial mediation (biologically induced or controlled) is a great challenge, though the formation of microbially mediated Fe-Mn oxides is well studied (Mandernack et al., 1995; Konhauser, 2012). A large part of the ore-forming metal content could have been trapped in the

471 footwall limemarlstone in the form of disseminated fine-grained metal oxides, and by
472 metasomatic formation of carbonate and clay minerals.
473
474 *Source of metals, enrichment effects, and temperature calculations*
475 There are several proposals as to the source of the Mn in the Úrkút basin. An important
476 consideration in understanding the source of the ore-forming fluids is the lack of direct
477 connection with volcanic rocks; the Bakony Mts are extensional allochtons (Kázmér & Kovács,
478 1985; Csontos & Vörös, 2004). Szabó-Drubina (1959) proposed first that the proto-ore might
479 have been the result of local hydrothermal activity. Szabó et al. (1981) and Varentsov et al.
480 (1988) suggested the center of the activity was the Csárdahegy – Nyíres fault zone. Kaeding &
481 Brokamp (1983) also proposed an internal source based on geochemical evidence and the
482 occurrence of celadonite, commonly a product of altered volcanogenic material, or syngenetic
483 product. Polgári (2012a) proposed a diffuse-discharge system, with low temperature (~40 °C)
484 based on the thermal stability of the celadonite, which is the main component of the deposit, and
485 on the $\delta^{18}O_{SMOW}$ values, which were determined from the Mn-carbonate ore and the host black
486 shale (Polgári et al., 1991).
487 Results presented here support these ideas, but propose a higher temperature (50-160° C)
488 for the initial hydrothermal fluids based on $\delta^{18}O_{SMOW}$ values, which differ basically from the
489 datasets measured earlier from the ore beds and black shale (Fig. 7). Assuming equalibrium
490 conditions, the calculated temperature in the central parts of the Fe-Mn-oxide feeder and mound
491 zone is high and decreases toward the host limemarlstone (Jaffrés et al., 2007). This fits well
492 with the recently published results on the Uralian microbially mediated hydrothermal Fe-Mn-
493 oxide deposits that formed at elevated temperatures, based on oxygen isotopes (Ayupova et al.,
494 2016). From the $\delta^{18}O_{SMOW}$ data, it is clear that the carbonate content of the deposit can influence
495 the $\delta^{18}O_{SMOW}$ results (Fórizs et al., 2015). Based on their experimental studies, less than 5%
496 carbonate content can shift the $\delta^{18}O_{SMOW}$ toward higher values of around 0.5‰. The laboratory
497 experiments are continuing to determine whether even smaller amounts of carbonate (less than
498 1%) influence the $\delta^{18}O_{SMOW}$ values. The initial stage of feeder and mound zone formation
499 involved substitution of calcite micrite by Fe and Mn oxides, which resulted in a marked
500 decrease of carbonate content toward the central parts of Fe-Mn oxide feeder and mound zone. A
501 further influence could be the water content of the sediment, which was addressed by heating and

drying of repetitive samples to 180° C. This also caused changes of the $\delta^{18}O_{SMOW}$ values measured from the same samples after heating, but clear trends were not detected.

Taking into account these influences on the $\delta^{18}O_{SMOW}$ data and the control data (from dried samples), earlier $\delta^{18}O_{SMOW}$ data differ markedly from those reported by Polgári et al. (1991). The interpretation of our $\delta^{18}O_{SMOW}$ values allow for additional hypotheses. For example our $\delta^{18}O_{SMOW}$ values are consistent with high-temperature fresh-water input, however that possibility can be excluded based on geological and paleontological observations (Vető et al. 1997; Polgári et al., 2000; etc.). Though the existence of small nearby islands in the vicinity of the Úrkút basin (wood fragments, Polgári et al., 2005) cannot be excluded, their presence could not be a dominant factor based on microfossil evidence (Galácz & Vörös, 1972; Vörös & Galácz, 1998). On the other hand, the measured samples were collected from a small area and local fresh-water springs cannot be excluded, but that possibility contradicts a deep-water depositional environment (600-800 m) proposed by Galácz & Vörös (1972). The lowest $\delta^{18}O_{SMOW}$ values occur together with the most negative $\delta^{13}C_{PDB}$ values, which indicates contributions from the decomposition of organic matter, raising the possibility of variable microbial activity at elevated temperature and a proto-ore forming nutrient-rich hydrothermal fluid, which increased the light C isotopic component in the formation of carbonate. Based on these results, an ascending ore-forming fluid at elevated temperature along a rift zone is proposed as the driver and source of Mn-Fe-Si-rich fluids, which facilitated microbially mediated Fe-oxide precipitation under neutral suboxic conditions; these conditions likely characterized the paleo-seafloor environment.

The available pathways of Mn(II) oxidation in water are introduction of oxic fluids, oxide surface catalysis, and biologic (enzymatic) oxidation (Morgan, 2005). For the Fe-Mn-oxide indications of the feeder and mound zone, our results support a Fe-oxide surface catalysis mechanism for oxidation of the Mn(II). This is characteristic for mineralized chimney-like mounds, which are presumably stromatolites. The enzymatic Mn(II) oxidation is proposed to be the major process via the formation of oxide proto ore of the diagenetic Mn-carbonate ore bed. This is consistent with earlier reported mineralogical, textural and geochemical evidence and the failed rift setting of Polgári et al. (2012a).

Genetic model

532 The results presented here expand the complex model of Mn deposit formation. The Fe-
533 Mn-oxide indications are most probably the result of syngenetic microbially mediated
534 mineralization of a feeder and mound system under the carbonate ore bed. These results require
535 us to propose a much larger area of discharge than was previously thought (Fig. 9ab). The
536 greatest discharge zone occurred at the fracture zone of Csárdahegy that produced the cherty Fe-
537 rich Mn-oxide ore type of proximal mineralization. Deposit bedding indicates the syngenetic
538 formation of different ore types: cherty Fe-rich Mn oxide (proximal feeder zone); Fe-Mn oxide
539 indications of distal feeder and mound zone under the Mn-carbonate deposit; and proto-ore of the
540 diagenetic carbonate that produced the main mass of the ore deposit, in part at different locations
541 of the mineralizing system. Further, the genetic mechanism may also have been different. For the
542 feeder zones, microbially mediated suboxic Fe oxidation took place and Mn oxidation occurred
543 through surface Fe-oxide catalysis. This system is characterized by lower C_{org}. The distal facies
544 was favorable for enzymatic Mn oxidation accompanied by a much larger role for C_{org} and its
545 accumulation. These factors promoted different diagenetic processes, and the formation of
546 diagenetic rhodochrosite is scarce in the feeder zones, while it is the main component in the
547 distal area (Fig. 9a).
548 Similar Fe-Mn oxide proto-ores transformed during diagenesis to carbonate ores and
549 indications were reported for the Molango deposit (Mexico; Okita & Shanks, 1988), Moanda
550 (Gabon; Hein et al., 1989), Uralian occurrences (Maslennikov et al., 2012; Ayupova et al., 2016),
551 and Wafangzi, Minle-Datangpo, Gaoyan, and Taojiang (China; Fan et al., 1996). A similar
552 genetic model is applicable to a failed rift origin for the Alpine-Mediterranean Jurassic Fe-Mn
553 enrichments (e.g., Jach & Dudek, 2005).
554
555 **6. Conclusions**
556 The mineralized feeder and mound zone between the footwall limemarlstone and the black shale-
557 hosted Mn-carbonate deposit at Úrkút was investigated by high-resolution mineralogical,
558 microtextural, geochemical, and bulk and *in situ* organic geochemical and mineralogical
559 methods. These data provide key information on feeder zone formation, the initial stage of ore
560 formation.

561 The main components of footwall limemarlstone are calcite and clay minerals (smectite
562 and celadonite), which increase toward the ore-deposit. Quartz, dolomite, and K-feldspar are also
563 common, but do not show trends.
564 Feeder zone and mound indications consist of Mn oxides (romanèchite, manganite,
565 groutite, pyrolusite, birnessite, hausmannite, cryptomelane, hollandite, X-ray amorphous Mn
566 oxide), and Fe-oxyhydroxides (goethite, ferrihydrite, maghemite, akaganeite), which occur with
567 the Mn oxides. The Fe-rich zones are generally finely laminated resembling stromatolites and
568 consist of alternating laminae of Fe- and Mn-rich oxide phases. The Fe-rich parts formed at the
569 sediment-seawater interface.
570 The initial stage of mineralization of the feeder and mound zone caused dissolution of the
571 calcite micrite sediment, which was followed by disseminated precipitation of fine-grained Fe-
572 Mn oxides in the unconsolidated or weekly consolidated sediment. The Fe-Mn infiltration
573 affected only the matrix via dissolution and replacement and did not alter the calcite biodebris or
574 mineral grains. Calcite tests were mineralized only at the most intensely mineralized places.
575 Early diagenetic dolomite grains were replaced by Mn oxides along their margins.
576 Based on these textures and mineralogy, the nearly zero $\delta^{13}C_{PDB}$ (-2.25 ‰ – 0.64 ‰), and
577 the $\delta^{18}O_{SMOW}$ (28.58 ‰ – 29.87 ‰) data, we propose that the Úrkút ore deposit stated as a
578 normal marine carbonate platform formed in a subtropical environment where the temperature
579 was between about 18.6° C and 26.1° C. In the mineralized feeder and mound zones, a newly
580 calculated higher (50-160° C) temperature for the initial hydrothermal fluids (based on the
581 $\delta^{18}O_{SMOW}$) is proposed, which differs from inferences based on datasets measured earlier from
582 the carbonate ore beds and black shale.
583 We propose that there were various and significant microbiological activity on the surface
584 of the sediment, and this activity might have been the source of a part of the clay mineral
585 content, which later became Fe-rich from interaction with the ore forming fluids.
586 Based on these new data, we suggest that the ascending ore-forming fluid of elevated
587 temperature generated by a high geothermal gradiant acesended along a rift zone and was the
588 source and driver of Mn-Fe-Si-rich fluids. This fluid was subjected to microbially mediated Fe-
589 oxide precipitation under neutral suboxic conditions, which characterized the depositional
590 environment; active Fe-oxide surface catalytical processes precipitated Mn oxide. This is
591 characteristic for the formation of mineralized chimney-like mounds, which were probably

stromatolites. These processes generally occurred in the feeder zone of the footwall and the Mn deposit proto-ore, which later transformed into the diagenetic rhodochrosite Úrkút ore deposit.

These new results expand the earlier proposed genetic model, and provide new evidence for elevated temperatures of the ascending ore-forming fluids and the mineralization itself, and also support a widely extended discharge feeder zone than was thought previously.

Acknowledgments

This research did not receive a specific grant from funding agencies in the public, commercial, or not-for-profit sectors. We thank the careful measurements, the technical assistance, and data interpretations by I. Fórizs, Cs. Sajgó, I. Hegyi, K. Judik, G. Szarkándi, and A. Tóth. We thank the careful reviews and constructive suggestions provided by the anonymous reviewers, and editorial handling by xy.

Figure captions

Fig. 1. The location of Úrkút manganese deposit (a) (GPS data: N 47°05'03.3''; E 17°38'30.6''); (b) a sketch geological profile; (c-d) Fe-Mn oxide indications of mineralized feeder and mound zone in the footwall limemarlstone; and in the Mn-carbonate main ore bed marked by arrows (e).

Fig. 2. Macroscopic features of the samples from the feeder and mound zone. (a) reddish goethite at the contact of the Mn oxide-bearing feeder zone and the footwall marlstone (sample 1/2); (b) manganite impregnation in the limemarlstone (sample 2/1); (c) Fe-rich (goethite) zone at the contact (sample 2/5); (d) heterogenous green-red marlstone from the feeder zone (sample 2/2), colors caused by goethite and celadonite minerals; (e) vug-filled by romanéchite and groutite at the feeder zone (sample 4/D); (f, g) hollandite, groutite, manganite, cryptomelane with goethite crust (sample 3/A); (h) stromatolite and vein-like appearance of the hollandite, groutite, manganite, cryptomelane, and goethite (sample 5/2); (i) vein-filling manganite and goethite mineral impregnations in the limemarlstone (sample 4/I). Scale: 1 cm.

Fig. 3. Representative series of photos of polished samples and thin sections (footwall limemarlstone), petrographic microscope, reflected light (a-d) and transmitted light. (a, b) laminated, micro-stromatolite-like structures (white arrows) in the Mn and Fe oxide-rich samples (polished surfaces; samples 5/1 and 1/1); (c, d) laminated stromatolite-like structures in the Mn- and Fe-rich parts of manganite and goethite (sample 3/1/D); (e) cyanobacterial perimorphs (white arrow) and green clay in the marlstone and in the Fe-rich phase (1N; sample 4/C); (f-h) enlargement series of filamentous microbial forms in the micritic marlstone (arrows; 1N; sample 4/G). For further details see Table 1, SI. 2, 3.

Fig. 4. Representative series of photos of the Fe-Mn oxide indications of the feeder and mound zone, petrographic microscope, transmitted light. (a) Fe oxide-rich filamentous microbial forms (arrow) in the pores of *Echinozoa* tests (sample 4/I); (b) calcite framework of *Echinozoa* test, crossed Nicol of (a); (c) Fe-rich filamentous microbial structures (arrow) in the pore space of *Echinozoa* test, higher magnification (sample 4/I); (d-f) *Echinozoa* test impregnated by Mn oxide (higher magnification white square in d; sample 4/F), (e, f) filamentous microbial forms with complex inner structure in the pore space of fossils (arrows); (g, h) the Fe oxide-rich impregnation of micritic matrix (arrows) and in the pore space of fossils (arrows; samples 4/F and 4/C).

Fig. 5. SEM-EDS photos of the samples (back scattered electron images). (a) different Mn oxide zones enriched in Ba (light phase) or K content (sample 2/1); (b) needle-like Mn oxide minerals at the contact zone (arrows) (sample 2/1); (c, d) euhedral dolomite in the Fe-rich part with high Mn oxide at the marginal parts (arrows; sample 2/5); (e, f) Mn oxide laminae with high Ba content in the sample (arrows; sample 4/D); (g, h) *Crinoidea* tests impregnated by Mn oxide (arrows; g-sample 2/1, h-sample 1/1); (i) calcite biodebris with Fe oxide pore filling (sample 4/C); (j) enlargement of (i) showing microbial-like structure in the Fe-rich phases (arrows; sample 4/C).

Fig. 6. Box-plot diagrams of the main (a) and selective trace element (b) distributions of 9 samples. Legend: the boxes show the distance between the lower and upper quartiles (above and below them 0.25% and 0.75% of the values can be found), and the black line in the box is the median. The vertical lines show the 1.5 distance from quartile values. Those values which are above or below this line are the outliers (o), and those, which are above or below the outliers are the extreme values (*).

Fig. 7. The stable O and C isotopic relations of the samples compared with other giant Mn-ore deposits (Úrkút, Eplény Polgári et al., 1991, 2000; Molango-Mexico Okita and Shanks, 1988; Moanda-Gabon Hein et al., 1989; and Wafangzi, Minle-Datangpo, Gaoyan, Taojiang-China, Fan et al., 1996)

Fig. 8. Raman spectroscopy line measurements along the line on sample 3/1. The organic material is enriched typically in the manganite-bearing phase, while the hollandite and cryptomelane form alternating laminae.

Fig. 9. Proposed complex genetic model for the Úrkút Mn deposit (a), modified after Polgári et al., 2004, and the Fe-Mn oxide indications of the feeder and mound zone (b); not to scale

Legend

I. Proximal feeder zone (Csárdahegy)

II. Distal feeder zone

III. Zone of distal enzymatic Mn(II) oxidation

1.) Dissolved limemarlstone footwall with sedimentary dikes, and metalliferous clay minerals above Mn-oxide infiltrated limestone (black).

2.) Proximal cherty, Fe-rich Mn oxide blocks (high Ba and Sr content) in metalliferous clay mineral assemblage.

3.) Flourishing microbial system, sequestration of metals in the form of oxides (proto-ore),

679 selective enrichment of elements.
680 4.) Distal accumulation of MnOOH and FeOOH proto-ore, green clay minerals (celadonite),
681 organic matter
682 5.) Mn nodules, Fe- and Mn-encrustations, hard grounds.
683 **General key**
684 6.) Triassic shallow platform.
685 7.) Lower-Middle Liassic limestone (a) and limemarlstone (b), shallow marine pelagic sequence.
686 8.) Submarine (a) and terrestrial (b) volcanic activity in distal areas.
687 9.) Bioherms.
688 10.) Biodebris (*Ammonites*), *Brachiopoda, Mollusca, Crinoidea, Echinoidea, Porifera,*
689 *Ostracoda*, fish, etc.).
690 11.) Plankton organisms (*Radiolaria, Foraminifera, Bositra*, etc.).
691 12.) Resedimentation.
692 A. Considerable bioproductivity on the seafloor
693 B. Hydrothermal diffuse discharge system of elevated temperature effecting the unconsolidated
694 sediment, resulting Fe and Mn oxide indication (feeder and mound zone)
695 C. Diagenesis
696 Arrows show the direction of energy and ore forming fluid input.
697 For details see Table 5 and SI. 8.
698
699 **References**
700

701 Ayupova, N., Maslennikov, V.V., Tessalina, S., Shilovsky, O.P., Sadykov, S.A., Hollis, S.P.,
702 Danyushevsky, L.V., Safina, N.P. Statsenko, E.O., 2016. Tube fossils from gossanites of
703 the Urals VHMS deposits, Russia: Authigenic mineral assemblages and trace element
704 distributions. Ore Geology Reviews. in press, DOI: 10.1016/j.oregeorev.2016.08.003

705 Bárdossy, G., Bottyán, L., Gadó, P., Griger, Á., Sasvári, J., 1980. Automated quantitave phase
706 analysis of bauxites. American Mineralogist 65, 135-141.

707 Bíró, L., 2014. The stratigraphic re-evaluation of the drillings of the manganese ore mining at
708 Úrkút. Bulletin of Hungarian Geological Society 144/1, 3–14. (in Hungarian with English
709 abstract)

710 Coplen, T.B., 2007. Calibration of the calcite–water oxygen-isotope geothermometer at Devils
711 Hole, Nevada, a natural laboratory, Geochimica et Cosmochimica Acta 71/163948-3957.

712 Cora, I., 2009. The mineralogical investigation of the carbonaceous Mn-ore of Úrkút, Hungary.
713 (Thesis), Eötvös Loránd University Department of Mineralogy, pp. 90.

714 Csontos, L., Vörös, A., 2004. Mesozoic plate tectonic reconstruction of the Carpathian region.
715 Palaeogeography Palaeoclimatology Palaeoecology 210, 1–56.

716 Dupraz, C., Visscher, P. T., 2005. Microbial lithification in marine stromatolites and hypersaline
717 mats. Trends in Micobiology 13, 429-438.
718 Fan, D., Jie, Y., Leiming, Y., Rufan, Z., 1996. The role of microbes in the formation of Mn
719 carbonate during early diagenesis — take the Gaoyan deposit as an example. In: Lianjun,
720 Ye (Ed.), Organismand Organic Matter in the Formation of Mineral Deposits. China
721 Ocean Press, Beijing, pp. 81–101.
722 Fórizs, I., Bajnóczi, B., Mozgai, V., Szabó, M., Tóth, M., 2015. The effect of non-carbonate soil
723 components on the measured isotopic composition of carbonate. Abstract, IX. ESIR
724 Conference, Eger, Hungary.
725 Frandsen, C., Legg, B. A., Comolli, L. R., Hengzhong, Z., Gilbert, B., Johnson, E., Banfield, J.
726 F., 2014. Aggregation-induced growth and transformation of β-FeOOH nanorods to
727 micron-sized α-Fe_2O_3 spinels. Cryst. Eng. Comm. 16, 1451-1458.
728 Galácz, A., Vörös, A., 1972. Jurassic history of the Bakony Mountains and interpretation of
729 principal lithological phenomena. Bulletin of Hungarian Geological Society 102/2, 122-
730 135. (in Hungarian with English abstract).
731 Haas, J., 1994. Mesozoic. University Book. Eötvös Publishing House, Budapest. 119 pp.
732 Haas, J., 2012. Influence of global, regional, and local factors on the genesis of the Jurassic
733 manganese ore formation in the Transdanubian Range, Hungary. Ore Geology Reviews
734 47, 77–86.
735 Hahn, T., 2010. Mineralogy, cement stratigraphy and geochemistry of manganese ores and host
736 rocks of the Toarcian Úrkút deposit, Hungary (Thesis), Technical University
737 Bergakademie Freiberg Faculty of Geosciences, Geoengineering and Mining Department
738 of Mineralogy, pp. 122.
739 Hein, J.R., Bolton, B.R., Nziengui, P., McKirdy, D., Frakes, L., 1989. Chemical, isotopic and
740 lithologic associations within the Moanda Manganese Deposit, Gabon. Abstracts. 28th
741 IGC. Washington DC, pp. 2–47.
742 Jach, R., Dudek, T., 2005. Origin of a Toarcian manganese carbonate/silicate deposit from the
743 Krížna unit, Tatra Mountains, Poland. Chemical Geology 224, 136–152.
744 Jaffrés, J. B. D., Graham, A., Shields, W., Klaus, W., 2007. The oxygen isotope evolution of
745 seawater: a critical review of a long-standing controversy and an improved geological
746 water cycle model for the past 3.4 billion years. Earth-Science Reviews 83/1, 83-122.

747 Jehlička, J., Edwards, H.G.M., Vítek, P., 2009. Assessment of Raman spectroscopy as a tool for
748 the non-destructive identification of organic minerals and biomolecules for Mars studies.
749 Planetary Space Science 57/5, 606-613.
750 João, T.-A., Dirkx, R., Veld, H., Klaver, G., De Boer, P.L., 2012. Toarcian black shales in the
751 Dutch Central Graben: record of energetic, variable depositional conditions during an
752 Oceanic Anoxic Event. Journal of Sedimentary Research 82, 104–120.
753 Kaeding, L., Brockamp, O., Harder, H., 1983. Submarin-Hydrothermale Entstehung der
754 Sedimentaren Mn-Lagerstatte Úrkút (Ungarn). Chemical Geolology 40, 251–268.
755 Kázmér, M., Kovács S., 1985. Permian-Paleogene paleogeography along the eastern part of the
756 Insubric-Periadriatic lineament system: Evidence for continental escape of the Bakony-
757 Drauzug unit. Acta Geologica Hungarica 28, 71–84.
758 Konhauser, K. O., Urrutia, M. M. (1999): Bacterial clay authigenesis: a common biogeochemical
759 process, Chemical Geology, 161, 399–413.
760 Konhauser, K., O. (Ed.) 2012. Fundamentals of Geobiology, Wiley - Blackwell Science Ltd,
761 New York. pp. 50-210.
762 Mandernack, K.W., Post, J., Tebo, B.M., 1995. Manganese mineral formation by bacterial spores
763 of the marine Bacillus, strain SG-1: evidence for the direct oxidation of Mn(II) to
764 Mn(IV). Geochimica et Cosmochimica Acta 59, 4393–4408.
765 Maslennikov, V.V., Ayupova, N.R., Herrington, R.J., Danyushevskiy, L.V., Large, R.R. 2012.
766 Ferruginous and manganiferous haloes around massive sulphide deposits of the Urals.
767 Ore Geology Reviews 47, 5-41.
768 Morgan, J.J., 2005. Kinetics of reaction between O_2 and Mn (II) species in aqueous solutions.
769 Geochimica et Cosmochimica Acta 69/1, 35–48.
770 Okita, P.M., Shanks III, W.C., 1988. $\delta^{13}C$ and $\delta^{33}S$ trends in sedimentary manganese deposit,
771 Molango (Mexico) and Taojiang (China): evidence for mineralization in closed system.
772 Absts., International Association for Sedimentologists. Symposium on Sedimentology
773 Related to Mineral Deposits. Beejing, pp. 188–189.
774 Pace, A., Bouton, A., Bourillot, R., Vennin, E., Visscher, P., Dupraz, C., Thomazo, C., Galaup,
775 S., Kwasniewski, A., 2015. Microbial and Physicochemical Steps Leading to the
776 Mineralization of the Great Salt Lake Microbialites, Abst., Goldschmidt Conf., 2374.

777 Pekker, P., 2005. Mineralogical investigation of the Úrkút facies of the Eplény Limestone
778 (Thesis), Eötvös Loránd University Department of Mineralogy, pp. 82.
779 Polgári, M., 1993. Manganese geochemistry reflected by black shale formation and diagenetic
780 processes — model of formation of the carbonatic manganese ore of Úrkút. Special
781 Series of Hungarian Geological Institute. Karpati Publish House, Ushgorod. 211 pp.
782 Polgári, M., Bíró, L., Pál-Molnár, E., Dobosi, G., Bajnóczi, B., Németh, T., Kis, V. K., Vigh, T.,
783 2013. Rhodocrosite-bearing concretions from a Jurassic manganese ore mineralization –
784 Úrkút, Hungary. Carpathian Journal of Earth and Environmental Sciences 8/4, 139-146.
785 Polgári, M., Hein, J. R., Bíró, L., Gyollai, I., Németh, T., Sajgó, Cs., Fekete, J., Schwark, L., Pál-
786 Molnár, E., Vido, M., Vigh, T., 2016b. Mineral and chemostratigraphy of a Toarcian
787 black shale hosting Mn-carbonate microbialites (Úrkút, Hungary). Palaeogeography
788 Palaeoclimatology Palaeoecology 459, 99-120.
789 Polgári, M., Hein, J. R., Tóth A. L., Pál-Molnár, E., Vigh, T., Bíró, L., Fintor, K., 2012b.
790 Microbial action formed Jurassic Mn-carbonate ore deposit in only a few hundred years
791 (Úrkút, Hungary). Geology 40/10, 903-906.
792 Polgári, M., Hein, J. R., Vigh, T., Szabóné-Drubina, M., Fórizs, I., Bíró, L., Müller, A., Tóth, A.
793 L., 2012a. Microbial processes and the origin of the Úrkút manganese deposit, Hungary.
794 Ore Geology Reviews 47, 87-109.
795 Polgári, M., Hein, J.R., Tóth, M., Vigh, T., Bíró, L., 2007. Did hydrothermal fluids contribute to
796 the huge Úrkút carbonate body? Abstr. Goldschmidt Conf. A801.
797 Polgári, M., Németh, T., Pál-Molnár, E., Futó, I., Vigh, T., Mojzsis, J.S., 2016a. Correlated
798 chemostratigraphy of Mn-carbonate microbialites (Úrkút, Hungary). Gondwana Research
799 29/ 1, 278-289.
800 Polgári, M., Okita, P.M., Hein, J.R., 1991. Stable isotope evidence for the origin of the Úrkút
801 manganese ore deposit, Hungary. Journal of Sedimentary Petrology 61, 384-393.
802 Polgári, M., Philippe, M., Szabó-Drubina, M., Tóth, M., 2005. Manganese-impregnated wood
803 from a Toarcian manganese ore deposit, Eplény Mine, Bakony Mts, Transdanubia,
804 Hungary. N. Jhb. Geol. Paläont. Monathefte 3, 175–192.
805 Polgári, M., Szabó, Z., Szederkényi, T. (Eds.), 2000. Manganese Ores in Hungary – In
806 Commemoration of Professor Gyula Grasselly – Hungarian Academy of Sciences. Juhász
807 Publishing House, Szeged. 675 pp.

808 Polgári, M., Szabó-Drubina, M., Szabó, Z., 2004. Theoretical model for the Mid-European
809 Jurassic Mn-carbonate mineralization Úrkút, Hungary. Bulletin of Geosciences, Czech
810 Geological Survey 79, 53–61.
811 Roy, S., 1981. Manganese Deposits. Academic Press, London. 458 pp.
812 Szabó, Z., Grasselly, Gy., 1980. Genesis of manganese oxid ore in the Úrkút basin, Hungray, In.
813 Varentsov, I. M., Grasselly, Gy. (Eds.) Geology and Geochemistry of Manganese,
814 Akadémiai kiadó (Budapest) 2 pp. 223-236.
815 Szabó, Z., Grasselly, Gy., Cseh Németh, J., 1981. Some conceptual questions regarding the
816 origin of manganese in the Úrkút Deposit, Hungary. Chemical Geology 34, 19–29.
817 Szabó-Drubina, M., 1959. Manganese deposits of Hungary. Economic Geology 54, 1078–1093.
818 Varentsov, I.M., Grasselly, Gy., Szabó, Z., 1988. Ore-formation in the early-Jurassic basin of
819 Central Europe: aspects of mineralogy, geochemistry and genesis of the Úrkút manganese
820 deposit, Hungary. Chemie der Erde 48, 257–304.
821 Veizer, J., Hoefs, J., 1976. The nature of O18/O16 and C13/C12 secular trends in sedimentary
822 carbonate rocks. Geochimica et Cosmochimica Acta 40, 1387–1395.
823 Vető, I., Demény, A., Hertelendi, E., Hetényi, M., 1997. Estimation of primary productivity in
824 the Toarcian Tethys — a novel approach based on TOC, reduced sulphur and manganese
825 contents. Palaeogeography Palaeoclimatology Palaeoecology 132, 355–371.
826 Vörös, A., Galácz, A., 1998. Jurassic palaeogeography of the Transdanubian Central Range
827 (Hungary). Riv. Ital. Paleontol. Strat. 104, 69–84.
828 Yeshaya, B., Moshe, S., 1988. The role of cell-bound flocculants in coflocculation of benthic
829 cyanobacteria with clay particles, FEMS Microbiol. Lett. 53 169-174.
830 Zavarzin, G.A., 2003. Diversity of cianobacterial mats. Krumbein W.E. (Eds.) Fossil and Recent
831 Biofilms 8, 141-150.

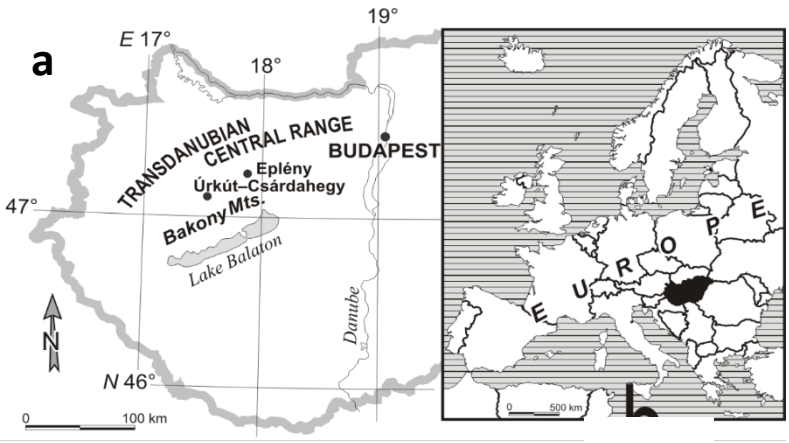
a
E 17°
18°
19°
TRANSDANUBIAN CENTRAL RANGE
BUDAPEST
Úrkút–Csárdahegy
Eplény
Mts.
Bakony
Lake Balaton
Danube
47°
N 46°
N
0
100 km
EUROPE
0
500 km
b


c


d

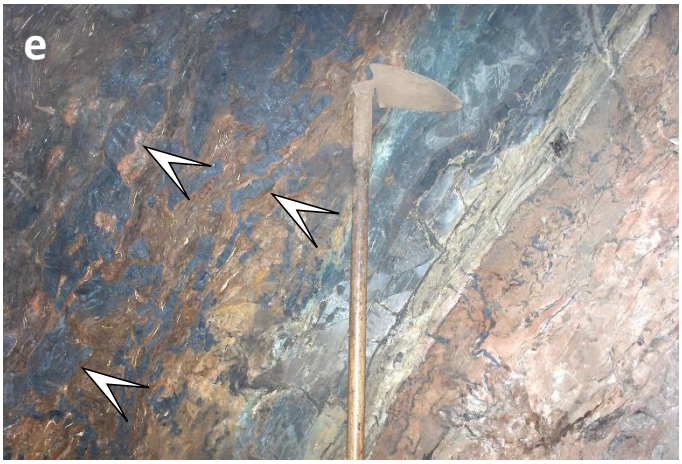
e

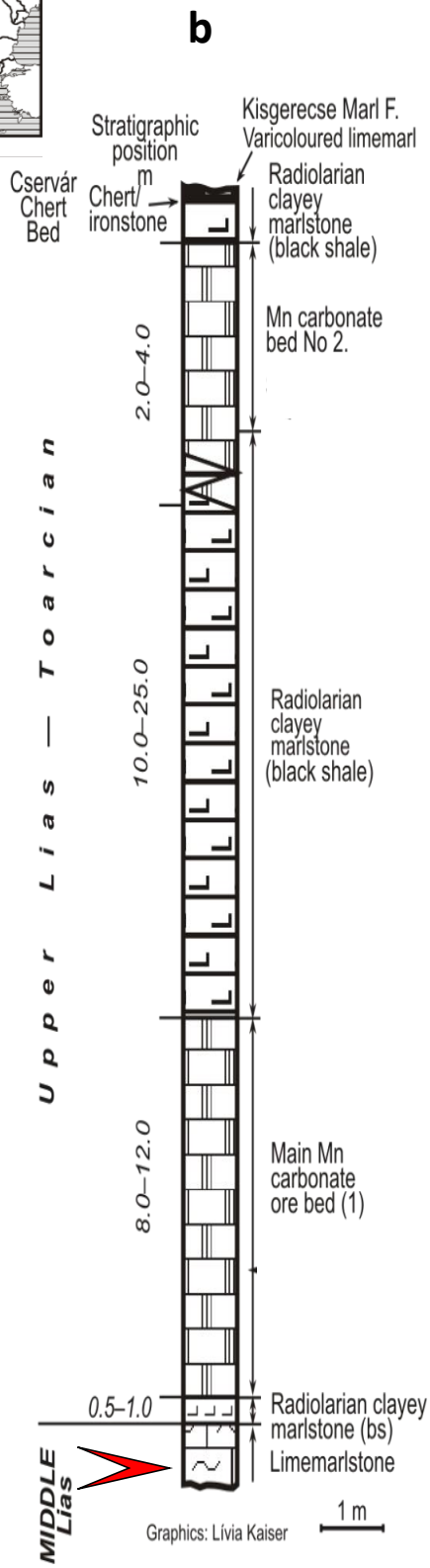
b
Stratigraphic position m
Kisgerecse Marl F.
Varicoloured limemarl
Cservár Chert Bed
Chert/ ironstone
Radiolarian clayey marlstone (black shale)
Mn carbonate bed No 2.
2.0–4.0
Upper Lias — Toarcian
10.0–25.0
Radiolarian clayey marlstone (black shale)
8.0–12.0
Main Mn carbonate ore bed (1)
0.5–1.0
Radiolarian clayey marlstone (bs)
Limemarlstone
MIDDLE Lias
1 m
Graphics: Lívia Kaiser

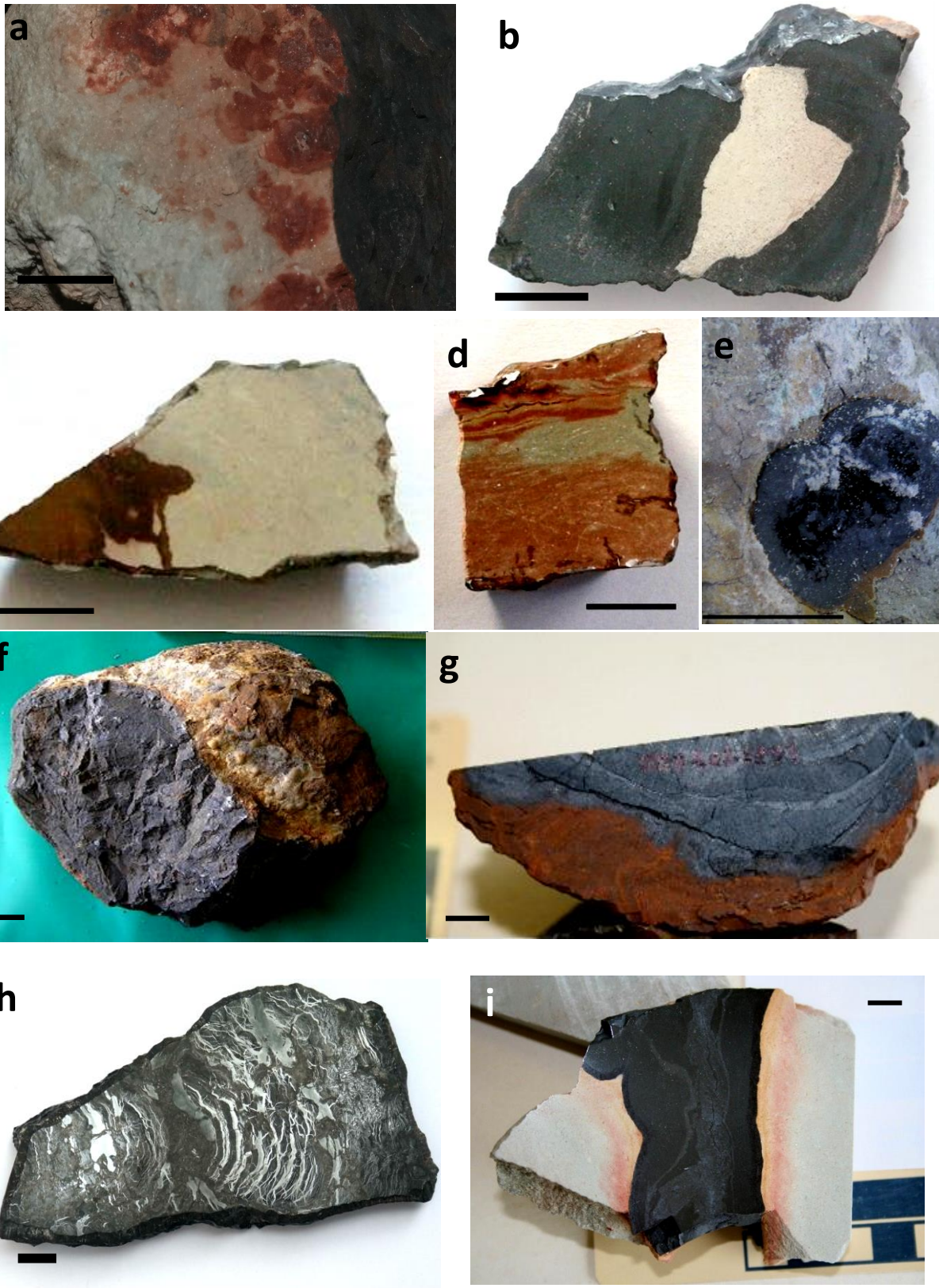
a
b
c
d
e
f
g
h
i

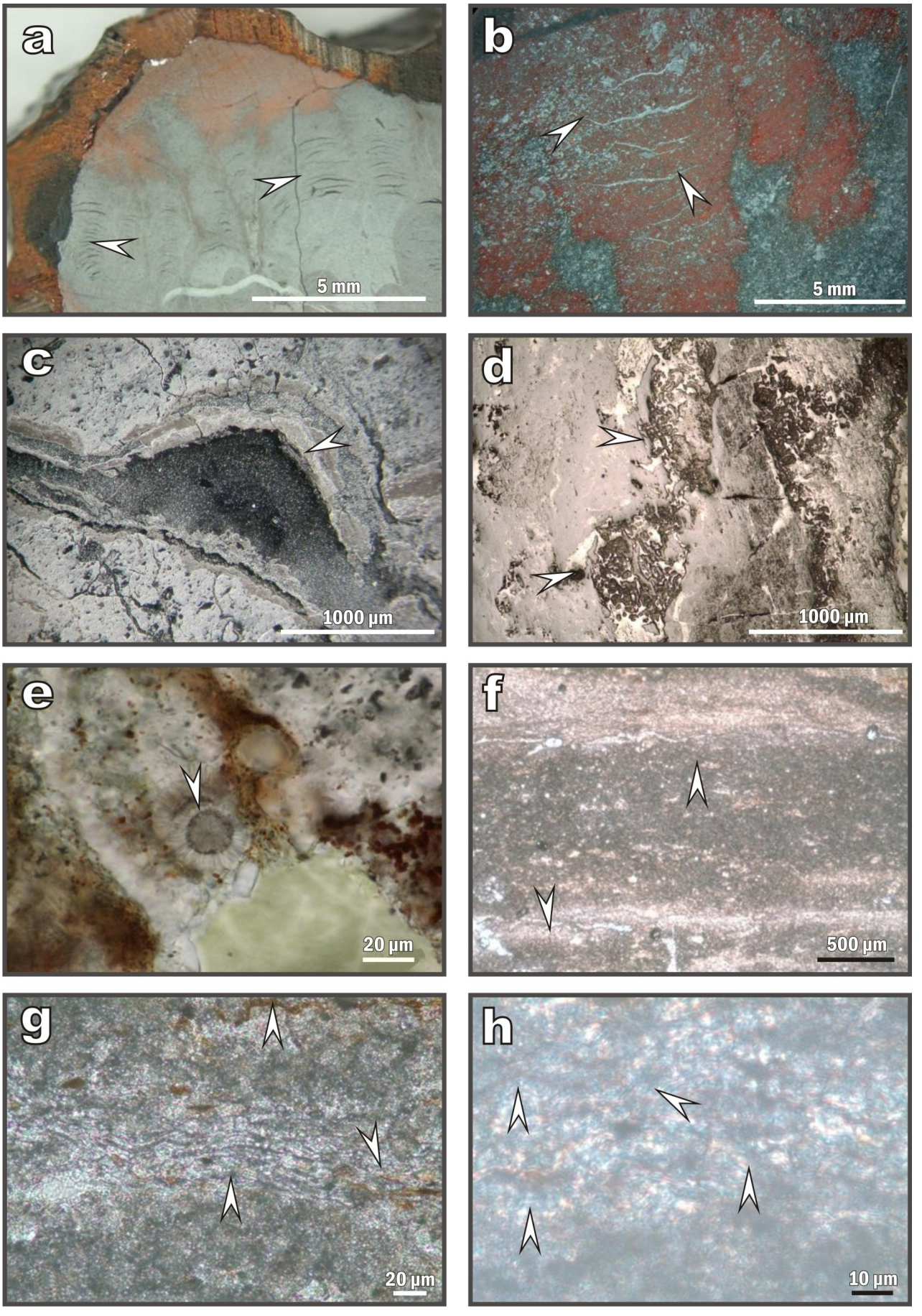
a
5 mm
b
5 mm
c
1000 µm
d
1000 µm
e
20 µm
f
500 µm
g
20 µm
h
10 µm

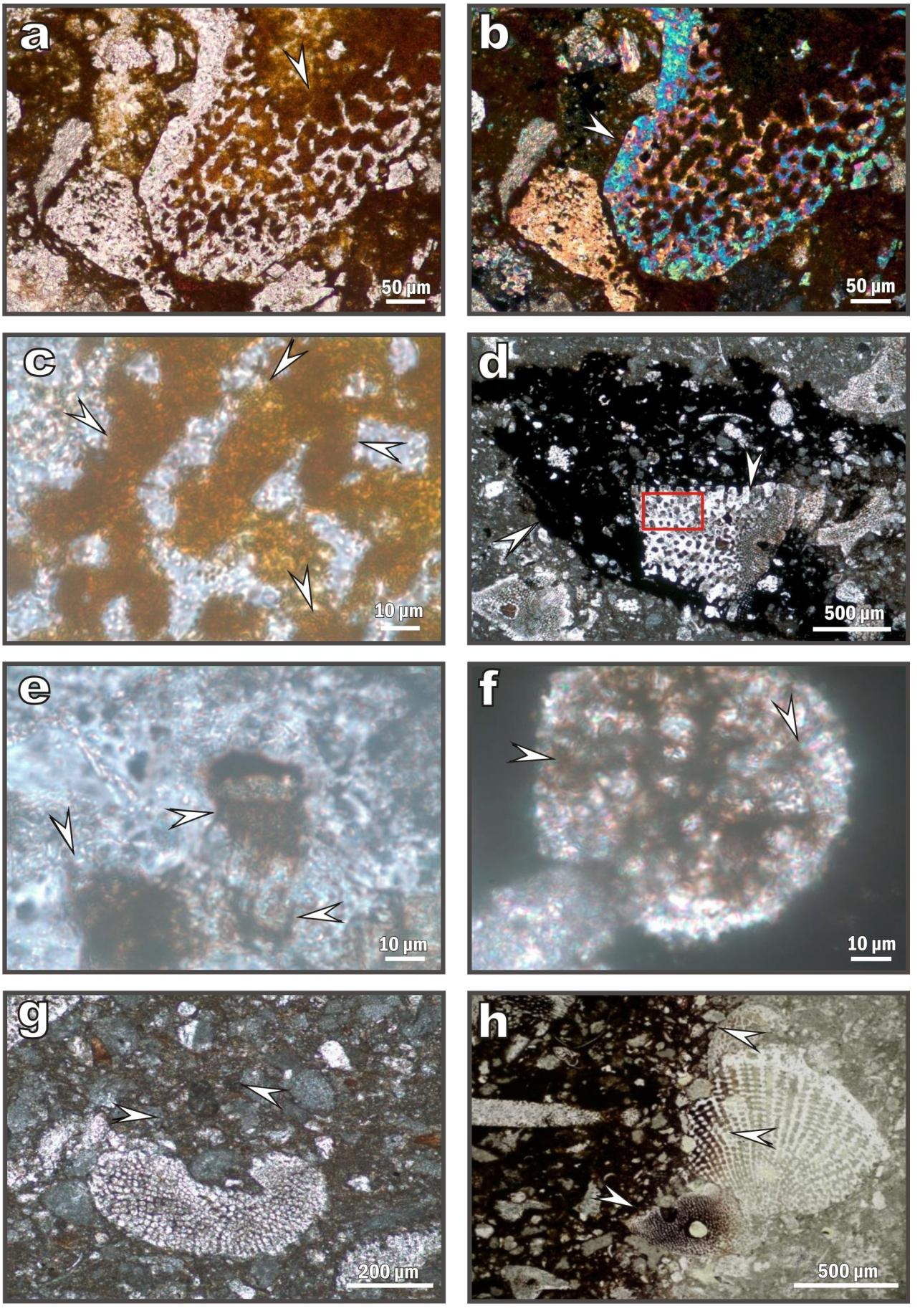
a
50 µm
b
50 µm
c
10 µm
d
500 µm
e
10 µm
f
10 µm
g
200 µm
h
500 µm

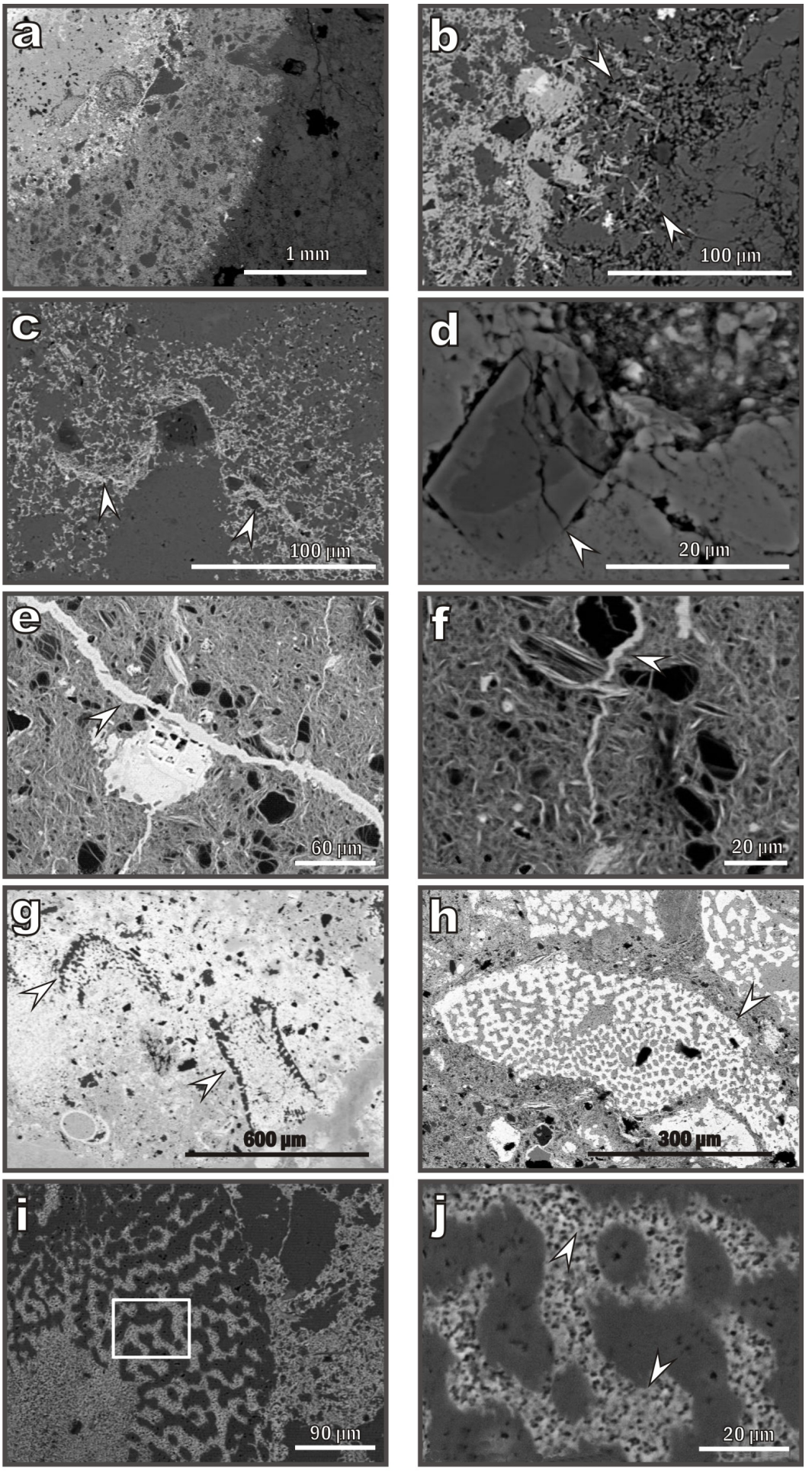
a
1 mm
b
100 µm
c
100 µm
d
20 µm
e
60 µm
f
20 µm
g
600 µm
h
300 µm
i
90 µm
j
20 µm

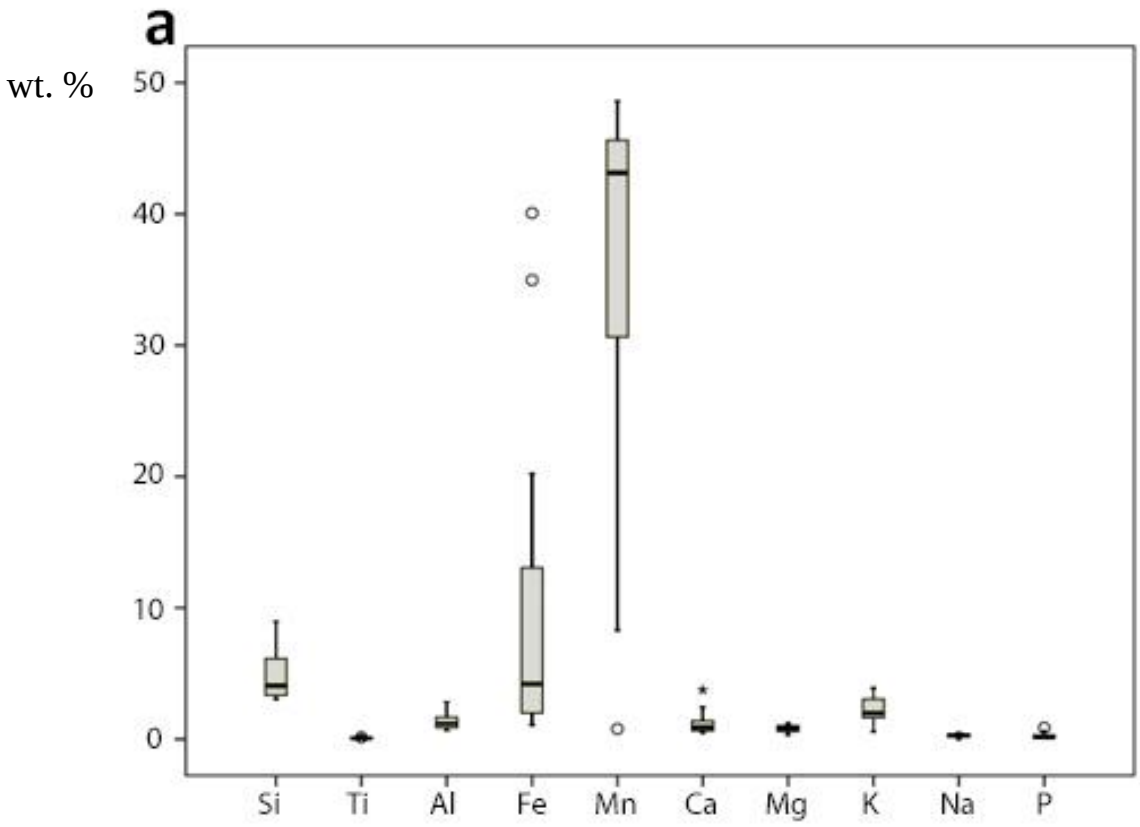
a
wt. %
50
40
30
20
10
0
Si
Ti
Al
Fe
Mn
Ca
Mg
K
Na
P

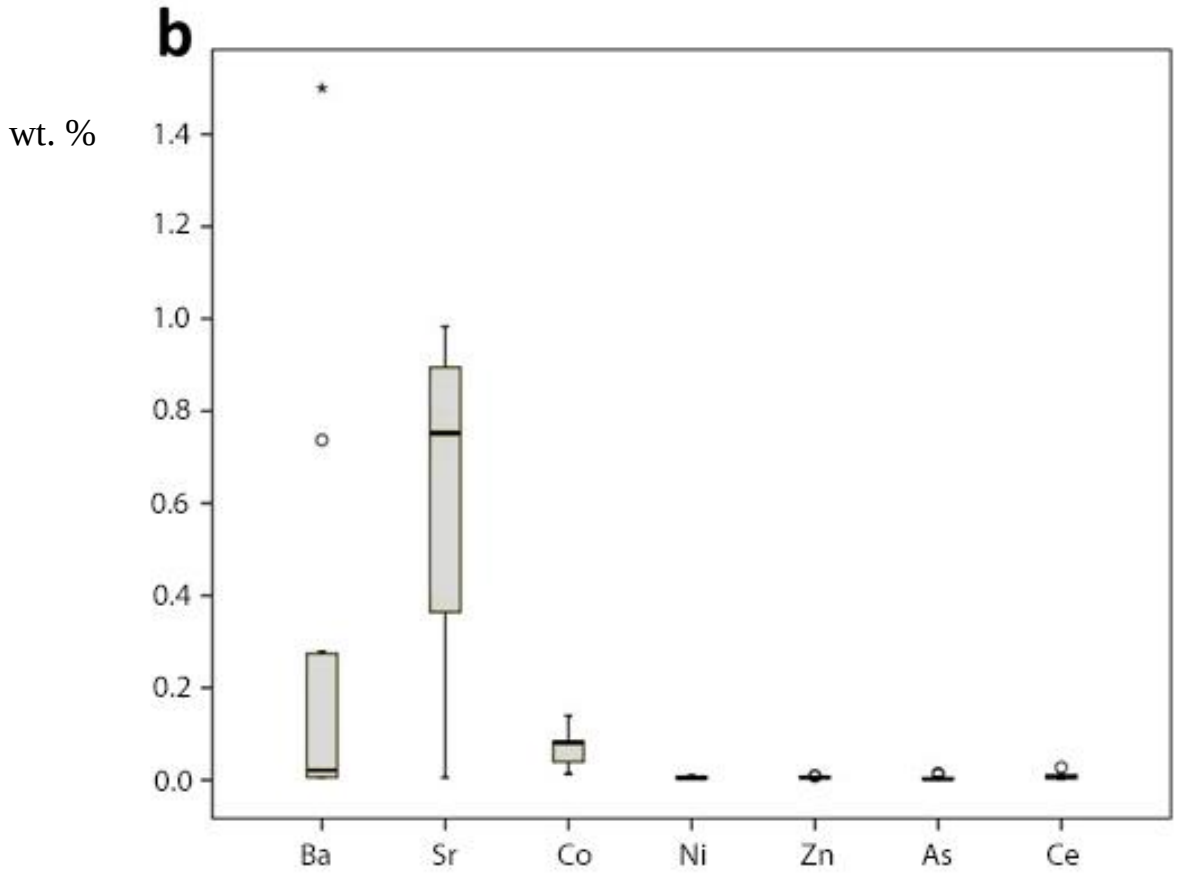
b
wt. %
1.4
1.2
1.0
0.8
0.6
0.4
0.2
0.0
Ba
Sr
Co
Ni
Zn
As
Ce

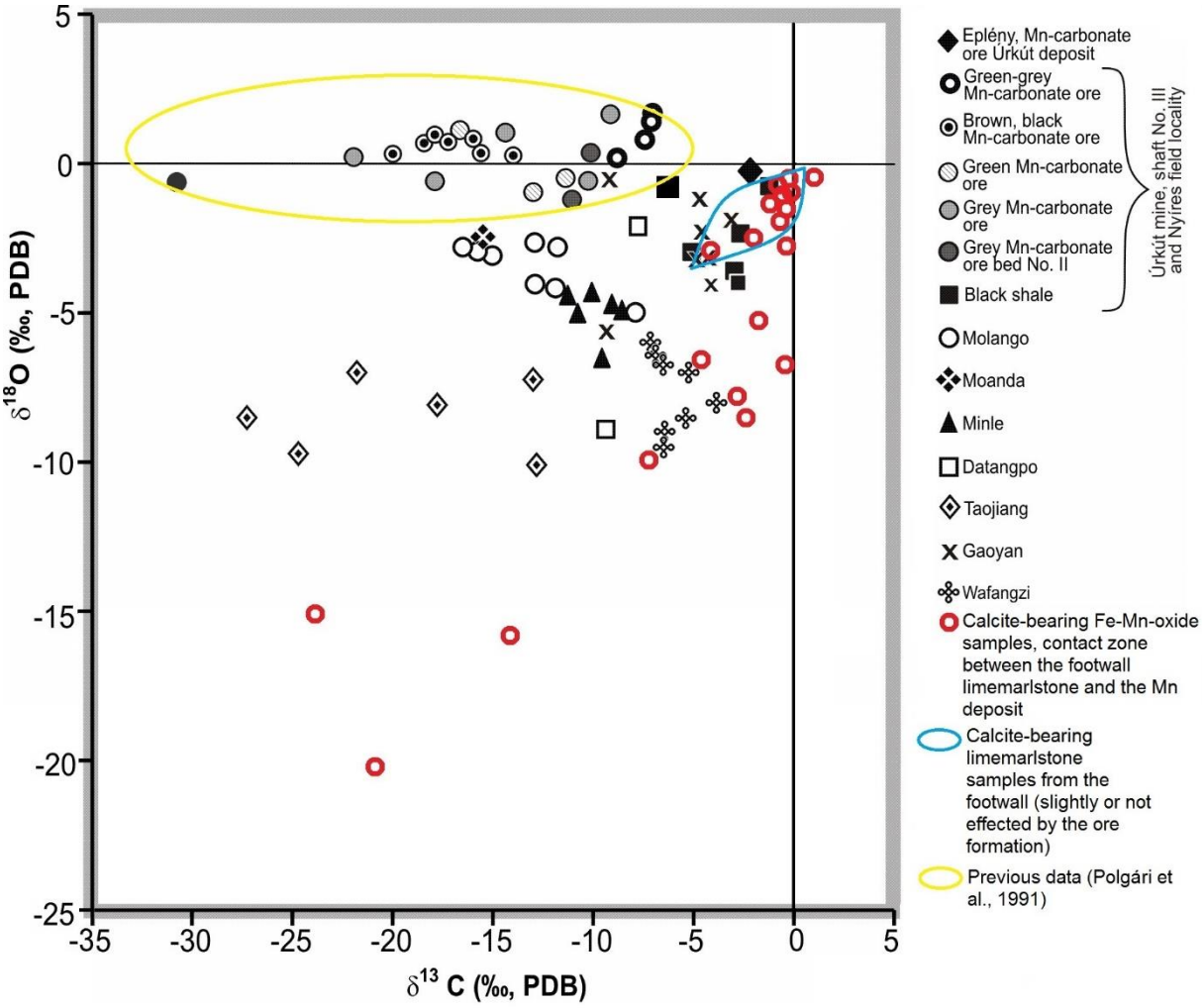
5
0
-5
-10
-15
-20
-25
-35
-30
-25
-20
-15
-10
-5
0
5
δ18O (‰, PDB)
δ13 C (‰, PDB)
Eplény, Mn-carbonate ore Úrkút deposit
Green-grey Mn-carbonate ore
Brown, black Mn-carbonate ore
Green Mn-carbonate ore
Grey Mn-carbonate ore
Grey Mn-carbonate ore bed No. II
Black shale
Úrkút mine, shaft No. III and Nyíres field locality
Molango
Moanda
Minle
Datangpo
Taojiang
Gaoyan
Wafangzi
Calcite-bearing Fe-Mn-oxide samples, contact zone between the footwall limemarlstone and the Mn deposit
Calcite-bearing limemarlstone samples from the footwall (slightly or not effected by the ore formation)
Previous data (Polgári et al., 1991)

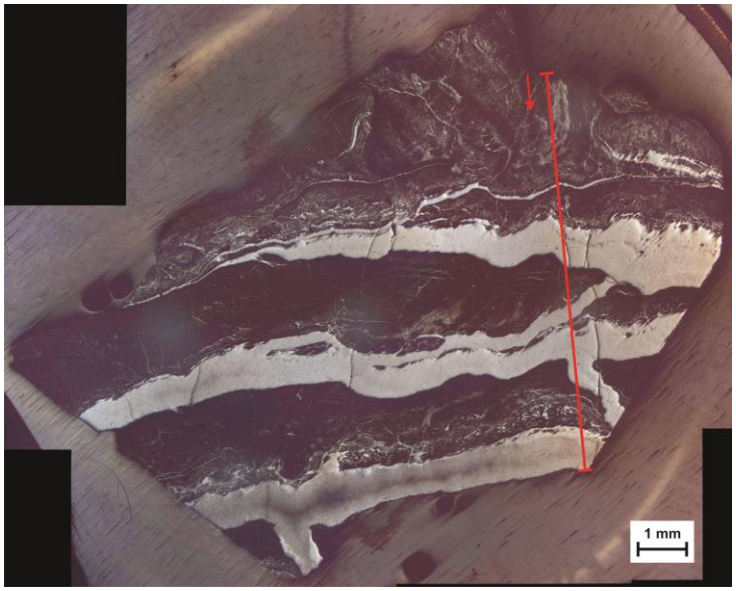
1 mm

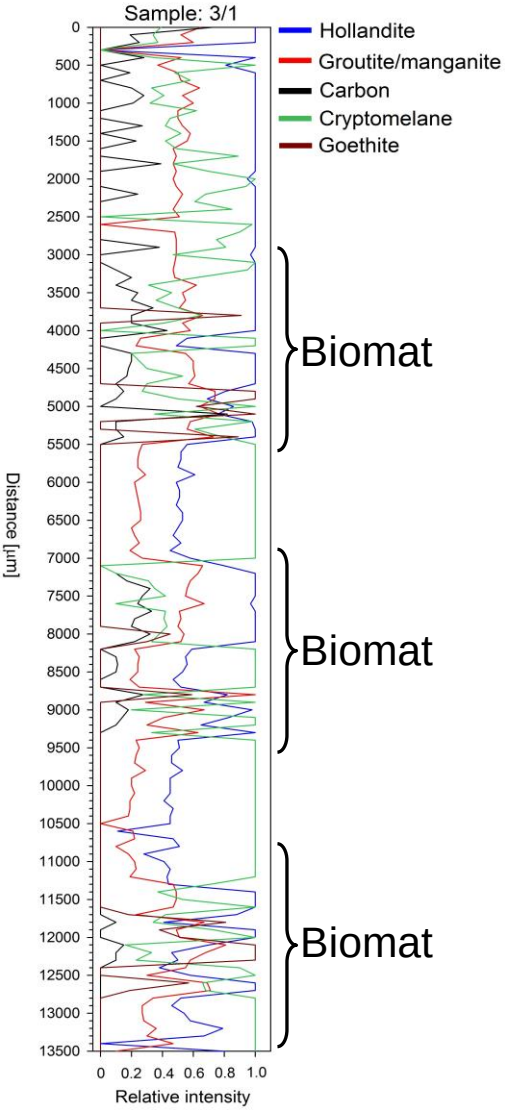
Sample: 3/1
Hollandite
Groutite/manganite
Carbon
Cryptomelane
Goethite
Biomat
Biomat
Biomat
Distance [µm]
0
500
1000
1500
2000
2500
3000
3500
4000
4500
5000
5500
6000
6500
7000
7500
8000
8500
9000
9500
10000
10500
11000
11500
12000
12500
13000
13500
0 0.2 0.4 0.6 0.8 1.0
Relative intensity

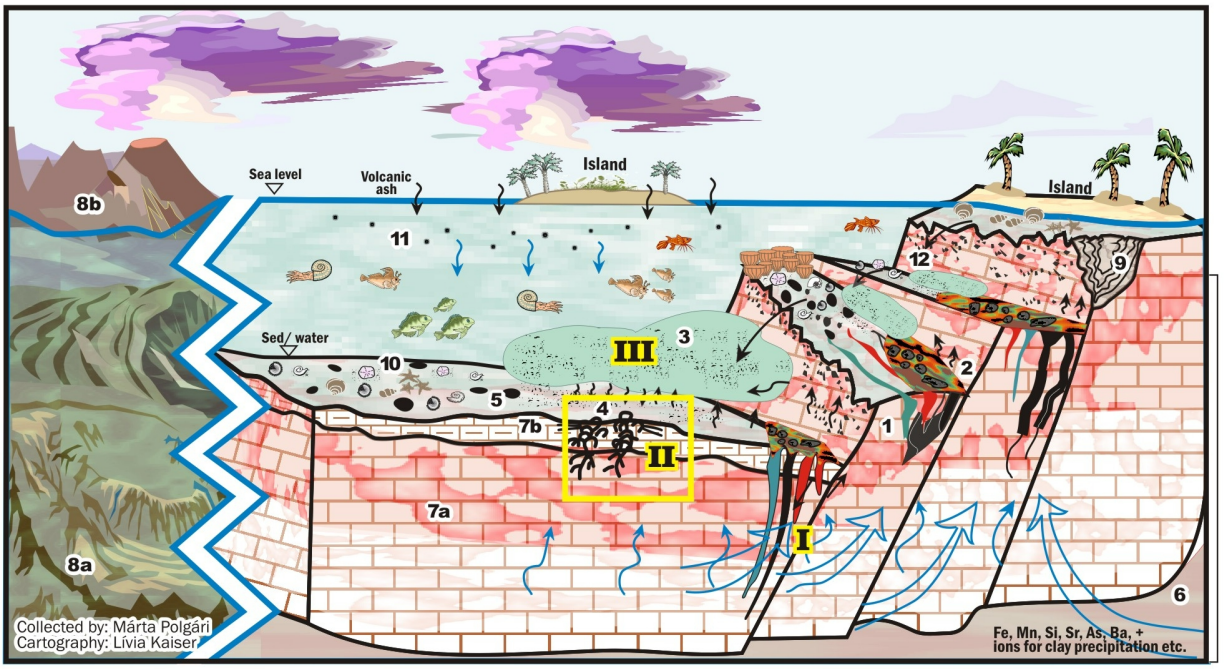
a
Sea level
Volcanic ash
Island
Island
8b
11
12
9
Sed./ water
10
III
3
2
5
4
7b
II
1
7a
I
8a
6
Collected by: Márta Polgári
Cartography: Lívia Kaiser
Fe, Mn, Si, Sr, As, Ba, + ions for clay precipitation etc.
250 m

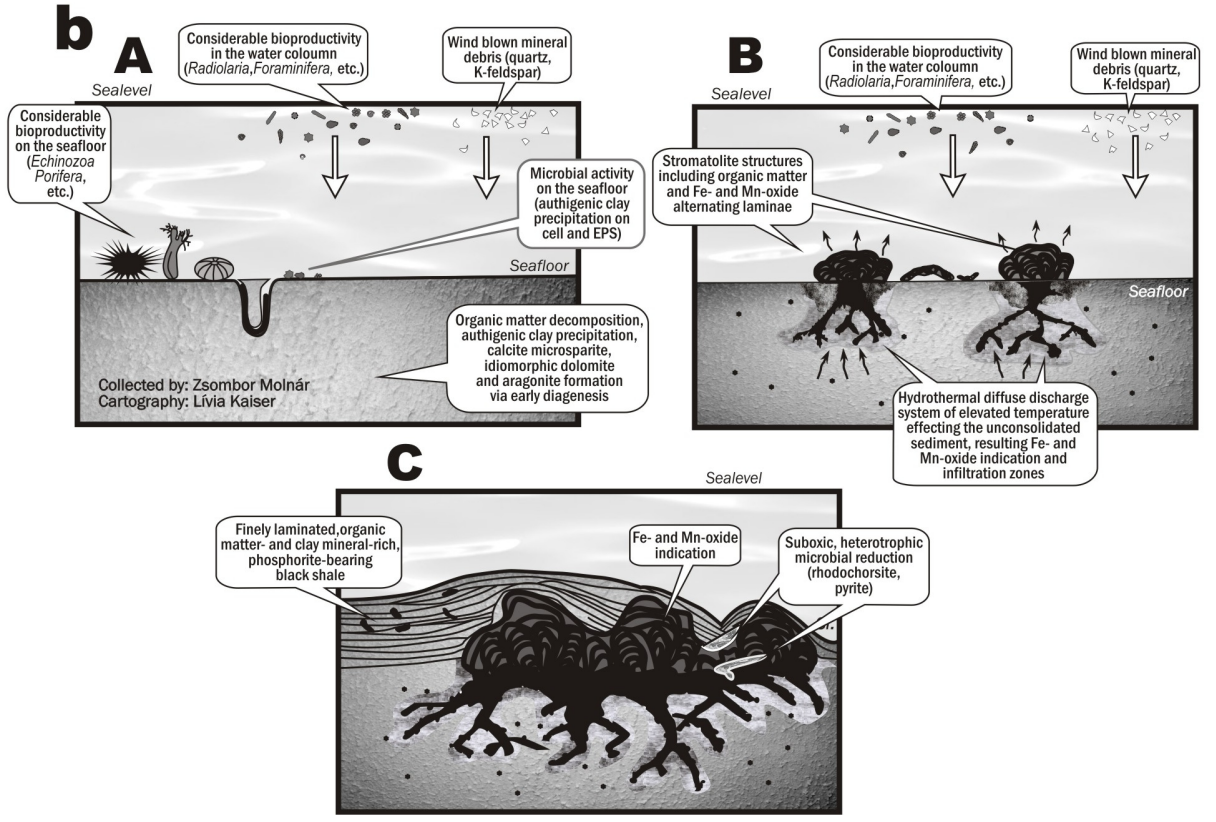
b
A
Considerable bioproductivity in the water coloumn (Radiolaria,Foraminifera, etc.)
Wind blown mineral debris (quartz, K-feldspar)
Sealevel
Considerable bioproductivity on the seafloor (Echinozoa Porifera, etc.)
Microbial activity on the seafloor (authigenic clay precipitation on cell and EPS)
Seafloor
Organic matter decomposition, authigenic clay precipitation, calcite microsparite, idiomorphic dolomite and aragonite formation via early diagenesis
Collected by: Zsombor Molnár
Cartography: Lívia Kaiser
B
Considerable bioproductivity in the water coloumn (Radiolaria,Foraminifera, etc.)
Wind blown mineral debris (quartz, K-feldspar)
Sealevel
Stromatolite structures including organic matter and Fe- and Mn-oxide alternating laminae
Seafloor
Hydrothermal diffuse discharge system of elevated temperature effecting the unconsolidated sediment, resulting Fe- and Mn-oxide indication and infiltration zones
c
Sealevel
Finely laminated,organic matter- and clay mineral-rich, phosphorite-bearing black shale
Fe- and Mn-oxide indication
Suboxic, heterotrophic microbial reduction (rhodochorsite, pyrite)

Table 1. – List of samples and methods used

Samples			Methods										
Section	**ID**	**Features**	**A**	**B**	**C**	**D**	**E**	**F**	**G**	**H**	**I**	**J**	**K**
Section 1 from Úrkút, Shaft No. III, western minfield, IV -2/4 mining block, +186 mBf mining area													
1/1	1/1/A	Black oxide ore with small radial crystals	X	X		X		X					
	1/1/B	Black oxide ore with phanerocrsyts	X	X		X		X					
	1/1/C	Black oxide ore with fine grains		XY		X	X	X	X	X	XY		X
	1/1/D	Fine laminated brown oxide ore	X	XY		X	X	X	X	X	XY		
1/2	1/2/A	Black oxide ore with fine grains	X	X		X		X	X	X	Y		X
	1/2/B	Greenish white marlstone	X			X		X		X	Y		
	1/2/C	Red contact zone	X										
Section 2 from Úrkút, Shaft No. III, western minfield, IV -2/4 mining block, +192 mBf mining area													
2/1	2/1/A	Black oxide ore	X	XY		X	X	X	X	X	Y		
	2/1/B	Red contact zone	X			X		X		X	Y		
	2/1/C	Greyish white limestone	X	XY		X	X	X	X	X	Y		X
2/2	2/2/A	Reddish marlstone	X	XY	X	X		X					X
	2/2/B	Greenish marlstone	X	XY	X	X		X					
	2/2/C	Greensih yellow marlstone	X										
	2/2/D	Greensih yellow phanerocrsyts	X										
2/3	2/3/A	Reddish marlstone	X	Y	X	X		X					X
	2/3/B	Yellowish spots	X										
	2/3/C	Ellipsoidal form on the surface	X										
	2/3/D	Greenish spots	X										
2/4	2/4/A	White limestone	X	Y		X		X					X
	2/4/B	Greyish marlstone	X	XY		X		X					
	2/4/C	Greenish spots	X			X		X					
	2/4/D	White limestone	X	XY						X	Y		
	2/4/E	Greenish ring-like contact zone	X	XY									
	2/4/F	Black shale	X	XY	X	X		X					X
2/5	2/5/A	White limestone with fossils	X	XY	X	X		X	X				
	2/5/B	Fe-rich contact zone with yellow spots	X	XY	X	X		X	X				
	2/5/C	Fe-rich contact zone	X	XY	X	X		X	X				
2/6	2/6/A	Black oxide ore	X	XY									X
	2/6/B	Black oxide ore	X	XY									X
	2/6/C	Black oxide ore	X	XY									X
Section 3 from Úrkút, Shaft No. III, deep level, points of +180 mBf													
3	3/A	Oxide ore with laminated structures		X								X	
	3/B	Oxide ore with laminated structures		X								X	
	3/C	Oxide ore with laminated structures	X	X									X
	3/D	Oxide ore with laminated structures											X

Samples			Methods										
Section	**ID**	**Features**	**A**	**B**	**C**	**D**	**E**	**F**	**G**	**H**	**I**	**J**	**K**
Section 4 from Úrkút, Shaft No. III, deep level, points of +180 mBf													
4	4/A	Black oxide ore	X	X		X				X	Y		
	4/B	Contact zone of the ore and marlstone	X	X		X				X	Y		
	4/C	Contact zone of the ore and limestone		X			X		X		X		
	4/D	Bubble-like ore structure	X	X			X		X			X	
	4/E	Mn oxide vein-like impregnation	X	X									X
	4/F	Mn oxide spotted marlstone	X	X									X
	4/G		X	X									X
	4/H		X	X									X
	4/I		X	X									X
	4/J								X				
	4/K								X				
	4/L								X				
	4/M								X				
	4/N								X				
	4/O								X				
	4/P								X				
	4/Q												X
Section 5 from Eplény, western minfield													
5	5/A	Fine laminated oxide ore	X	X								X	
	5/B	Fine laminated oxide ore	X	X									
	5/C	Fine laminated oxide ore	X	X									

Legend: A – Macroscopic observations, B – Stereo microscope (X) and petrographic microscope (Y), C - Cathodoluminescence microscope (CL), D - X-ray powder diffraction (XPD), E - Micro x-ray diffraction (μXRD), F - Mass spectrometry (MS), G – Scanning – electron microscope (SEM-EDS), F – Gas - chromatography mass spectroscopy (GC-MS), I - Fourier transform infrared spectroscopy (FTIR) (X) and Attenuated total reflectance Fourier transform infrared spectroscopy (ATR FTIR) (Y), J – Raman – spectroscopy, K – Chemical analysis (ICP, XRF, MP-AES)

The archive samples can be found at the storage of MTA Institute for Geological and Geochemical Research. The arcive ID-s of the samples are: 1/1-1/2 – CH 07011311 - CH 07011312; 2/1-2/5 – CH 07011331 - CH 07011335; 2/6 – CH01031308; 3/A – OX03011801; 3/B – OX06092801; 3/C – OX06092802; 3/D – OX03021801 4/A – 1/4PM; 4/B – D2; 4/C – 13030311; 4/D – 1.11.A; 4/E – 5/030311; 4/F – 6/030311; 4/G – 2/030311; 4/H – 6/030312; 4/I – CH05071301; 4/J – 030311KR; 4/K – 4/0303115; 4/L – 1.8; 4/M – OX03021802; 4/N – EA3; 4/O – EA2; 4/P – 1/4; 4/Q – 1/030311; 5/1 – Ep. 1; 5/2 – Ep. 2; 5/3 – Ep. 3

Table 2. Main- (wt. %) and trace element composition (ppm) of Fe-Mn oxides and limemarlstone (samples 2/1/A, 2/2/A, 2/4/b)

ID	Si	Al	Fe	Mn	Mg	Ca	Na	K	Ti	P	S	Ag	As	Ba	Be	Bi	Cd	Co	Cr	Cu	Ga	Ge	Hf
	wt. %											ppm											
3/1/B	8.97	2.84	40.1	0.77	1.12	0.48	<0.01	1.45	0.19	0.23	<0.01	0.03	73	63	2.6	0.17	<0.02	151	32	8.3	9.3	0.5	1.47
3/1/C	3.29	1.24	3.75	42.1	0.81	1.99	0.40	2.26	0.07	0.62	I.S.	I.S.	I.S.	I.S.	I.S.	I.S.	I.S.	I.S.	I.S.	I.S.	I.S.	I.S.	I.S.
3/1/D	3.39	0.67	4.64	44.2	0.58	1.27	0.29	3.12	0.05	0.39	0.24	<0.02	13	62	1.3	<0.04	0.11	814	8	31	11	0.1	0.32
2/6/A	5.28	1.48	1.20	44.4	0.59	0.82	0.39	2.98	0.09	0.10	0.22	0.02	10	2420	1.2	0.13	0.21	852	13	85.7	10	<0.1	0.49
2/6/B	5.28	1.49	1.75	42.0	0.87	1.01	0.40	1.88	0.08	0.14	0.22	0.03	20	7370	1.2	0.25	0.17	1360	11	26	11	0.60	0.60
2/6/C	3.85	1.00	1.08	48.6	0.31	0.41	0.27	3.91	0.07	0.10	0.25	0.04	10	2780	1.0	0.18	0.2	595	8	41	11	<0.1	0.45
4/Q	3.12	1.13	5.90	46.8	0.39	0.54	<0.01	0.56	0.08	0.17	0.21	<0.02	24	60	1.7	0.06	<0.02	136	13	43	12	0.2	0.67
4/E	4.27	1.03	2.20	44.2	1.18	0.99	0.48	1.88	0.06	0.07	0.24	0.04	29	2710	1.3	0.27	0.1	1400	10	56	10	0.1	0.45
4/F	6.96	1.84	4.89	29.9	1.19	3.06	0.36	1.80	0.06	0.86	0.20	<0.02	119	>10000	1.4	0.14	<0.02	834	17	6.1	15	0.3	0.45

ID	Li	Mo	Nb	Ni	Pb	Rb	Sb	Sc	Sn	Sr	Ta	Te	Th	Tl	U	V	W	Y	Zn	Zr	La	Ce	Tb	Yb	Lu
	ppm																								
2/6/A	9	8.55	2.7	33	9.6	36	0.22	3.5	0.4	9830	0.22	0.9	2.2	0.6	1.1	36	0.8	6	50	25	12.4	26	0.23	0.8	0.13
2/6/B	11	13	4.6	48.7	8.2	34	0.27	4.6	0.9	9650	0.32	0.6	2.5	1.5	1.2	46	0.7	16	60	32	25.6	54	0.49	2.1	0.33
2/6/C	7	9.0	2.9	26	4.6	31	0.26	3.7	0.5	6950	0.21	0.3	2.0	0.8	1.1	33	0.5	5	58	22	14.4	29	0.20	0.8	0.11
3/1/B	12	2.38	13	99.8	12	51	4.7	7.8	0.9	51	1.36	0.5	4.2	0.2	0.6	97	27	27	43	81	50	159	0.91	2.8	0.40
3/1/C	I.S.	I.S.	I.S.	I.S.	I.S.	I.S.	I.S.	I.S.	I.S.	I.S.	I.S.	I.S.	I.S.	I.S.	I.S.	I.S.	I.S.	I.S.	I.S.	I.S.	I.S.	I.S.	I.S.	I.S.	I.S.
3/1/D	6	7.79	3.1	51	14	22	1.34	1.3	<0.3	8000	0.27	0.1	0.9	0.2	0.6	43	4	33	47	18	32.2	106	0.76	2.1	0.29
4/Q	4	9.88	7.4	85.6	22	18	1.32	3.0	0.3	98	0.31	0.3	1.7	0.1	1.2	24	7.7	21	24	37	27.9	114	0.76	1.7	0.24
4/E	8	11	2.8	41	21	27	0.58	3.0	0.5	8880	0.21	1.0	2.0	1.0	1.7	38	1.6	12	59	24	30.7	67	0.46	1.5	0.22
4/F	14	8.6	3.3	31	38	37	1.29	4.6	0.7	9020	0.44	0.5	3.6	0.8	2.2	41	7.1	70	56	25	75.4	275	2.71	4.8	0.68

All values for Cs, In, and Se less than detection limits except In for 3/1/B=0.03 ppm: Cs<5 ppm, In<0.2 ppm, Se<2 ppm; nd: no data

ID	Al	Fe	Mn	Mg	Ca	Na	K	Ti	As	Co	Cr	Ni	Zn	V
	wt. %								ppm					
5/A	0.35	3.06	45.4	0.34	0.41	0.11	2.95	0.0010	89	385	4.2	nd.	40	580
5/B	0.59	3.43	36.2	0.94	1.63	0.18	1.55	0.0008	109	1264	2.1	78	46	690
5/C	0.96	5.30	39.1	0.63	1.41	0.26	2.27	0.0017	164	507	11	22	159	1110
1/1/C	0.33	4.14	28.3	0.34	0.41	0.19	0.49	0.0012	120	269	3.1	nd.	31	394
1/2/A	0.23	0.89	45.3	0.36	3.48	0.15	2.18	0.0039	45	817.	2.3	64	100	383
2/1/A	0.12	0.13	0.61	0.32	18.5	0.06	0.04	nd.	24	205	1.6	1.6	nd.	242
2/2/A	0.41	0.41	0.22	1.88	15.7	0.06	0.27	0.0003	29	147	7.4	15	6.1	481
2/3/A	0.35	0.37	0.14	1.35	9.96	0.04	0.24	0.0002	5.7	96	6.0	13	10	357
2/4/F	0.52	1.21	2.11	1.14	8.66	0.06	0.45	0.0002	28	263	7.7	21	16	536
2/4/B	0.39	0.54	4.51	1.10	14.4	0.09	0.31	nd.	14	170	6.4	11	10	433

Table 3. C and O isotope data of the samples (A) and temperature calculation (B)

A ID	δC_{PDB} (‰)	δO_{PDB} (‰)	δO_{SMOW} (‰)
1/1/C	-21.35	-20.35	9.93
1/1/D	-14.35	-15.73	14.69
1/2/A	-5.13	-7.28	23.41
1/2/B	0.64	-1.25	29.62
1/2/C	-1.02	-2.54	28.30
2/1/A	-8.74	-11.38	19.17
2/1/B	0.45	-1.67	29.19
2/1/C	0.06	-2.26	28.58
2/2/A	0.34	-1.13	29.75
2/2/B	0.45	-1.41	29.45
2/3/A	0.27	-1.01	29.87
2/4/A	0.16	-1.05	29.83
2/4/C	2.35	-2.04	28.81
2/4/F	-4.57	-3.33	27.48
4/J	-0.99	-2.51	28.32
4/K	-3.72	-8.61	22.03
4/L	-2.44	-9.23	21.4
4/M	-24.02	-15.17	15.27
4/N	1.31	-0.85	30.04
4/O	-2.28	-5.27	25.47
4/P	-0.74	-7.65	23.02

B Sample ID	$\delta\ ^{18}O_{calcite}$/ $\delta\ ^{18}O_{SMOW}$ (‰)	$\delta\ ^{18}O_{water}$ / $\delta\ ^{18}O_{SMOW}$	α (calcite-water)	Temperature (°C)
1/1/C	9.93	0	1.00993	161
1/1/D	14.69	0	1.01469	115
1/2/A	23.41	0	1.02341	53
1/2/B	29.62	0	1.02962	20
1/2/C	28.3	0	1.0283	26
2/1/A	19.17	0	1.01917	80
2/1/B	29.19	0	1.02919	22
2/1/C	28.58	0	1.02858	25
2/2/A	29.75	0	1.02975	19
2/2/B	29.45	0	1.02945	20
2/3/A	29.87	0	1.02987	18
2/4/B	29.83	0	1.02983	19
2/4/C	28.81	0	1.02881	24
2/4/F	27.48	0	1.02748	30
4/J	28.32	0	1.02832	26
4/K	22.03	0	1.02203	61
4/L	21.4	0	1.0214	65
4/M	15.27	0	1.01527	110
4/N	30.04	0	1.03004	18
4/O	25.47	0	1.02547	41
4/P	23.02	0	1.02302	55

(Legend: gray – samples form the Fe-Mn-oxide indications; normal – samples from the footwall limemarlstone (slightly or not affected by the ore formation)

Calculation made after Coplen (2007); $\delta\ ^{18}O_{water}/\delta\ ^{18}O_{SMOW}$ for Jurassic marine seawater was carried out by Veizer and Hoefs (1976)

Table 4. Mineral phases and organic compounds by FTIR (Sample No. 1/C (A) and 4/C (B)

A

Measuring points	1	2	3	4	5	6	7	8	9	10	11
Ferrihydrite		X	X			X	X	X	X	X	
Maghemite		X			X	X	X	X	X	X	
Rhodochrosite	X		X	X	X					X	X
Quartz (Si-O)		X						X			
Akaganeite						X					
(CO_3)								X	X		
Chlorite			X		X					X	
Clay (Si-O)		X								X	
(Si-O)			X				X				
(v3 PO_4)		X		X		X*		X	X*	X	
(C-O)						X		X			
(CO)							X				
(CH_2)				X	X		X		X		X
Amide I				X	X		X		X		X
Amide II											
(C=C)	X		X	X	X		X				X
COOH	X						X				X
(CO)									X		
(CO)			X		X		X		X		
(CH) sym.	X		X		X		X		X		X
(CH) asym.	X		X		X		X		X		X

B

Measuring points	1	2	3	4	5	6	7	8	9	10
Ferrihydrite					X		X		X	X
Maghemite			X			X		X		
Goethite			X		X	X	X		X	X
Akanageite			X		X	X	X	X	X	X
Rhodochrosite	X	X		X				X		
Quartz(Si-O)										
CO_3	X	X	X	X	X	X	X	X	X	
Chlorite			X	X		X	X			
Clay (Si-O)					X			X		
(Si-O)		X							X	X
(PO_4)				X*				X		
(C-O-C);(C-C)								X		
(C-O)		X							X	
(CO)								X		
CO3										
CH2						X	X		X	X
(CN)(C-H) variable.				X					X	
Amide I			X	X	X	X	X		X	X
(COOH)								X	X	X
(C-H) sym.			X	X	X	X	X		X	X
(C-H) assym.			X	X	X	X	X		X	X
(NH_4)			X						X	X
(C-H) aromatic ring					X	X	X			

For details see Table 1 and SI. 6.

Table 5. Proposed genetic model for the Fe-Mn oxide indication of feeder and mound zone

Late diagenesis	**Diagenesis in suboxic environment** Normal sea water under low temperature (Eh: 0 - +0.2 V, (DO 0 – 0.2 mL/L), dysoxic environment (DO 0.2 - 2 ml/l), and heterotrophic, suboxic microbial metabolism, biogenic (silica segregation during the stabilization of ferrihydrite and the dissolution of *Porifera* spiculae) and mainly abiogenic (hydrothermal exhalation) silicification	
	Evidence: $\delta^{18}O_{SMOW}$: 27.48 ‰; $\delta^{13}C_{PDB:}$ -4.57 ‰; pr/ph relation; the local appearance of rhodochrosite (heterotroph Mn reduction), pyrite (heterotroph sulfate reduction), high Si-content (quartz, chert)	
Ore mineralization (indication)	**The appearance of the Fe-Mn oxide indication in a poorly consolidated footwall limemarl as the result of ascending hydrothermal activity of elevated temperature** Normal salinity, neutral pH (6-8), aerobic (DO>2 ml/l), redox environment (Eh: +0.4- +1.0) affected by hydrothermal system (~80-100° C), with low S content (**A**). The main cause of the ore genesis is the microbial oxidation of the Fe^{2+}, based on these the precipitation and oxidation of Mn^{2+} with oxide surface catalysis (hollandite, cryptomelane lamination) and microbial oxidation (**B**). The metal-rich fluid slightly enlarged the primary pores of the marlstone and the fossils, and the dolomite shows Mn-rich crust	
	A **Evidence** $\delta^{18}O_{SMOW}$: 23.41‰ – 9.93‰; main element content (Fe, Mn Si, Ba, K etc.), akaganeite; hollandite, ramsdellite, manganite, Fe-rich clay minerals; Mn-rich carbonates (dolomite and calcite); diffuse borders	**B** **Evidence** $\delta^{13}C_{PDB}$: -21.35‰ - -1.05‰; Fe-Mn-oxyhydroxides, XRD amorphous Mn oxides, filamentous microtexture; the high organic matter content of the laminae, stromatolite-like structure
Early diagenesis	**Genesis of limemarlstone via degradation of organic matter** Calcification by the degradation of the organic matter (cellular, EPS, etc.). The calcite transforms to dolomite and/or aragonite	
	Evidence Enrichment of clay minerals and euhedral dolomite, boring traces on clay minerals	
Footwall	**Sedimentation in a subtropical environment** Normal salinity, neutral pH (6-8), aerobic (DO>2 ml/l), redox (Eh: +0.4 V- +1.0 V), high bioproductivity (macro and microfossils, clay minerals, calcite)	
	Evidence $\delta^{18}O_{SMOW}$: 27.48 ‰ – 29.87 ‰; clay minerals; microtextures, biodebris (*Echinozoa*, *Foraminifera*, fish remains); low detrital mineral (quartz) content, K-feldspar with luminescence (ash)	

SUPPORTING INFORMATION

Fe-Mn oxide indications in the feeder and mound zone of the Jurassic Mn-carbonate ore deposit, Úrkút, Hungary

Zsombor Molnár[1], Márta Polgári[2,3*], James R. Hein[4], Sándor Józsa[1], József Fekete[2], Ildikó Gyollai[2], Krisztián Fintor[5], Lóránt Bíró[2], Máté Szabó[2], Sándor Rapi[6], Péter Forgó[7], Tamás Vigh[8]

[1]*Eötvös University, Dept. Petrology and Geochemistry, 1117 Budapest, Pázmány P. s. 1/c, Hungary, e-mail: molnarzs1994@gmail.com*
[2]*Research Center for Astronomy and Geosciences, Geobiomineralization and Astrobiological Research Group, Institute for Geology and Geochemistry, Hungarian Academy of Sciences, 1112 Budapest, Budaörsi út. 45, Hungary, e-mail: rodokrozit@gmail.com*
[3]*Eszterházy Károly University, Dept. of Natural Geography and Geoinformatics, 3300 Eger, Leányka str. 6/C, Hungary*
[4]*USGS, 2885 Mission St., Santa Cruz, CA 95060, U.S.A., jhein@usgs.gov*
[5]*Szeged University, Dept. of Mineralogy, Geochemistry and Petrology, 6722 Szeged, Egyetem, str. 2-6, Hungary, e-mail: efkrisz@gmail.com*
[6]*Eszterházy Károly University, Regional Research Centre, 3300 Eger, Leányka str. 6/G, Hungary, e-mail: raps@ektf.hu*
[7]*Eszterházy Károly University, Food Science Institute, 3300 Eger, Leányka Str. 6, Hungary, e-mail: forgop@ektf.hu*
[8]*Mangán Ltd, Úrkút, Külterület 1. 8409 Hungary, e-mail: manganvigh@gmail.com*

**corresponding authors:*
rodokrozit@gmail.com


Contact zone between the footwall limemarlstone and the black shale-hosted Mn-carbonate deposit
a
2007/01/13


Mangán Kft., Úrkút
CH 07011333 in situ
(2/3)
b
2007/01/13


c
2007/01/13

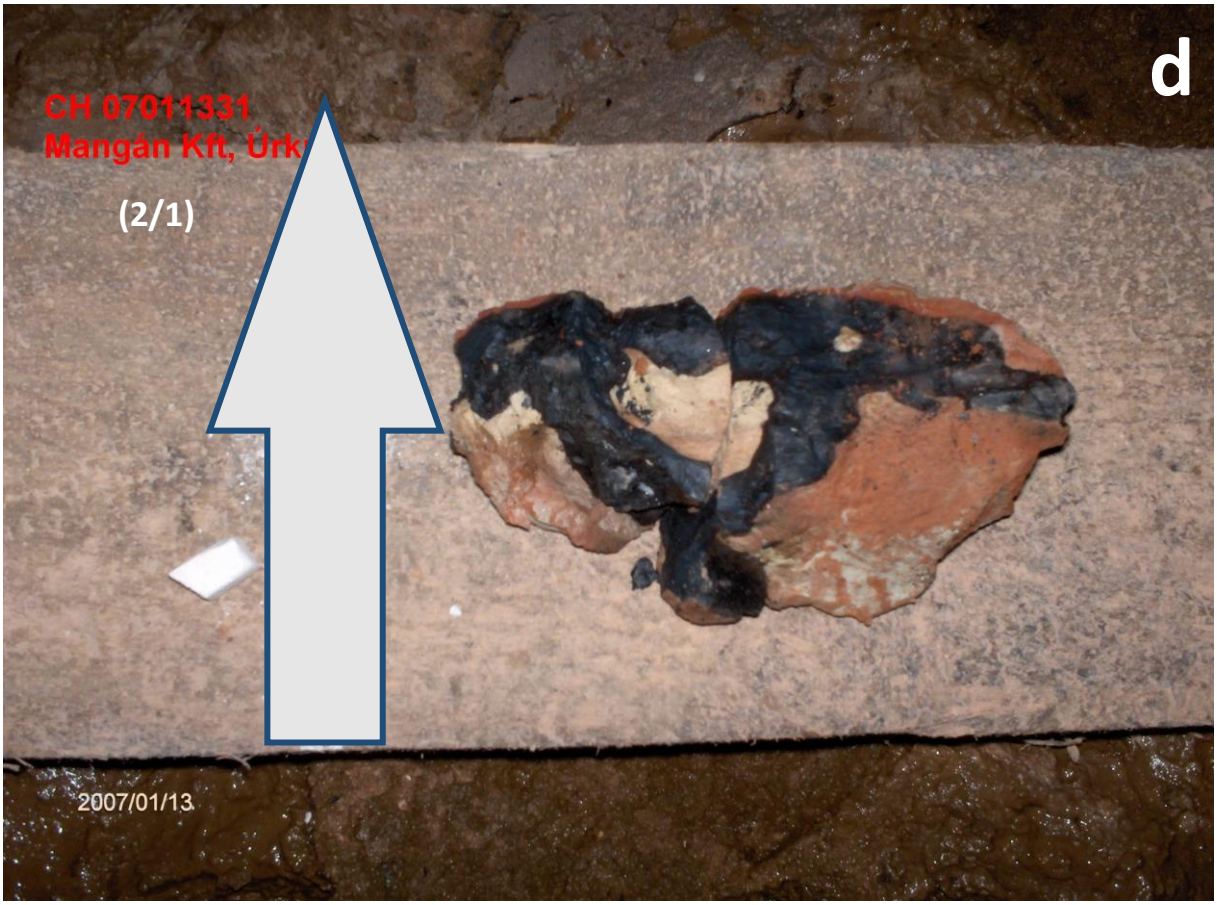
d
CH 07011331
Mangán Kft, Úrk
(2/1)
2007/01/13


e
2007/01/13
CH 07011331, 32
in situ
Mangán Kft., Úrkút
2/2
32
2/1
31


f
2007/01/13

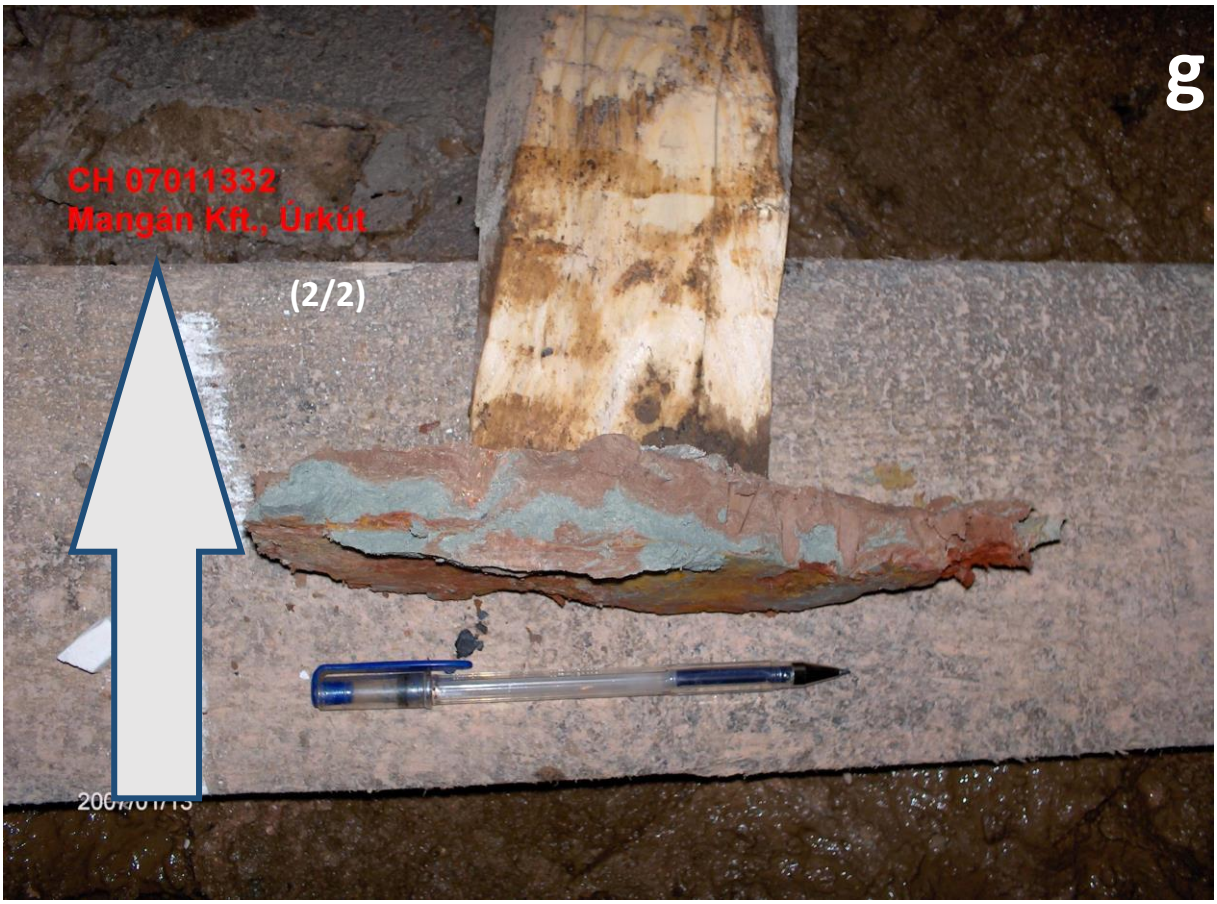
g
CH 07011332
Mangán Kft., Úrkút
(2/2)

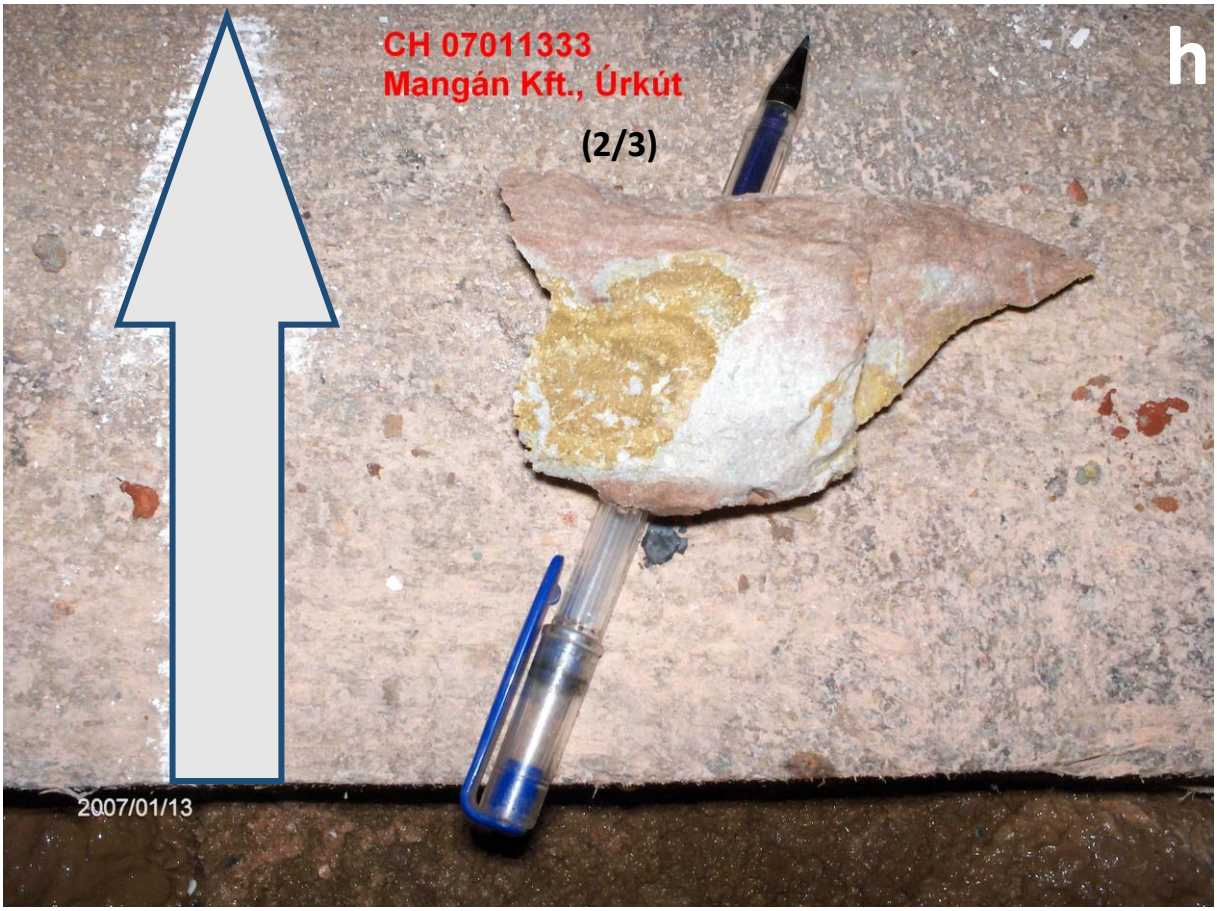
h
CH 07011333
Mangán Kft., Úrkút
(2/3)
2007/01/13

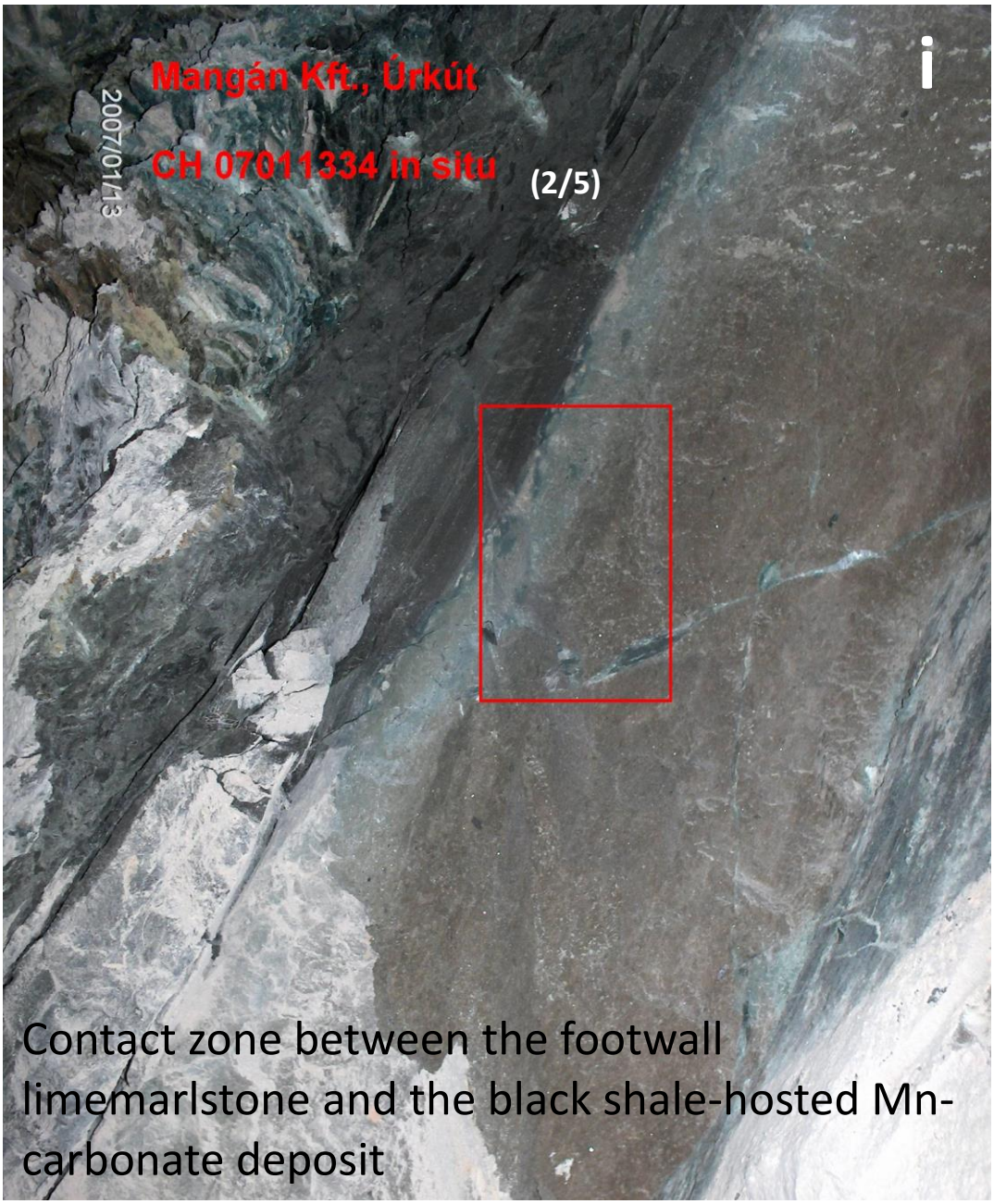

Contact zone between the footwall limemarlstone and the black shale-hosted Mn-carbonate deposit

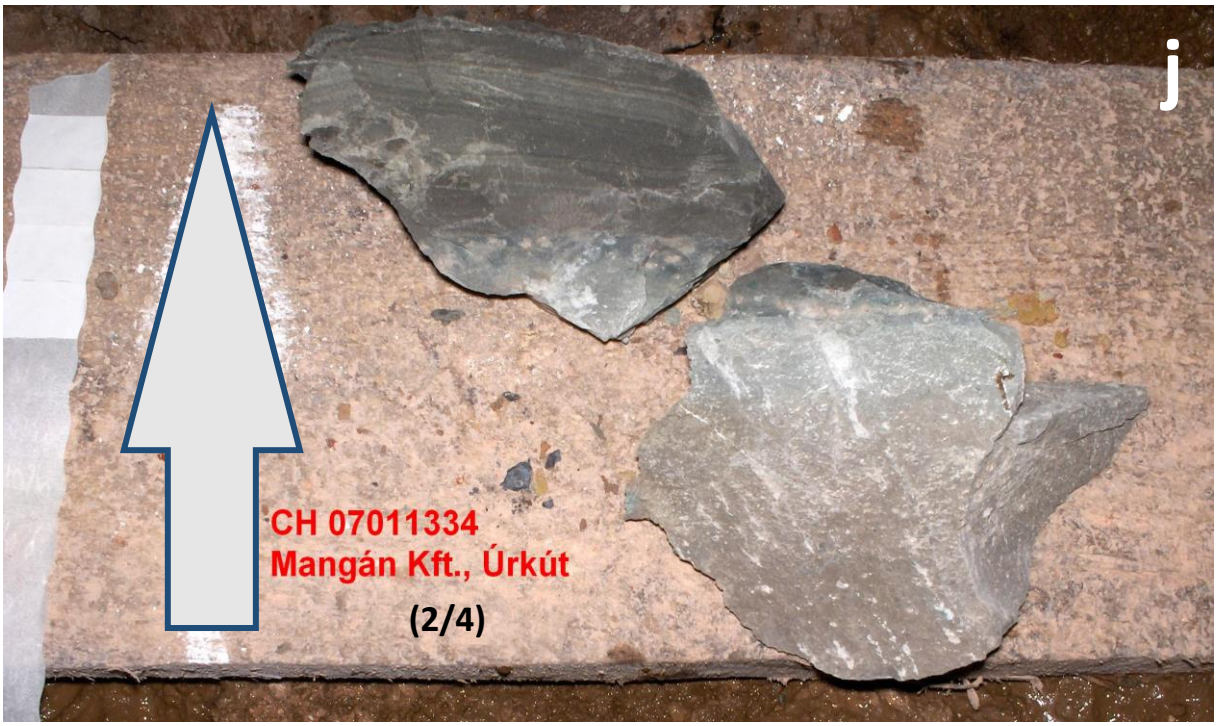
j
CH 07011334
Mangán Kft., Úrkút
(2/4)


K
2007/01/13

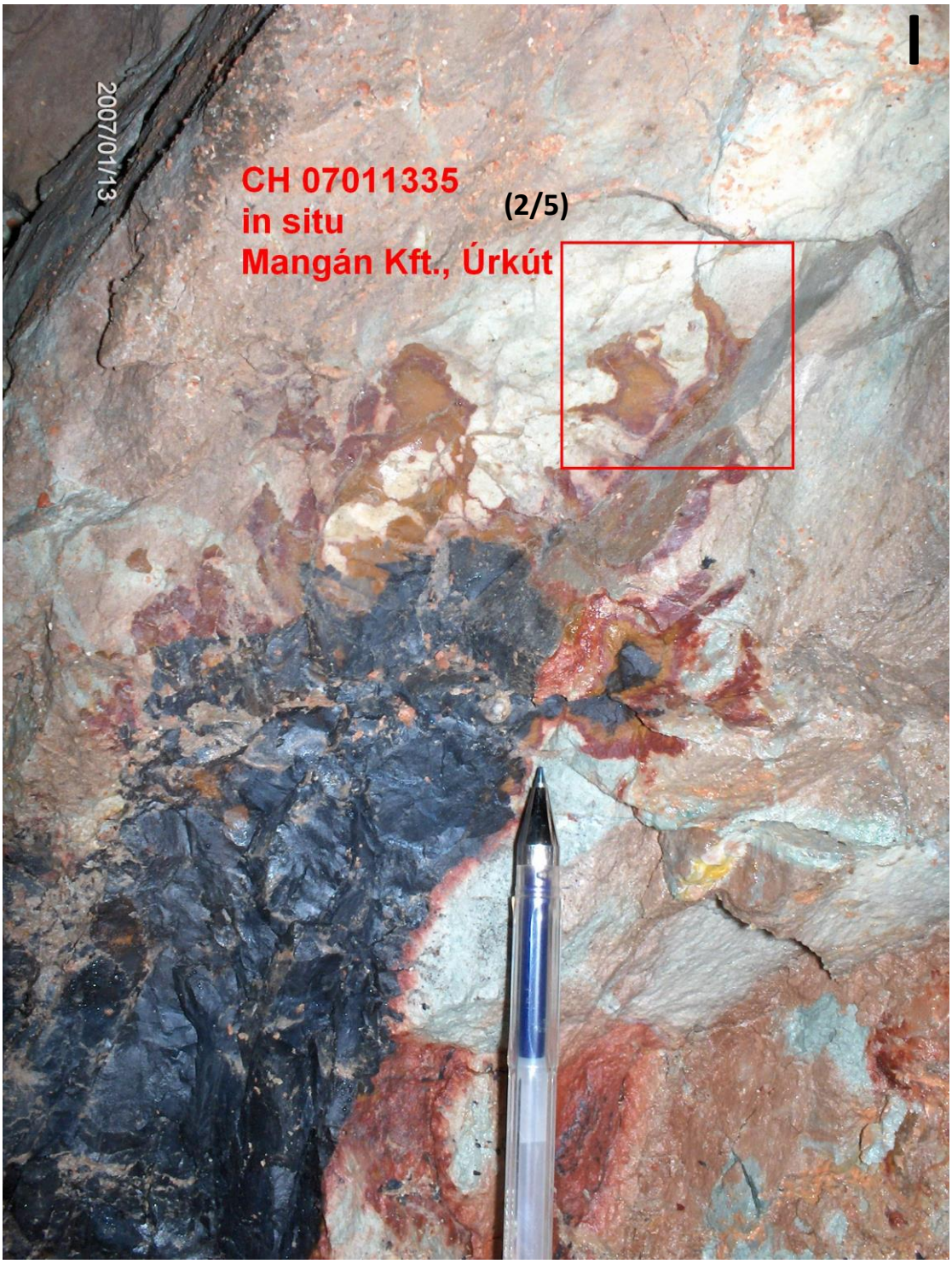
2007/01/13
CH 07011335
in situ
Mangán Kft., Úrkút
(2/5)

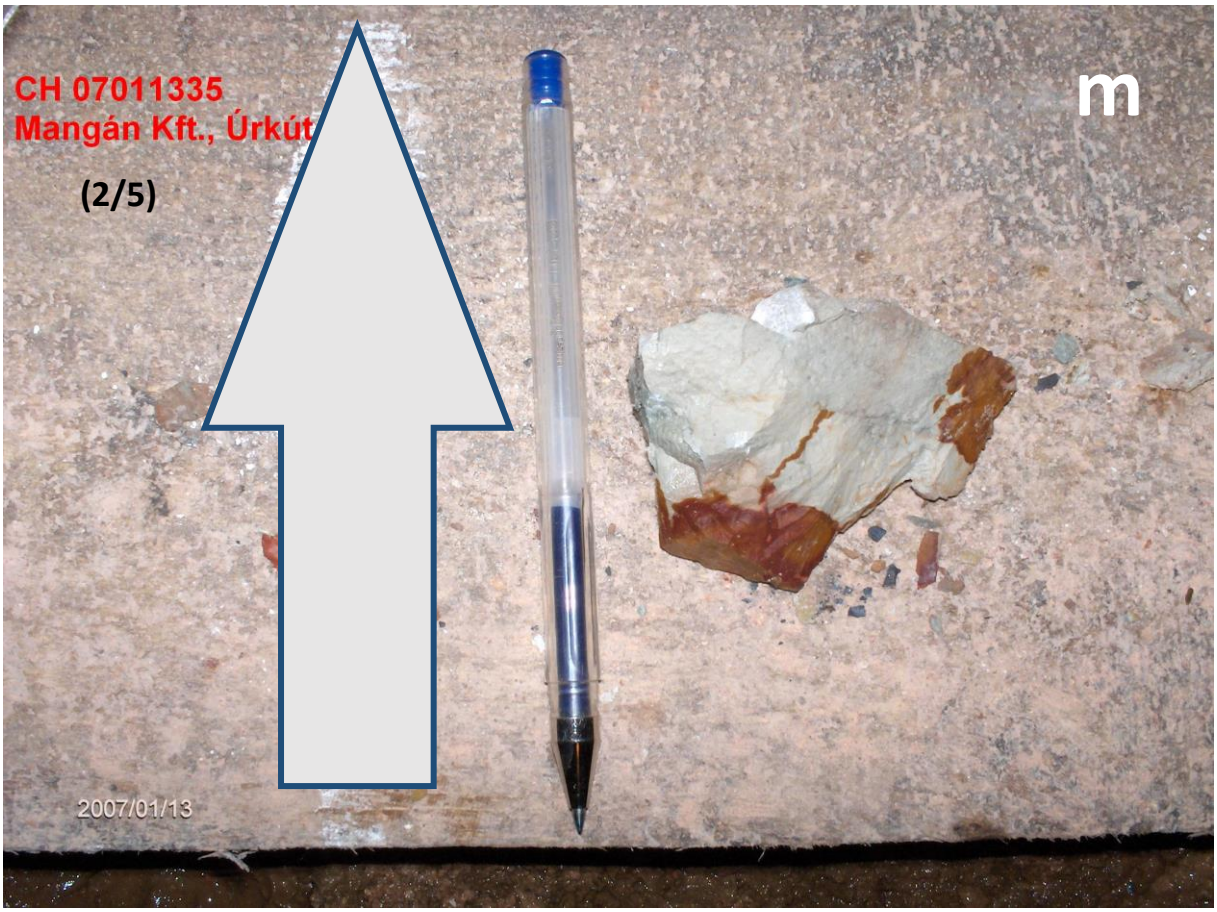
CH 07011335
Mangán Kft., Úrkút
(2/5)
m
2007/01/13

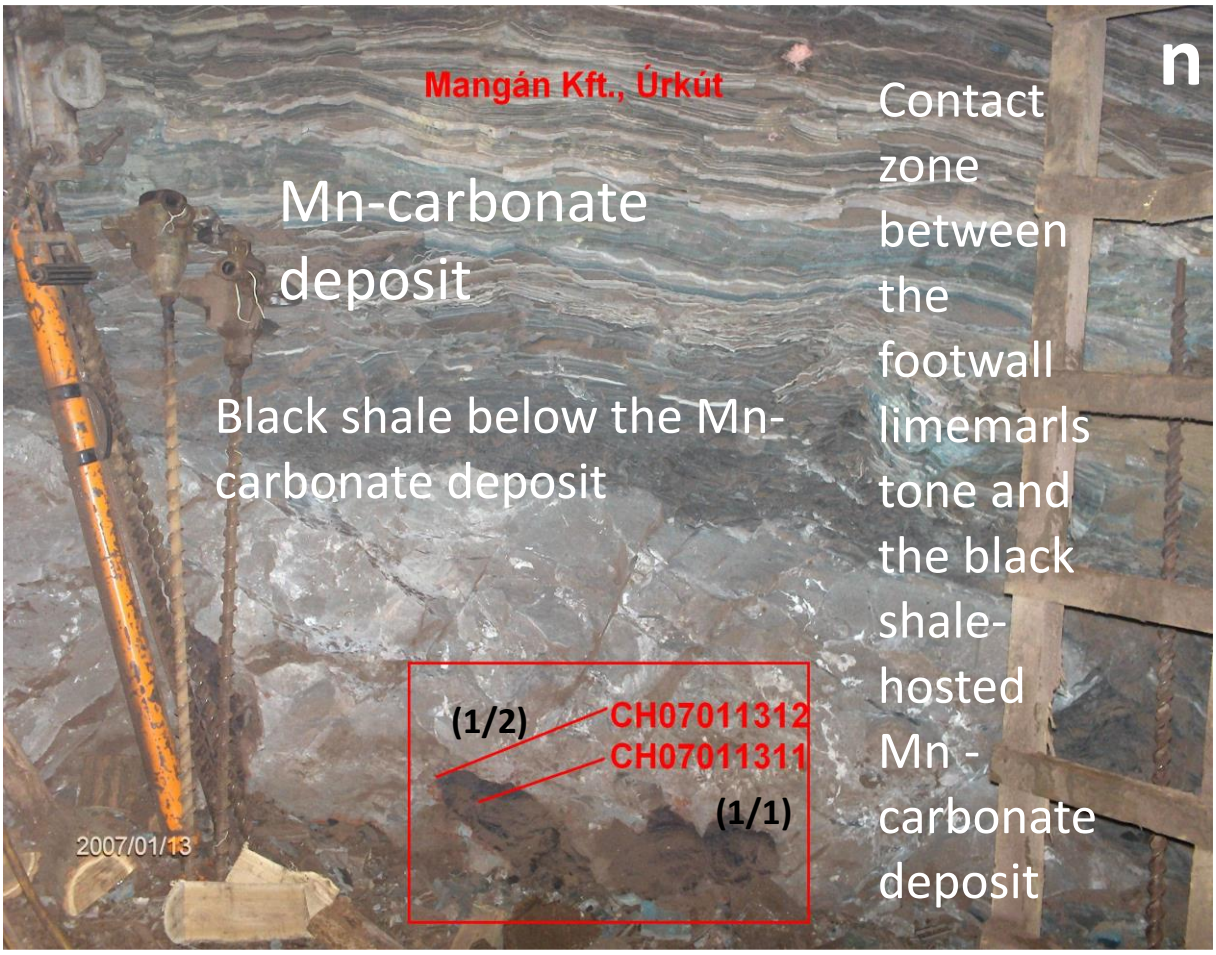
Mangán Kft., Úrkút
Mn-carbonate deposit
Black shale below the Mn-carbonate deposit
Contact zone between the footwall limemarlstone and the black shale-hosted Mn - carbonate deposit
(1/2)
CH07011312
CH07011311
(1/1)
2007/01/13

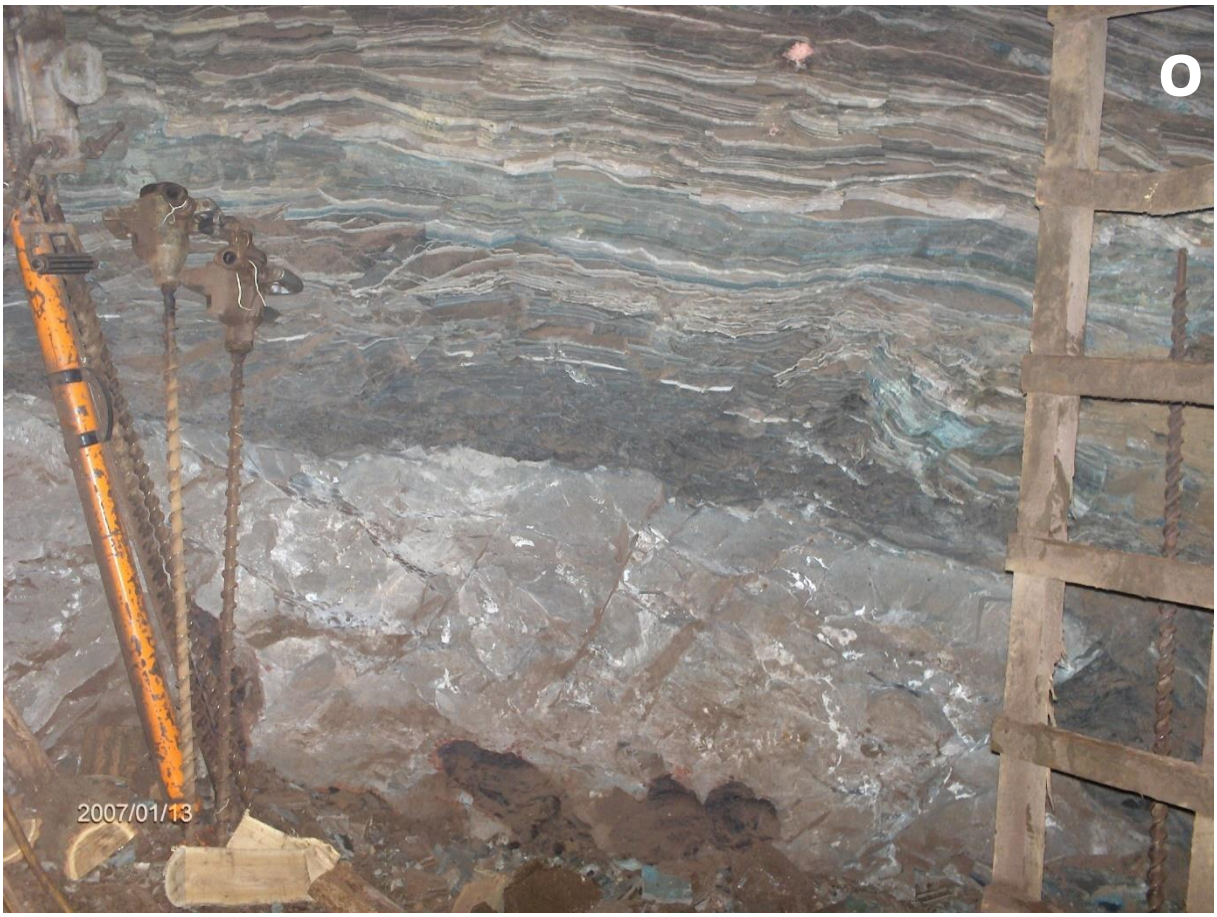
O
2007/01/13

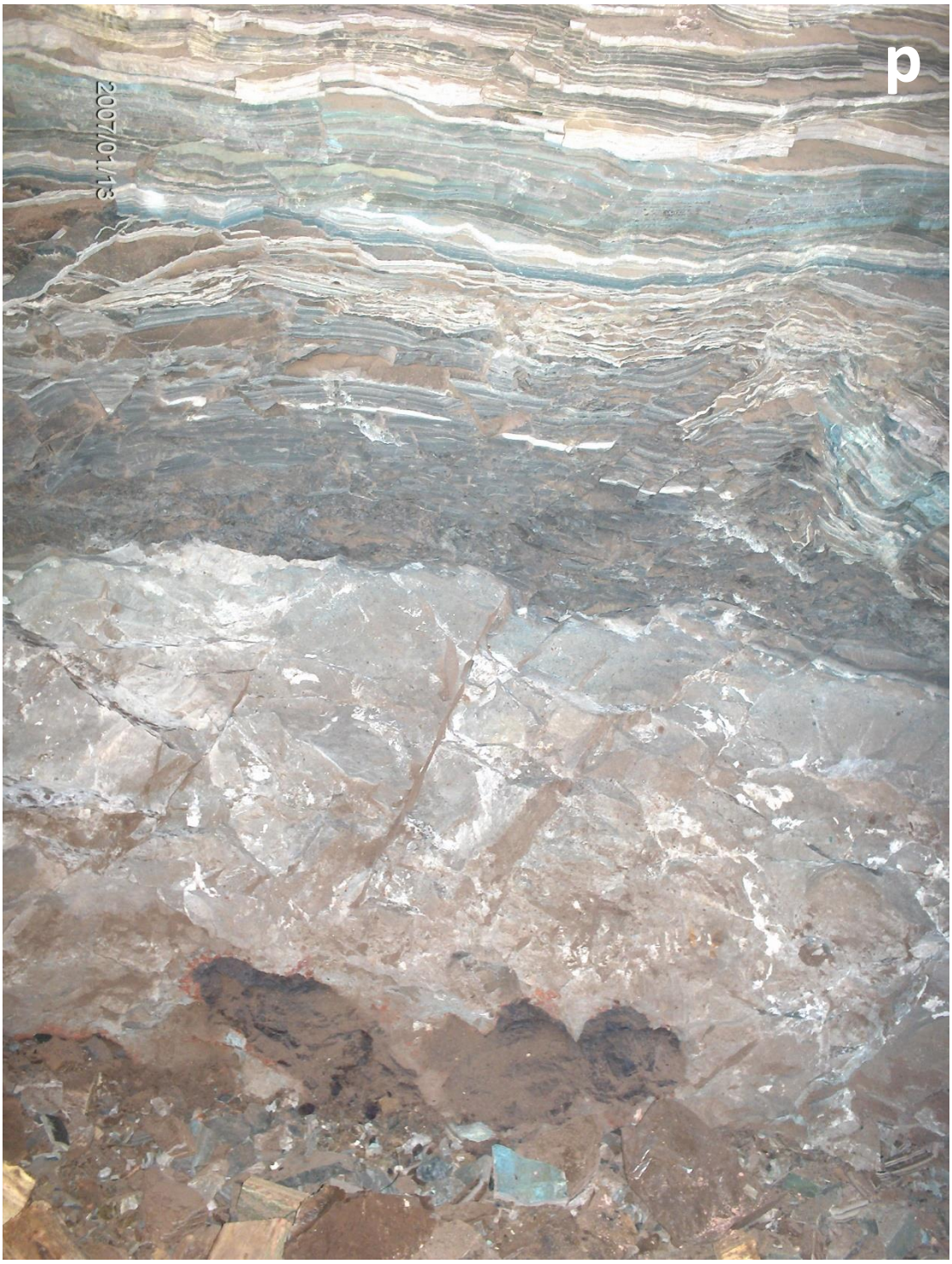

SI. 1. (a) The contact (feeder and mound) zone between the footwall limemarlstone and the black shale-hosted Mn-carbonate deposit, (b) the area of section 2 (sample 2/3), (c) Fe-Mn-oxide indication in vein-like structure, (d) the 2/1 sample for details see Table 1 (archive ID with red), (e) outcrop photo of samples 2/1 (archive ID with red, 31), a Mn oxide and 2/2 (archive ID with red, 32), marlstone, (f) The contact (feeder and mound) zone between the footwall limemarlstone and the black shale hosted Mn-carbonate deposit, (g) (h) samples 2/2 and 2/3 with arrow showing up direction (marlstones, archive ID with red) (i) The contact of the limemarlstone footwall and the black shale, (j) the black shale samples (2/4) with the up

direction arrow (archive ID with red), (k) Fe-Mn-oxide indication with Fe-rich crust in the limemarlstone, (l) the Fe-rich 2/5 marlstone sample in limemarlstone, the box shows the sample location (m) outcrop photo of sample 2/5 Fe-rich limemarlstone sample with up direction indicated, (n) (o) (p) the whole exposed section in the area, showing laminated Mn-carbonate ore and section 1 with samples 1/1 and 1/2 on (n) (archive ID with red).

SI. 2. Applied methods on samples

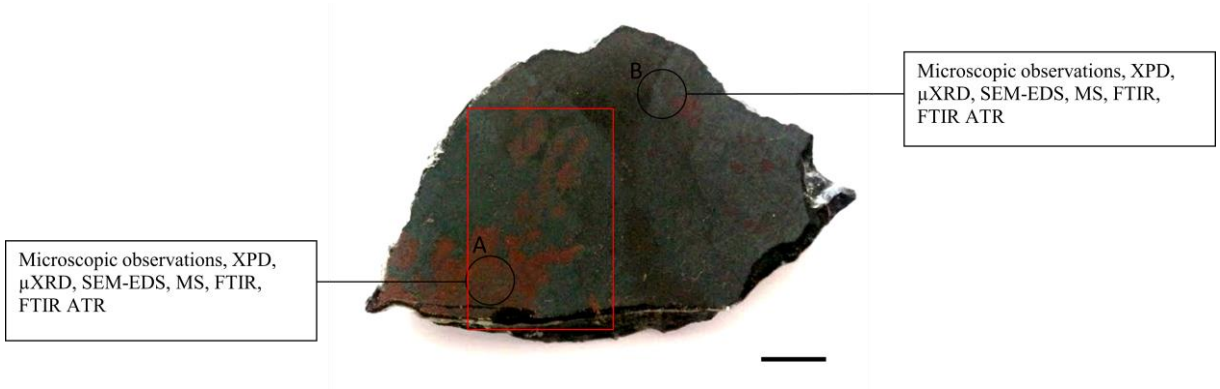

Applied methods on **sample 1/1**, scale: 1 cm (sample 1/1; polished surface). Legend: A – 1/1/D sample; B – 1/1/C sample; red square: thin section. Abbreviations: XPD – X-ray powder diffractometry, µXRD – micro-X-ray diffractometry, MS – mass spectroscopy, SEM-EDS – scanning electronmicorscopy, FTIR - Fourier transform infrared spectroscopy, FTIR ATR – Attenuated total reflectance Fourier transform infrared spectroscopy

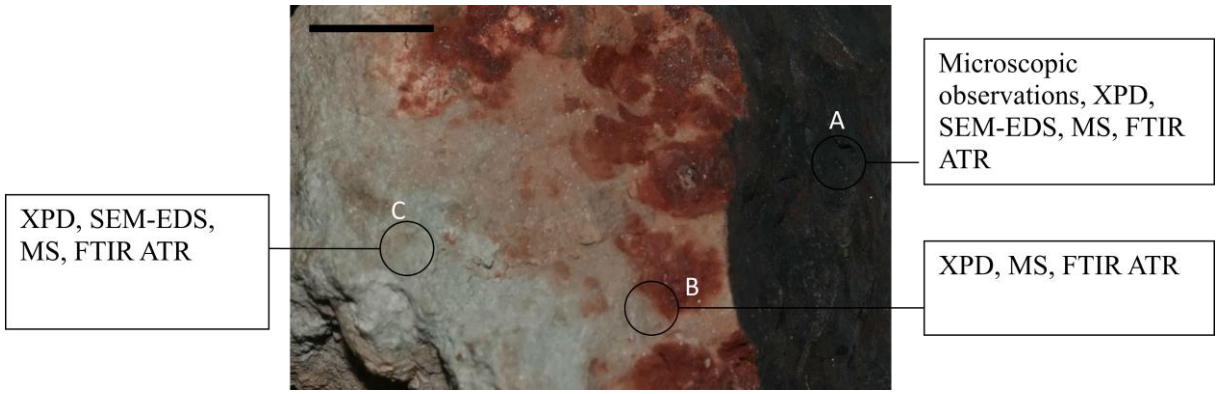

Applied methods on **sample 1/2**; scale: 1 cm (sample 1/2; original surface). Legend: A – 1/2/A sample; B – 1/2/B sample; C – 1/2/C sample. Abbreviations: XPD – X-ray powder diffractometry, µXRD – micro-X-ray diffractometry, MS – mass spectroscopy, SEM-EDS – scanning electronmicorscopy, FTIR ATR – Attenuated total reflectance Fourier transform infrared spectroscopy

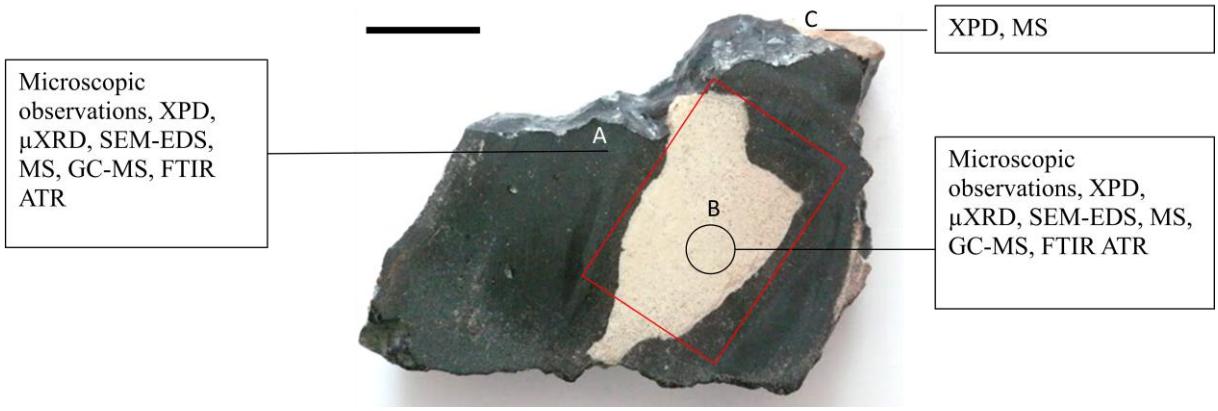

Applied methods on **sample 2/1**, scale: 1 cm (sample 2/1; polished surface). Legend: A – 2/1/A sample; B – 2/1/B sample; C – 2/1/C sample; red square: thin section. Abbreviations: XPD – X-ray powder diffractometry, µXRD – micro-X-ray diffractometry, MS – mass spectroscopy, SEM-EDS – scanning electronmicorscopy, GC-MS – Gas chromatography mass spectroscopy, FTIR ATR – Attenuated total reflectance Fourier transform infrared spectroscopy

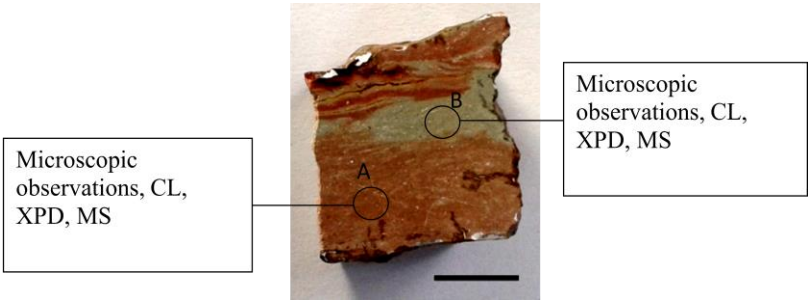

Applied methods on **sample 2/2**, scale: 1 cm (sample 2/2; polished surface). Legend: A – 2/2/A sample; B – 2/2/B sample. Abbreviations: XPD – X-ray powder diffractometry, CL – cathodeluminescence microscope, MS – mass spectroscopy,

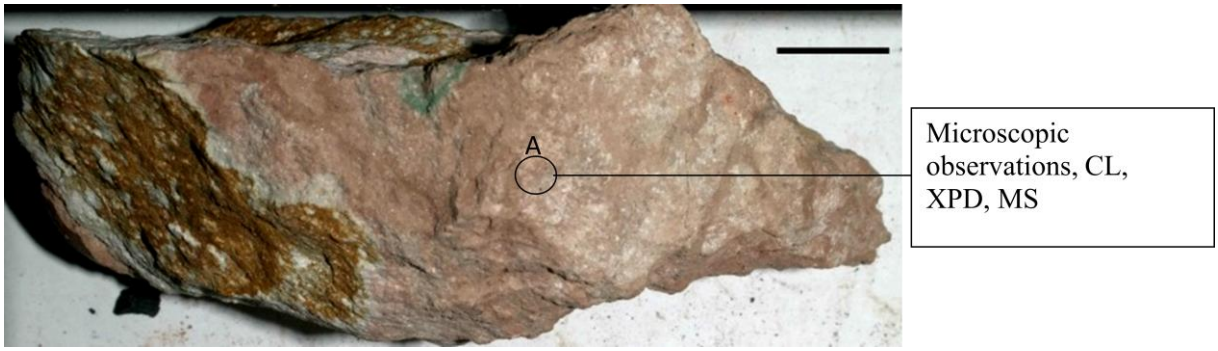

Applied methods on **sample 2/3**, scale: 5 cm (sample 2/3; whole rock). Legend: A – 2/3/A sample. Abbreviations: XPD – CL – cathodeluminescence microscope, X-ray powder diffractometry, MS – mass spectroscopy,

Applied methods on **sample 2/4/A**, scale: 1 cm (**sample 2/4**; polished surface). Abbreviations: CL – Cathode luminescence microscope, XPD – X-ray powder diffractometry, CL – Cathode luminescence microscope, MS – mass spectroscopy, GC-MS – Gas chromatography mass spectroscopy, FTIR ATR – Attenuated total reflectance Fourier transform infrared spectroscopy

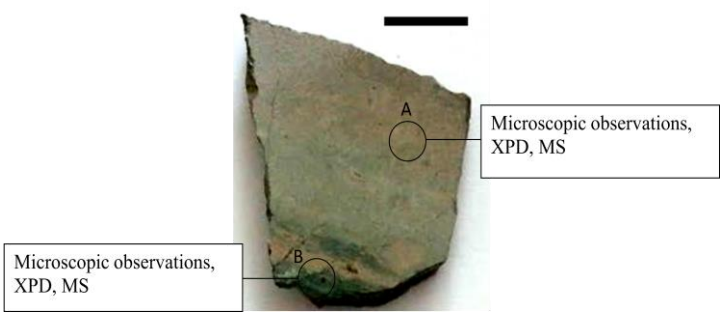

Applied methods on **sample 2/4/D**, scale: 1 cm (sample 2/4; polished surface). Abbreviations: XPD – X-ray powder diffractometry, MS – mass spectroscopy,

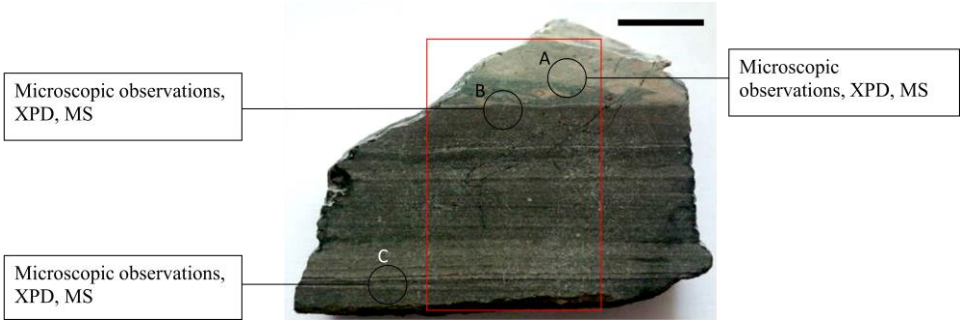

Applied methods on **sample 2/4/F**, scale: 1 cm (**sample 2/4**; polished surface). Abbreviations: XPD – X-ray powder diffractometry, MS – mass spectroscopy,

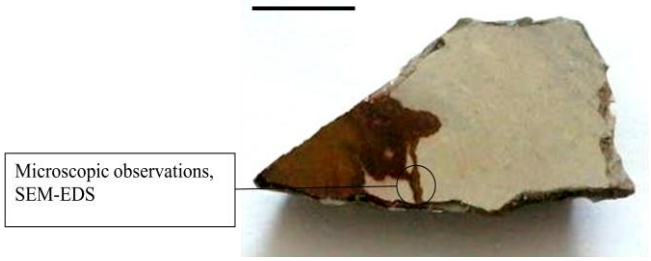

Applied methods on **sample 2/5**, scale: 1 cm (**sample 2/5**; polished surface). Abbreviations: SEM-EDS – scanning electronmicorscopy

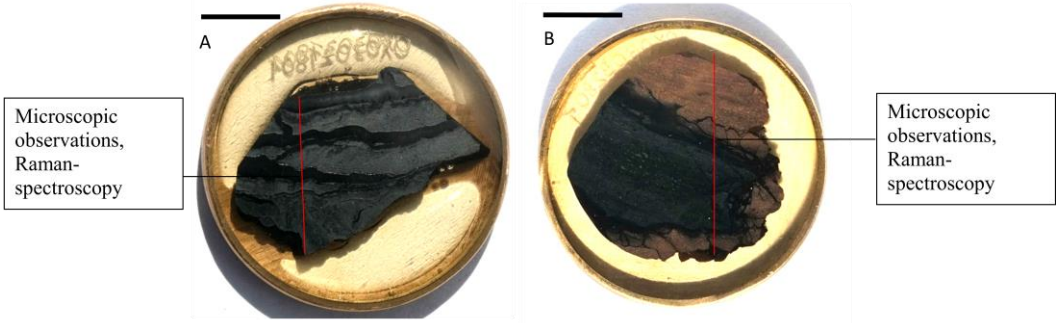

Applied methods on section 3, scale: 1 cm (polished surface). Legend: A – **sample 3/1/A**; B – **sample 3/1/B**

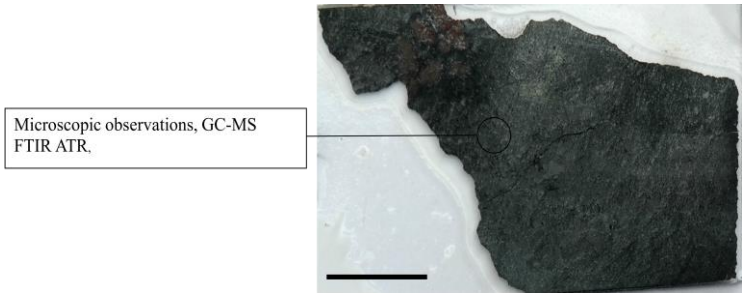

Applied methods on **sample 4/1/A**, scale: 1 cm (**sample 4/1/A**; thin section). Abbreviations: GC-MS – Gas chromatography mass spectroscopy, FTIR ATR – Attenuated total reflectance Fourier transform infrared spectroscopy

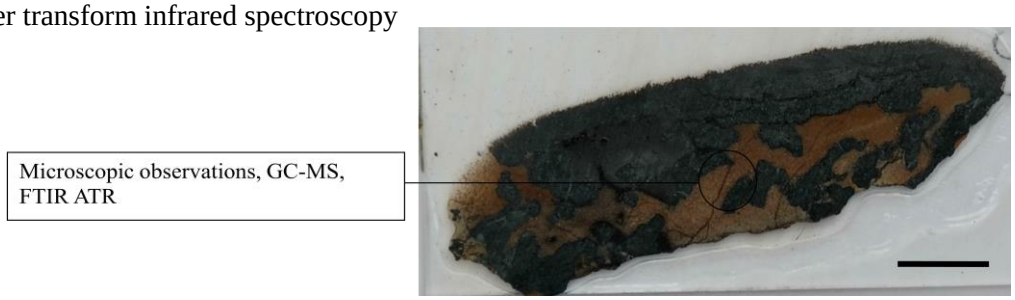

Applied methods on **sample 4/1/B**, scale: 1 cm (**sample 4/1/B**; thin section). Abbreviations: GC-MS – Gas chromatography mass spectroscopy, FTIR ATR – Attenuated total reflectance Fourier transform infrared spectroscopy

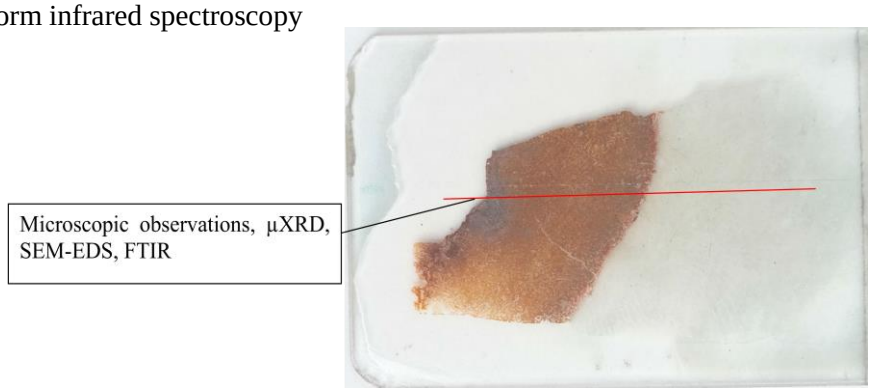

Applied methods on **sample 4/1/C**, scale: 1 cm (**sample 4/1/C**; thin section). Abbreviations: µXRD – micro-X-ray diffractometry, SEM-EDS – scanning electronmicorscopy; red line: SEM-EDS profile analyses

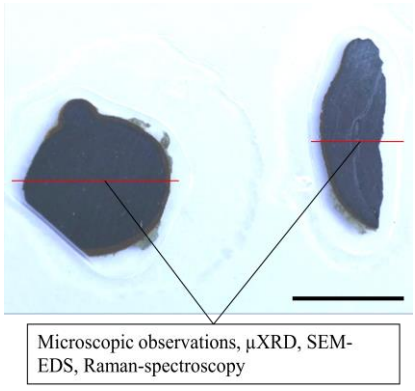

Applied methods on **sample 4/1/D**, scale: 1 cm (**sample 4/1/D**; thin section). Abbreviations: µXRD – micro-X-ray diffractometry, SEM-EDS – scanning electronmicorscopy; red line: SEM-EDS profile analyses

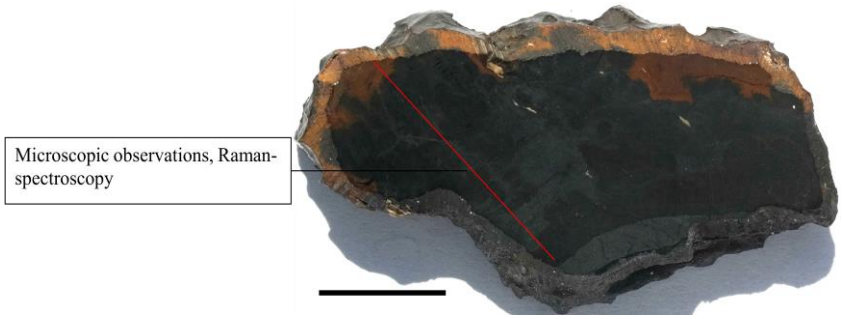

Applied methods on **sample 5/1/A**, scale: 1 cm (**sample 5/1/A**; polished surface). Red line: Raman profile analyses

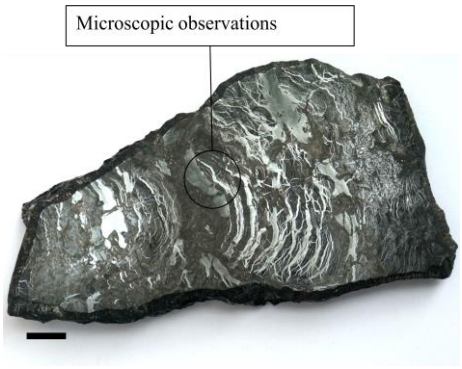

Applied methods on **sample 5/1/B**, scale: 1 cm (**sample 5/1/B**; polished surface).

Applied methods on **sample 5/1/C**, scale: 1 cm (**sample 5/1/C**; polished surface).

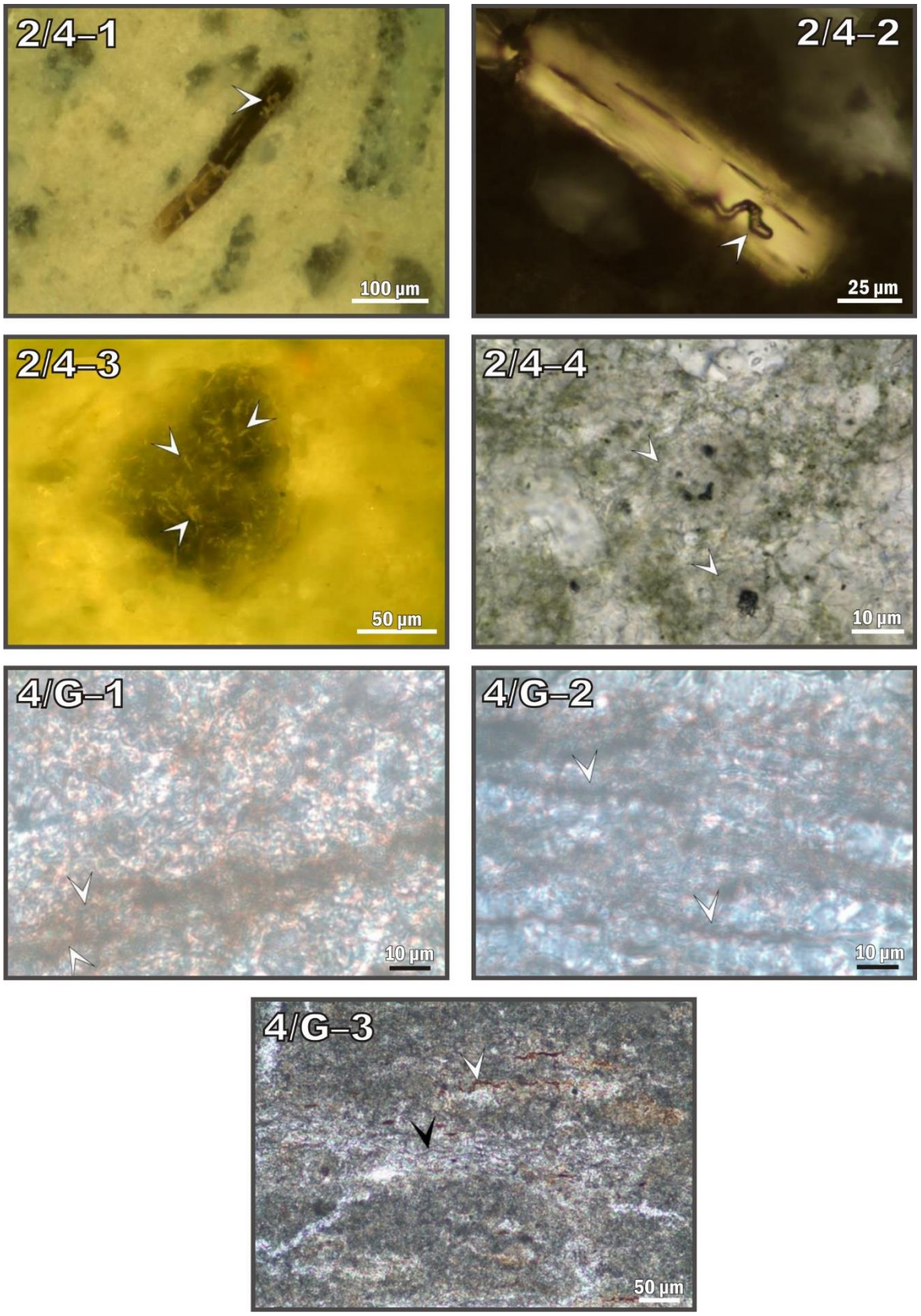
2/4–1
100 µm
2/4–2
25 µm
2/4–3
50 µm
2/4–4
10 µm
4/G–1
10 µm
4/G–2
10 µm
4/G–3
50 µm

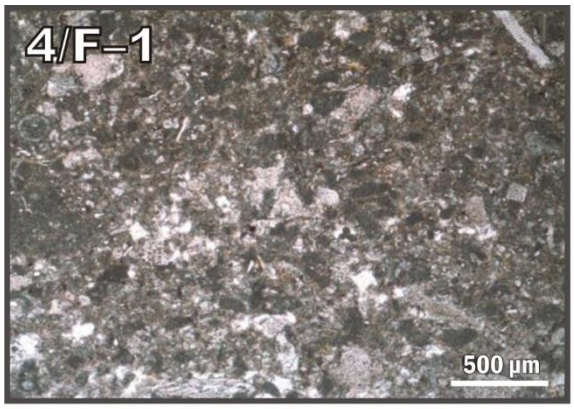
4/F–1
500 µm

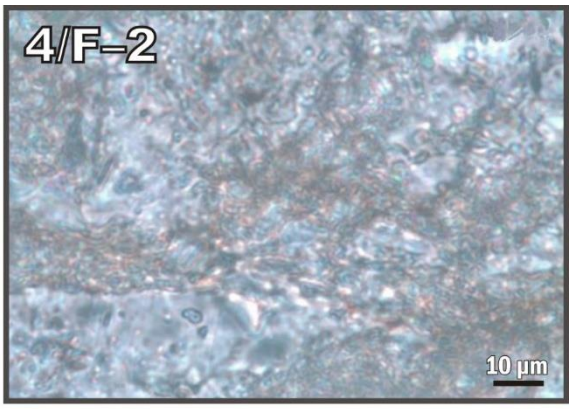
4/F–2
10 µm

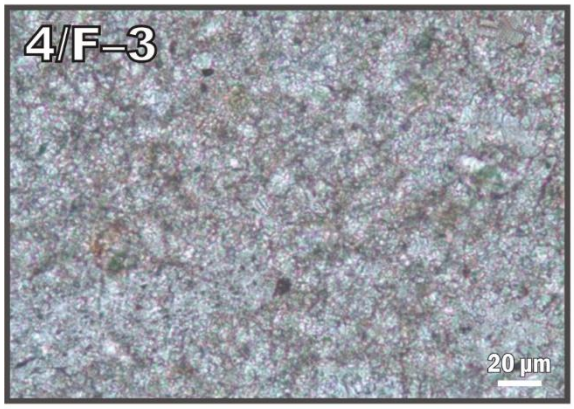
4/F–3
20 µm

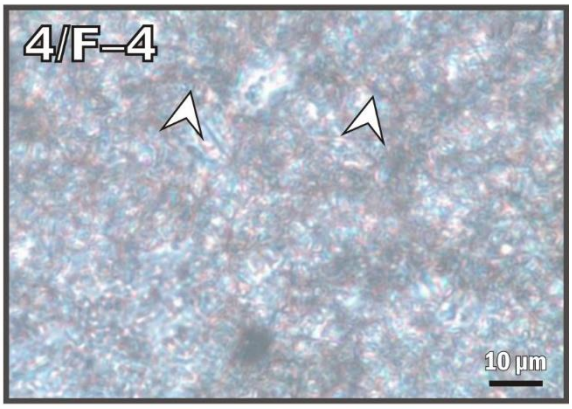
4/F–4
10 µm

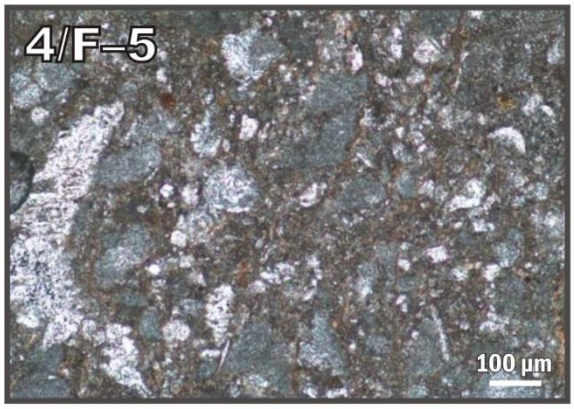
4/F–5
100 µm

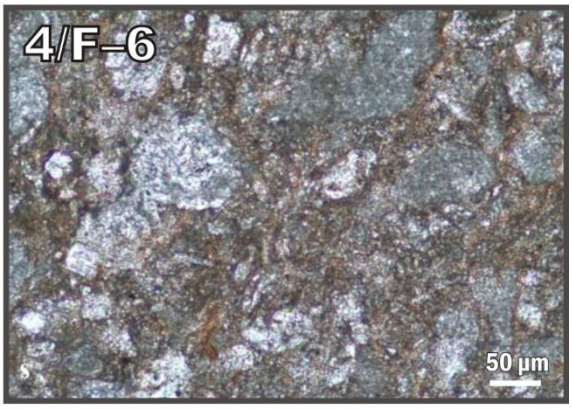
4/F–6
50 µm

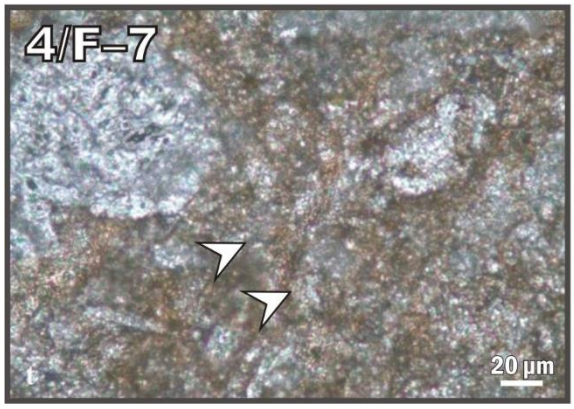
4/F–7
20 µm

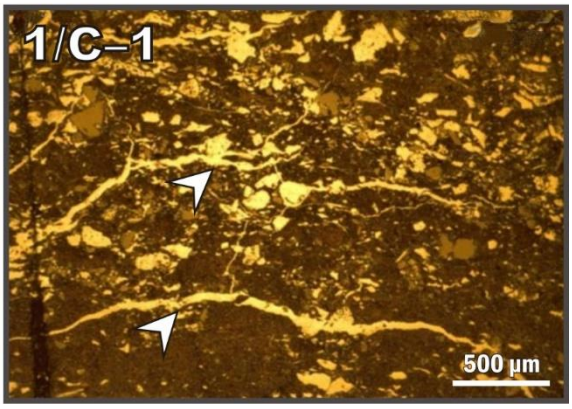
1/C–1
500 µm

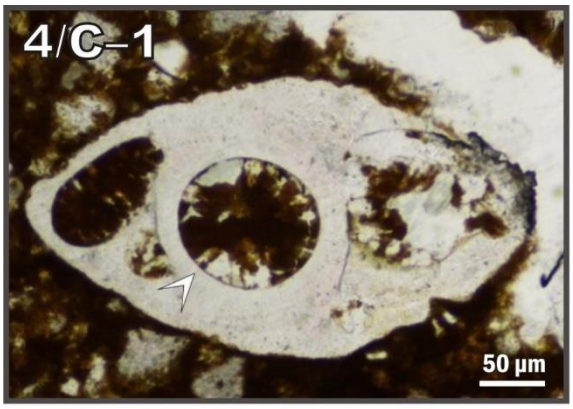
4/C–1
50 µm

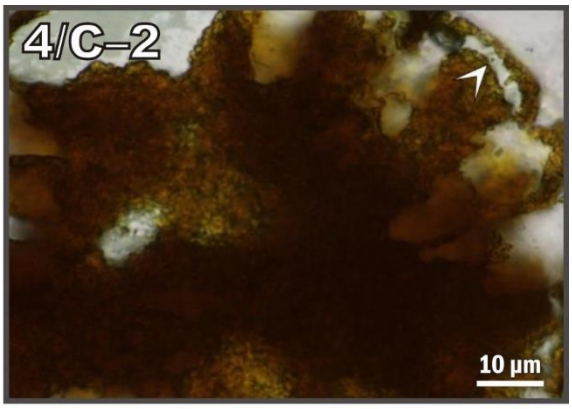
4/C–2
10 µm

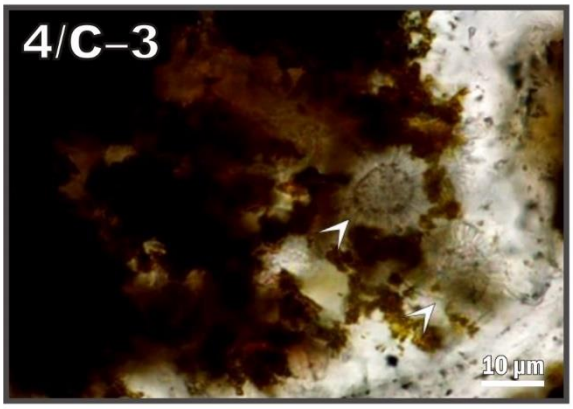
4/C–3
10 µm

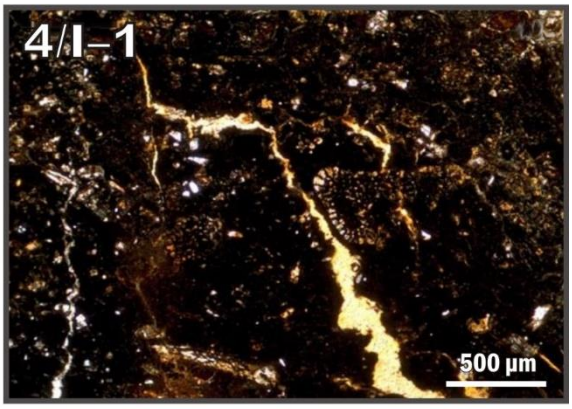
4/I–1
500 µm

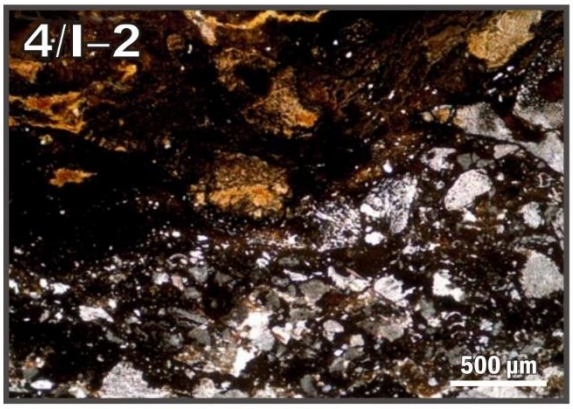
4/I–2
500 µm

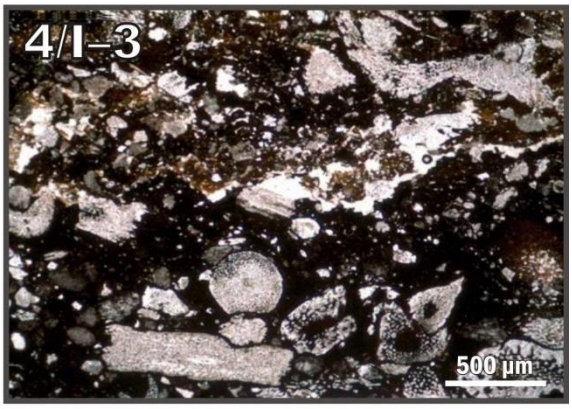
4/I–3
500 µm

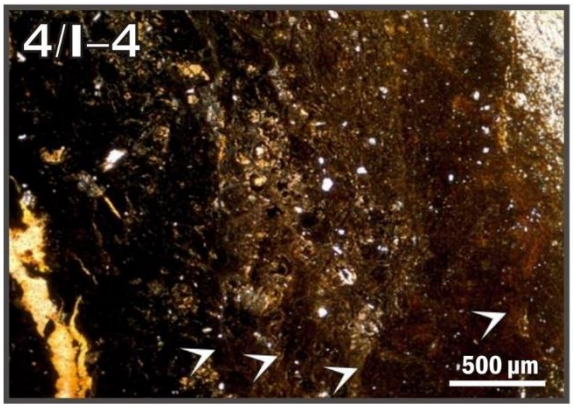
4/I–4
500 µm

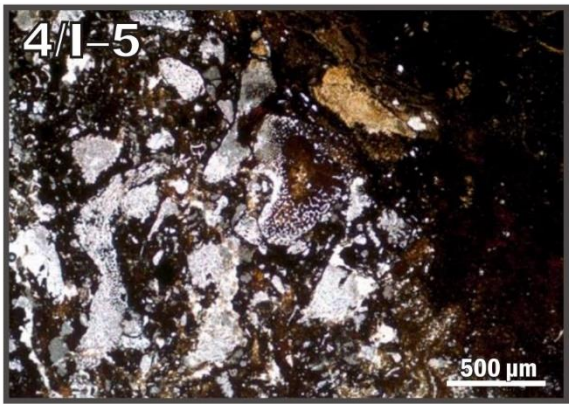
4/I–5
500 µm

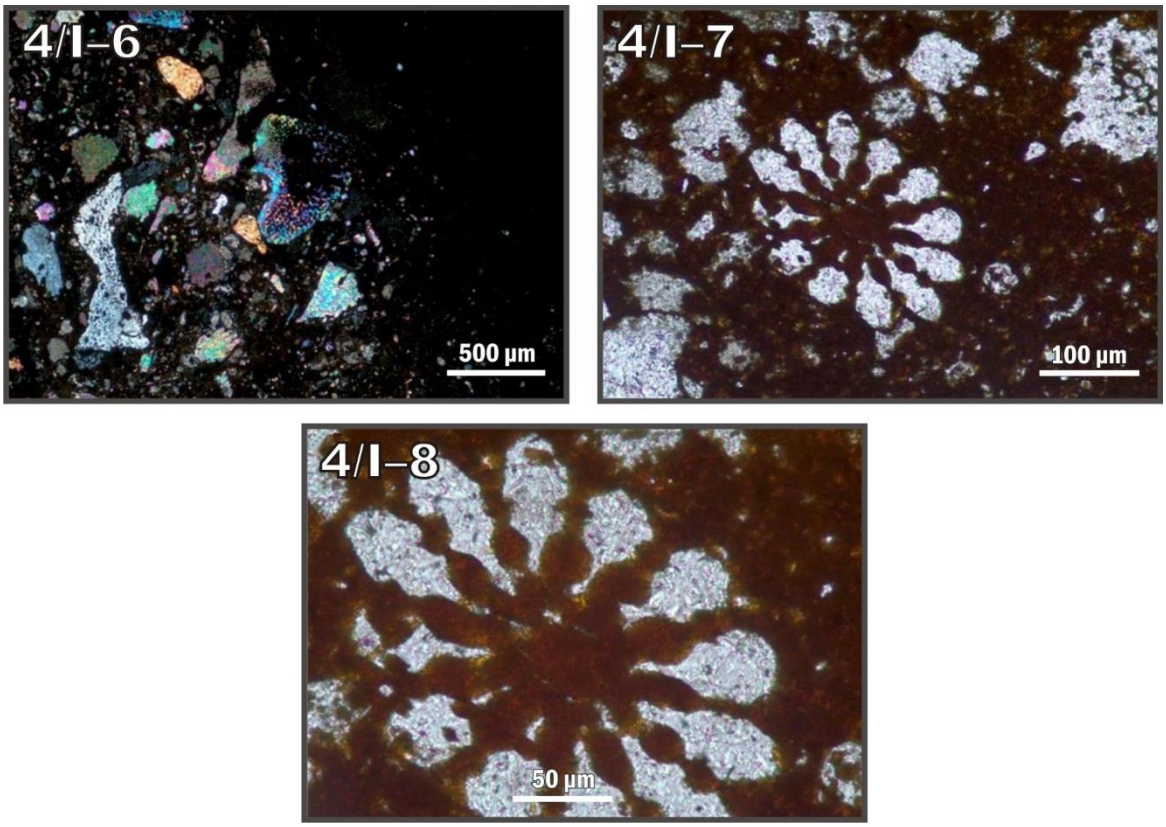

SI 3. Photos of the footwall limemarlstone and the proto-ore indications of the feeder zone, petrographic microscope, transmitted light (except where indicated) (**2/4-1; -2)** – Microscopic boring traces (arrows) on the same type of mineral debris (sample 2/4); **(2/4-3)** Microscopic photo of boring traces (arrows) on greenish clay mineral grain (sample 2/4); **(2/4-4)** Greenish clay mineral spots in the micritic marlstone footwall with rounded cyanobacterial perimorphs (arrows) (sample 2/4); (**4/G-1; -2**) filamentous microbial forms (arrows) with Fe-rich stalk in the micritic marlstone footwall (sample 4/G); **(4/G-3)** Calcite-rich filamentous bacterial forms (black arrow) with Fe-rich filamentous microbial forms (white arrows) (sample 4/G); **(4/F-1)** *Echinozoa* framework with quartz grains in the margin between the feeder zone and the footwall (sample 4/F); **(4/F-2; -4)** Filamentous Fe-rich microbial forms (sample 4/F); **(4/F-5;-6)** Micritic texture of the footwall limemarlstone (sample 4/F); **(4/F-7)** Filamentous Fe-rich microbial forms (sample 4/F); **(1/C-1)** Fe-rich indication with thin Mn-rich laminae (arrows) (sample 1/1**); (4/C-1; -2)** Fe-rich minerals in the pore space of *Foraminifera,* with higher magnification there are filamentous, microbial forms (arrows) (sample 4/C); **(4/C-3)** - Rounded cyanobacterial perimorphs with Fe-rich mineral on the marginal parts (sample 4/C); **(4/I-1)** Calcite-rich vein in the Mn-rich indication (sample 4/I); **(4/I-2; -3)** Biodebris in the Mn-rich indication, in the marginal parts of the footwall, the calcite framework is abundant, while in the deeper zones of the indication, the Fe and Mn content of the framework increase (sample 4/I); **(4/I-4)** Different zones of increasing Fe-content (sample 4/I); **(4/I-5)** Calcite framework of *Echinozoa* with increasing Fe-content of the pores (sample 4/I); **(4/I-6)** The same area of 4/I-5 with crossed Nicol (sample 4/I); **(4/I-7; -8)** Fe-rich pore filling of *Crinoidea*.

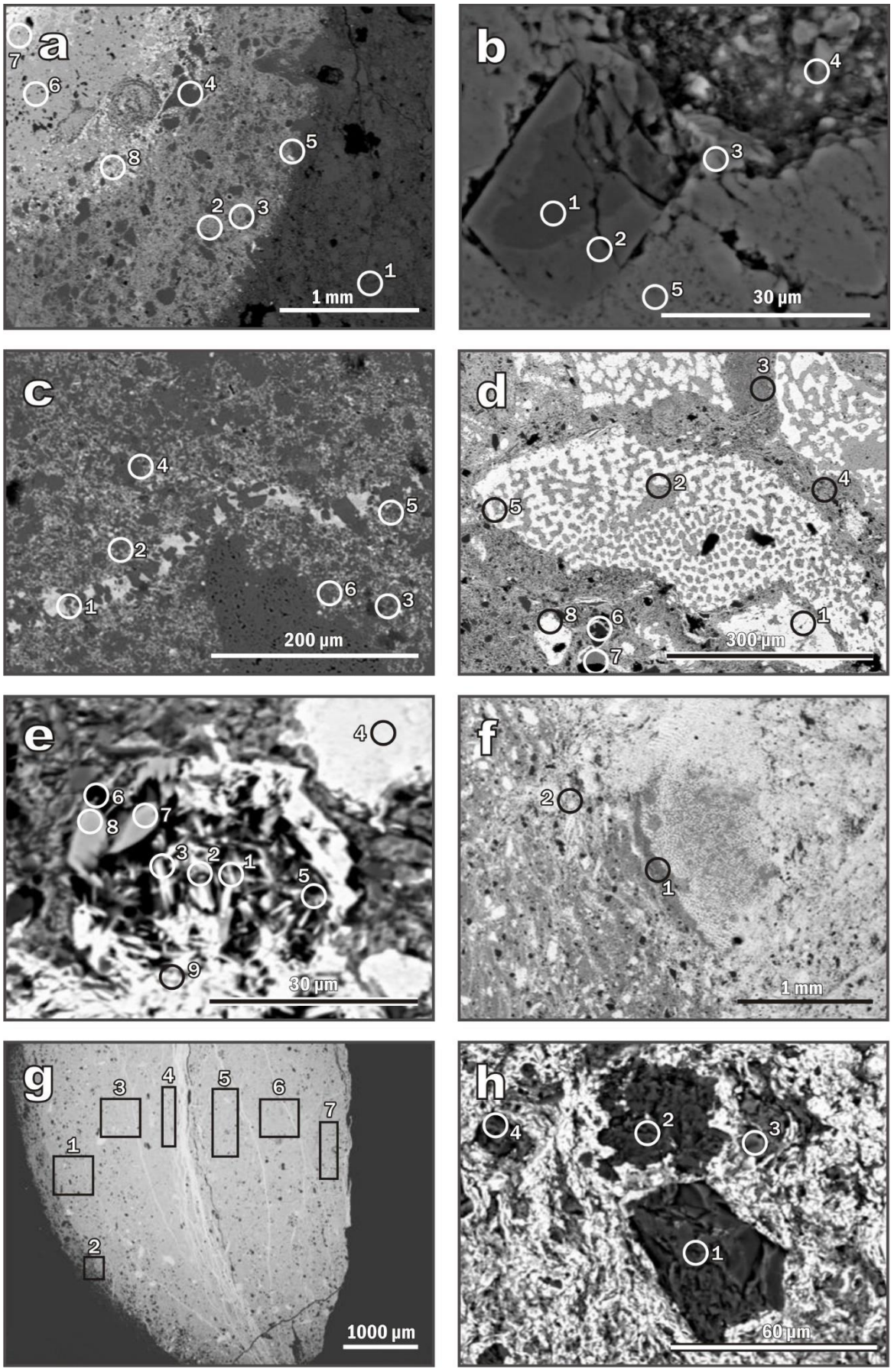
a
7
6
4
8
5
2
3
1
1 mm
b
4
3
1
2
5
30 µm
c
4
5
2
1
6
3
200 µm
d
3
2
4
5
8
6
1
7
300 µm
e
4
6
7
8
3
2
1
5
9
30 µm
f
2
1
1 mm
g
3
4
5
6
7
1
2
1000 µm
h
4
2
3
1
60 µm

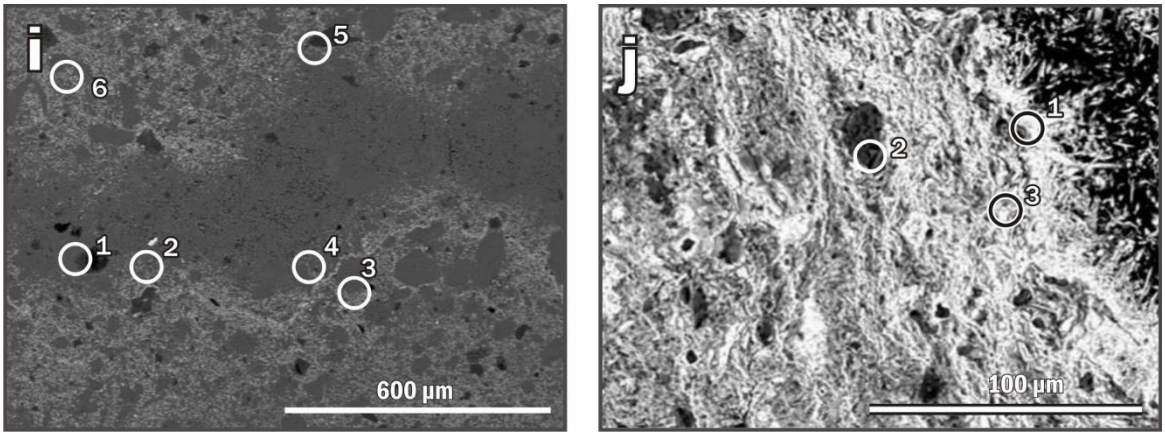

SI. 4. Back scattered electron images of the samples

(a) Zonation of different Mn-oxides with calcareous biodebris (black arrow) and the measured areas (white circle, for chemical content see table 1 below) (sample 2/1); **(b)** Euhedral dolomite with Mn-rich marginal parts and the measured areas (white circle, for chemical content see table 2 below) (sample 2/5); **(c)** Fe-rich veins in calcite matrix and the measured areas (white circle, for chemical content see table 3 below) (sample 2/5); **(d)** Mn-rich *Echinozoa* fragment and the measured areas (white circle, for chemical content see table 4 below) (sample 1/2); **(e)** Globular arrangement of Mn-oxide minerals with the measured areas (white circle, for chemical content see table 5 below) (sample 1/1); **(f)** Mn-rich biofragment with Mn-rich laminae and the measured areas (white circle, for chemical content see table 6 below) (sample 2/1); **(g)** Mn-rich ore indication with Fe-rich marginal part and the measured areas (white circle, for chemical content see table 7 below) (sample 4/4); **(h)** Dolomite and quartz grains in Mn-rich matrix and the measured areas (white circle, for chemical content see table 8 below) (sample 2/1); **(i)** Fe- and clay mineral rich veins in calcite matrix with euhedral dolomite and the measured areas (white circle, for chemical content see table 9 below) (sample 2/5); **(j)** Marginal part of the Mn-oxide mineral phases with typical, spike-like appearance with the measured areas (white circle, for chemical content see table 10 below) (sample 2/1)

Table 1. The main chemical components of the measured points at photo a (wt. %)										
Points	**Mg**	**Al**	**Si**	**K**	**Ca**	**Ti**	**Mn**	**Fe**	**Ba**	**O**
1	-	-	2.07	-	32.37	-		-	-	15.29
2	-	-	-	-	13.41	-	29.56	-	-	13.96
3	-	-	-	-	-	-	57.55	-	-	16.76
4	-	-	1.25	-	33.34	-	-	-	-	14.73
5	-	-	-	-	-	-	44.21	-	10.32	14.08
6	-	-	-	-	-	-	57.51	-	-	16.75
7	-	-	2.59	-	-	-	48.10	-	-	16.95
8	-	-	-	1.01	-	-	45.94	-	7.67	14.48

Table 2. The main chemical components of the measured points at photo b (wt. %)								
Points	**Mg**	**Al**	**Si**	**K**	**Ca**	**Mn**	**Fe**	**O**
1	11.85	-	-	-	19.82	-	-	15.71
2	9.33	-	-	-	22.20	1.58	-	15.46
3	1.41	3.67	15.13	2.40	3.80	-	5.00	25.58
4	-	-	-	-	36.35	-	-	14.51
5	-	-	-	-	35.12	-	-	14.02

Table 3. The main chemical components of the measured points at photo c (wt. %)						
Points	**Mg**	**Al**	**Si**	**Ca**	**Fe**	**O**
1	-	-	3.15	-	58.47	28.72
2	-	-	3.24	-	59.51	29.27
3	-	-	46.17	-	-	52.60
4	-	-	-	35.45	-	14.15
5	-	-	-	37.00	-	14.77
6	1.42	-	-	36.23	-	15.40

Table 4. The main chemical components of the measured points at photo d (wt. %)									
Points	**Mg**	**Al**	**Si**	**K**	**Ca**	**Mn**	**Fe**	**Ba**	**O**
1	-	-	-	-	-	45.82	-	10.39	14.56
2	-	1.55	6.08	-	-	-	47.81	-	28.85
3	-	2.52	10.23	1.33	-	-	41.95	-	32.19
4	-	4.01	12.34	2.10	-	-	34.44	-	32.85
5	-	-	-	-	-	48.02	-	12.75	15.47
6	14.05	-	-	-	19.74	-	-	-	17.12
7	1.38	11.11	16.45	-	3.39	-	28.19	-	43.00
8	-	-	-	-	-	44.40	-	11.21	14.24

Table 5. The main chemical components of the measured points at photo e (wt. %)								
Points	**Mg**	**Al**	**Si**	**K**	**Mn**	**Fe**	**Ba**	**O**
1	-	1.74	-	-	34.38	-	12.43	13.00
2	-	-	-	-	36.82	-	13.01	12.24
3	-	1.94	-	-	38.52	-	10.67	14.18
4	-	-	-	-	46.08	-	13.12	14.95
5	2.46	4.27	17.25	1.36	2.67	26.04	-	37.32
6	-	7.95	25.75	9.92	-	6.02	-	41.03

7	-	-	-	-	57.43	-	-	16.72
8	-	-	-	-	54.43	-	-	15.85
9	-	-	-	-	44.53	-	13.74	14.57

Table 6. The main chemical components of the measured points at photo f (wt. %)								
Points	**Mg**	**Al**	**Si**	**K**	**Mn**	**Fe**	**Ba**	**O**
1	1.89	3.55	16.25	1.66	-	27.92	-	35.26
2	-	-	-	0.85	45.66	-	12.30	14.90

Table 7. The main chemical components of the measured points at photo g (wt. %)											
	C	**O**	**Na**	**Mg**	**Al**	**Si**	**K**	**Ca**	**Mn**	**Fe**	**Ba**
1	18.46	15.84	0.04	0.99	2.85	16.74	2.69	2.01	0.73	37.53	2.12
2	40.54	21.13	0.90	2.37	5.53	18.65	3.02	2.61	0.43	3.38	1.44
3	11.36	13.76	-	0.94	2.26	13.49	1.77	1.04	26.11	22.93	6.33
4	10.15	13.06	0.05	0.37	1.52	8.58	1.70	0.81	38.43	18.13	7.20
5	11.38	12.69	0.03	0.65	1.66	9.22	1.31	0.96	37.66	15.40	9.03
6	11.05	13.56	0.05	0.80	3.14	10.40	2.58	1.05	32.88	18.17	6.32
7	11.20	14.10	-	0.73	2.20	11.39	1.97	1.34	31.68	19.24	6.16

Table 8. The main chemical components of the measured points at photo h (wt. %)									
Points	**Mg**	**Al**	**Si**	**K**	**Ca**	**Mn**	**Fe**	**Ba**	**O**
1	-	-	51.66	-	-	-	-	-	58.86
2	11.07	-	-	-	19.50	-	-	-	15.07
3	-	9.31	28.74	12.05	-	-	-	-	43.49
4	-	-	37.51	-	-	-	-	-	42.73

Table 9. The main chemical components of the measured points at photo i (wt. %)						
Points	**Mg**	**Si**	**Ca**	**Mn**	**Fe**	**O**
1	-	2.03	25.77	-	1.81	13.38
2	-	-	-	-	68.20	29.31
3	-	-	38.51	-	-	15.37
4	-	-	33.66	2.66	-	14.21
5	-	48.32	-	-	-	55.05
6	11.18	-	22.16	-	-	16.21

Table 10. The main chemical components of the measured points at photo j (wt. %)							
Points	**Mg**	**Al**	**Si**	**Ca**	**Mn**	**Fe**	**O**
1	-	-	6.31	5.93	-	41.25	27.29
2	-	1.38	3.89	15.83	-	29.01	24.44
3	-	-	-	36.97	-	-	14.76

SI. 5. Mineral composition of bulk samples (XRD) and in situ microXRD

Samples	Calcite	Dolomite	10 Å phyllosilicate	10.5 Å phyllosilicate	Quartz	K-feldspar	Apatite	Kutnohorite	Pyrite	Manganite	Pyrolusite
1/1/C		+								++	+++
1/1/D		+	+			+				++	++
1/2/A	+									++	+
1/2/B	+++	++		+	+						
1/2/C	+++	++		+	+					+	
2/1/A	+++	++		+	+					+	
2/1/B	+++	++		+	+						
2/1/A	++				+					++	
2/2/A	+++	++		+	++	+					
2/2/B	+++	+		++	+						
2/3/A	+++	++		+	++	+					
2/4/A	+++	++	+		+						
2/4/C	+			++	+++		++				
2/4/F	+	+	++	++	+++	+		+	+		
4/C/A	+				+						
4/C/B	++				+						
4/C/C	+++	+									
4/D/A					+						
4/D/B					+						
4/D/C		++	+++		+						
Ideal chemical formulas	$CaCO_3$	$(Ca;Mg)(CO_3)_2$	-	-	SiO_2	$KAlSi_3O_8$	$Ca_5(PO_4)_3(OH)$	$(Ca;Mn)(CO_3)_2$	FeS_2	MnO_2	MnO_2

Samples	Romanéchite	Hausmannite	Groutite	Birnessite	Goethite	XRD Amorphous Mn	Chlorite	Rhodochrosite	Zeolite
1/1/C		++			++	+		+	
1/1/D		++			+++	+			
1/2/A				+		++			
1/2/B									
1/2/C				+					
2/1/A									
2/1/B									
2/1/A						+++			
2/2/A									
2/2/B									
2/3/A									
2/4/A							+		
2/4/C									
2/4/F									+
4/C/A					+++				
4/C/B					+++				
4/C/C									
4/D/A	+++		++						
4/D/B	+++		++						
4/D/C			++						
Ideal chemical formulas	$(Ba;H_2O)(MnMn)_5O_{10}$	$MnMn_2O_4$	MnO(OH)	$(Na;Ca;K)MnMn_2O_4$ x 1,5 H_2O	FeO(OH)	-	$(Mg;Fe)_3(Si;Al)_4O_{10}(OH)_2$ x $(Mg;Fe)_3(OH)_6$	$MnCO_3$	-

Legend: +++ - main component; ++ - moderate component; + - minor component (trace)


1
2
3
a

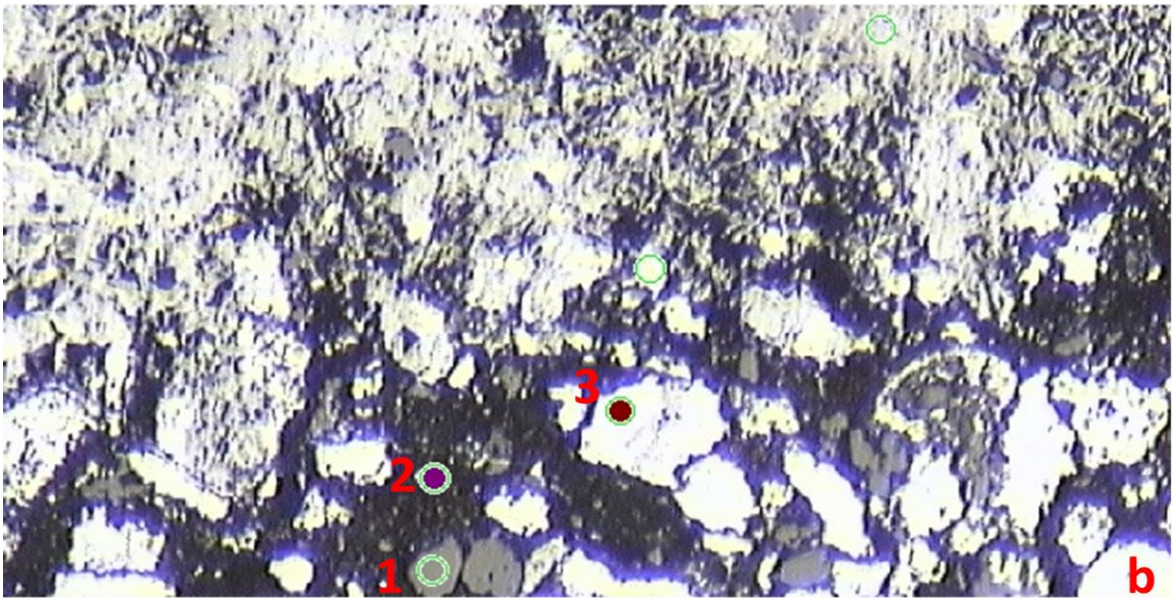
3
2
1
b

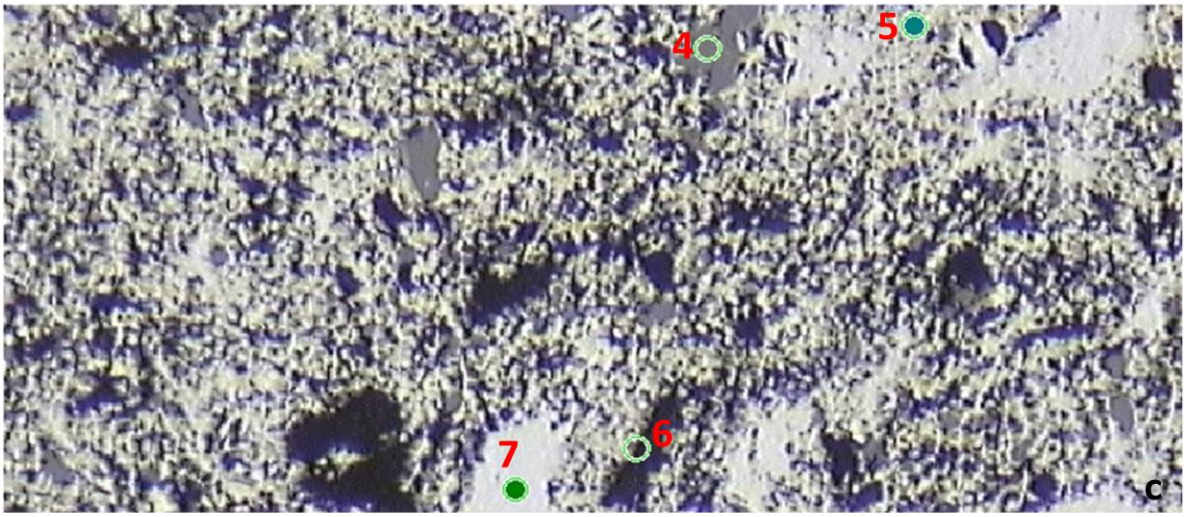
4
5
7
6
c

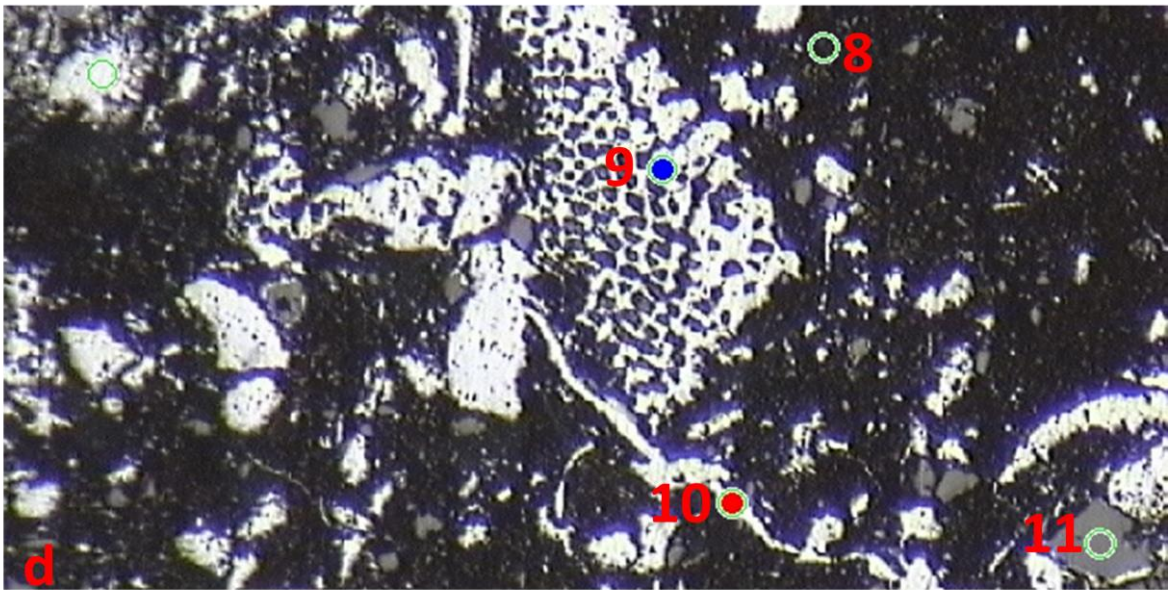
8
9
10
11
d

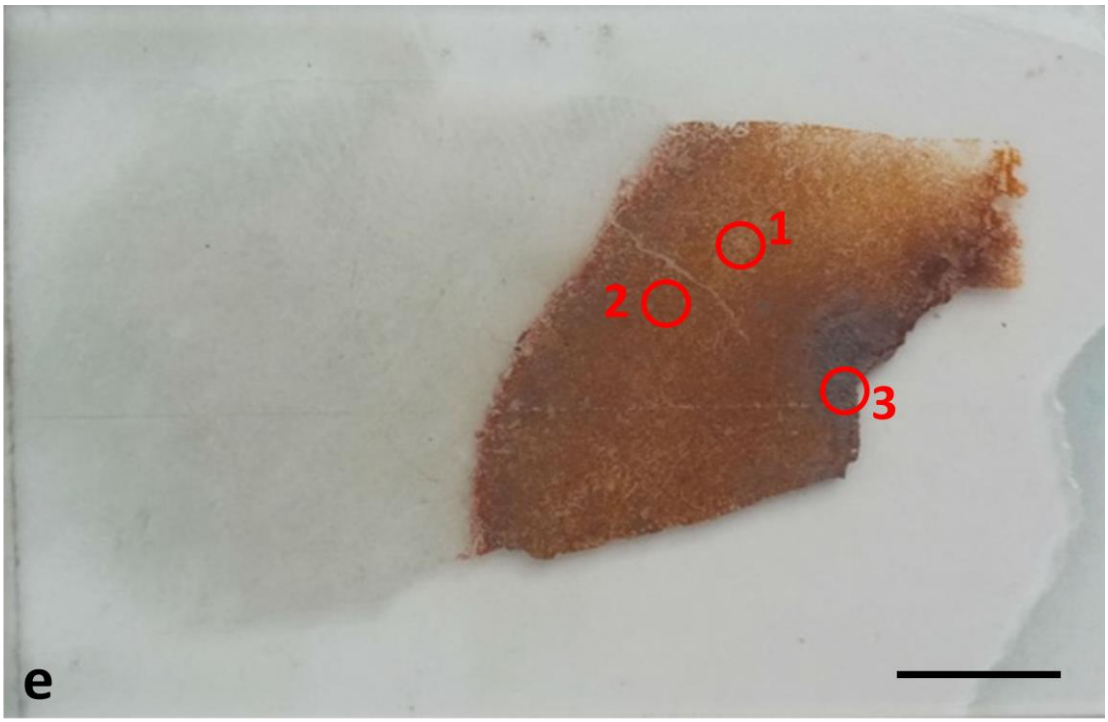
1
2
3
e

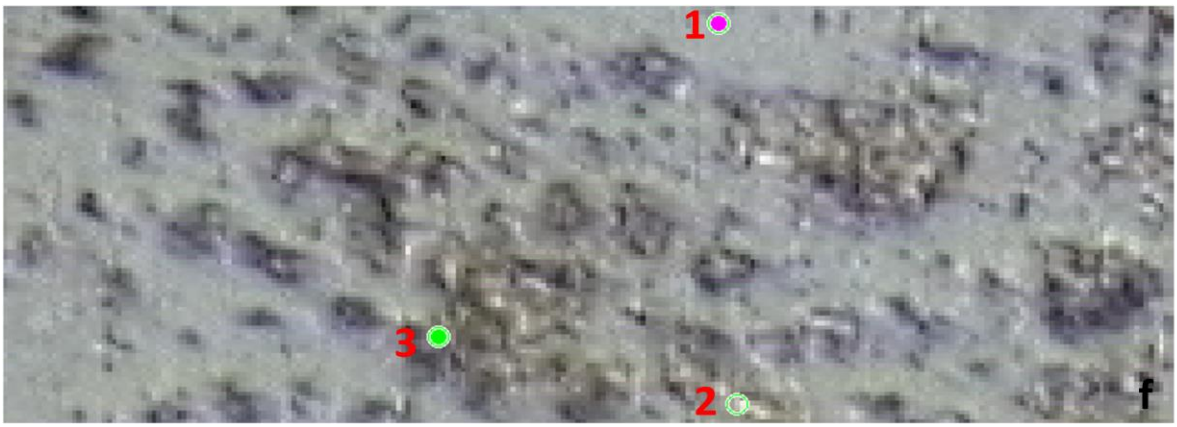

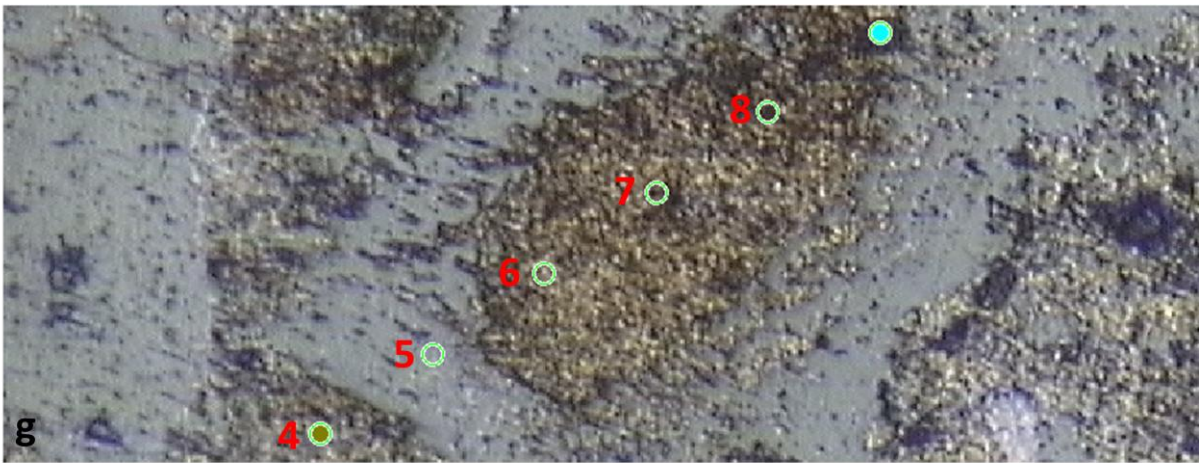

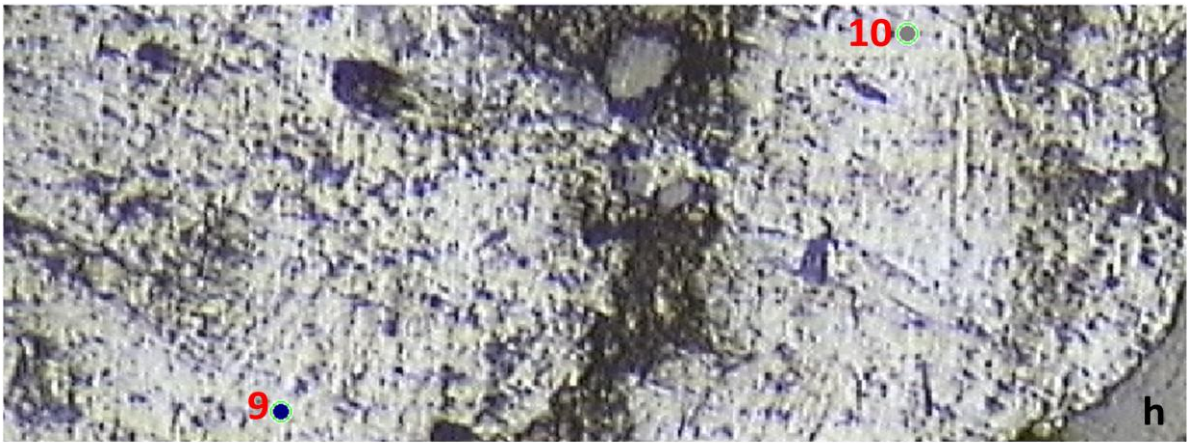

SI. 6. Measuring points on samples by FTIR
(a) thin section of sample No. 1/1/C
(b) first area on sample No. 1/1/C
(c) second area on sample No. 1/1/C
(d) third area on sample No. 1/1/C
(e) thin section of sample No. 4/C
(f) first area on sample No. 4/C
(g) second area on sample No. 4/C
(h) third area on sample No. 4/C

Detected mineral phases and organic compounds by wave length (cm^{-1}) and references
Samples No. 1/C (A) and 4/C (B)
A (photos a-d)

Measuring points	1	2	3	4	5	6	7	8	9	10	11	Ref.
Ferrihydrite	697	603			693	704		604	603			597
Maghemite	697			607	693	704			637;697	697		608-697
Rhodochrosite		709	712	708			708	708	719		708	725
Quartz (Si-O)	776								774	772		779
Akaganeite					783							786
(CO_3)										798		790
Chlorite		983		980					979			978
Clay min. (Si-O)	990											978-988
(Si-O)		1000				997						1005
(PO_4)	1102		120		1012			1116		1031		1012-1035
(C-O)					1159					1155		1170
(CO)						1358						1360-1450
(CH_2)			1452	1467		1474	1463	1422	1422			1454-1482
Amide I								1654	1654			1652
Amide II												
(C=C)	1602	1606	1602	1606		1606	1598				1602	1598
(COOH)	1733					1733					1737	1729
(CO)		2364	2357	2372		2357	2365	2364	2364			2365
(CH_2)*	2848,	2848	2866	2852		2852	2853	2852	2852		2848	2853
(CH_2)	2912	2917	2920	2924		2920	2920	2920	2920		2912	2926
(OH)				3521		3513	3509					3573

B (photos e-h)

Measuring points	1	2	3	4	5	6	7	8	9	10	Ref.
Ferrihydrite					600		603		600	600	597
Maghemite			607			607		611			608
Goethite			877		878	878	881		877	874	884
Akaganeite			663		667	667	667	659	663	659	668
Rhodochrosite	712	712		716				712			725
Quartz (Si-O)											
CO_3		795	795	795	791	795	795	791	795		790
Chlorite			975	979		979	979				978
Clay min. (Si-O)					990			986			978-988
(Si-O)									997	1001	1005
(PO_4)				1012				1024			1012-1026
(C-O-C);(C-C)								1072			1078
CO_3	1395	1399	1399	1384				1380			1397

CH2						1455	1467		1463	1463	1454-1482
(CN)(C-H)				1518/1530					1530		1526
Amide II.				1643b	1647	1632	1647	1639		1662	1658
(COOH)								1729	1737	1741	1720-29
(C-H) sym.			2845	2848	2848	2841	2845		2845	2849	2853
(C-H) asym.			2916	2920	2920	2920	2916		2924	2927	2926
(NH_4)			3077						3062	3059	3047
(C-H) arom. ring					3090	3096	3092				3090

For details see Table 1 and 4.

References

Beasley, M.M., Bartelink, Eric J., Taylor, L., Miller, R., 2014. Comparison of transmission FTIR, ATR, and DRIFT spectra: implications of assesment of bone bioapatite diagenesis. Journal of Archeological Science 46, 16-22.

Figueiredo, M. M., Martins, A. G., Gamelas, J. A. F., 2012. Characterization of bone and bone-based graft materials using FTIR spectroscopy. INTECH Open Access Publisher.

Glotch, T.D., Rossman, G.R., 2009. Mid-infrared reflectance spectra and optical constants of six iron oxide/oxyhydroxide phases. Icarus 204, 663–671.

Madejova, J., 2003. FTIR techniques in clay mineral studies. Vibrational spectroscopy 31/1, 1-10.

Madejová, J., Komadel, P., 2001. Baseline studies of the clay minerals society source clays: infrared methods. Clays and Clay Minerals 49, 410-432.

Müller, C. M., Pejcic, B., Esteban, L., Delle Piane, C., Raven, M., Mizaikoff, B., 2014. Infrared Attenuated Total Reflectance Spectroscopy: An Innovative Strategy for Analyzing Mineral Components in Energy Relevant Systems. Scientific Reports 4.

Parikh, S. J., Chorover, J., 2006. ATR-FTIR spectroscopy reveals bond formation during bacterial adhesion to iron oxide. Langmuir 22/20, 8492-8500.

RUFF Database

Udvardi, B., Kovács, I. J., Kónya, P., Földvári, M., Füri, J., Budai, F., Falus, Gy., Fancsik T., Szabó Cs., Szalai Z., Mihály, J., 2014. Application of attenuated total reflectance Fourier transform infrared spectroscopy in the mineralogical study of a landslide area, Hungary. Sedimentary Geology 313, 1-14.

Veiderma, M.I.H.K.E.L., Knubovets, R.E.N.A., Tonsuaadu, K., 1998. Structural properties of apatites from Finland studied by FTIR spectroscopy. Bulletin Geological Society of Finland 70, 69-75.

SI. 7. Raman line profile analyses

(a) photo and line profile of sample No. 3/2
(b) photo and line profile of sample No. 4/D
(c) photo and line profile of sample No. 5/1
The identified peaks of organic matter are summarized in Table 1A and B

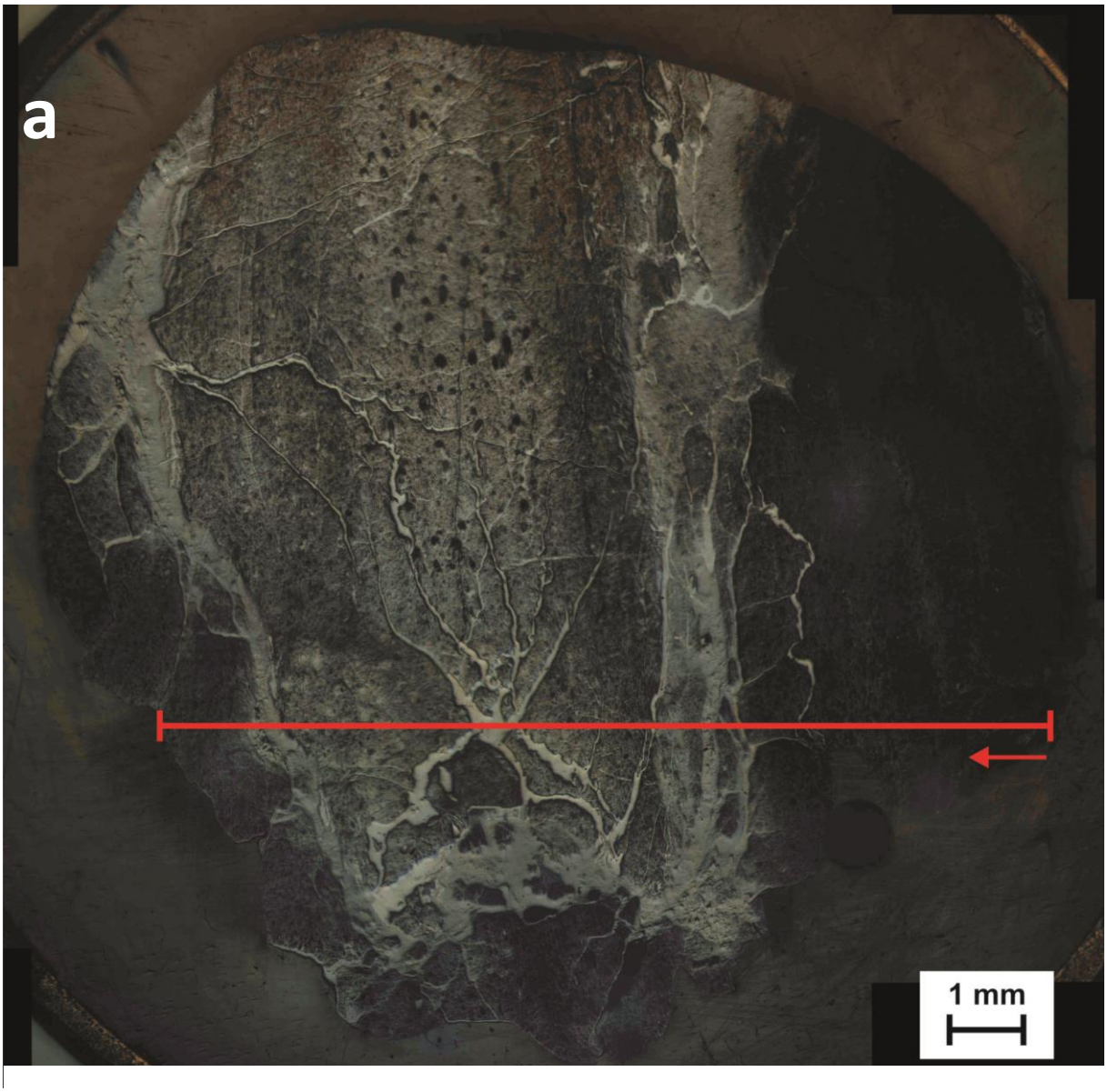
a
1 mm

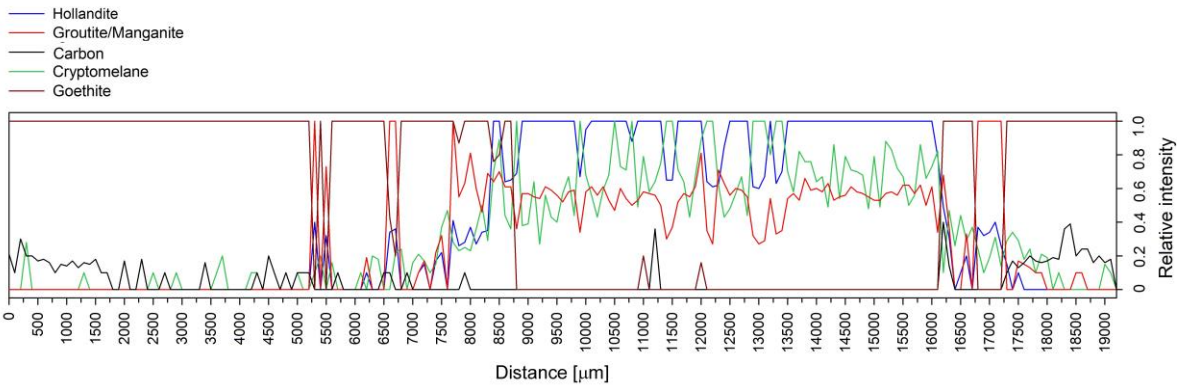
Hollandite
Groutite/Manganite
Carbon
Cryptomelane
Goethite
Relative intensity
0
0.2
0.4
0.6
0.8
1.0
0
500
1000
1500
2000
2500
3000
3500
4000
4500
5000
5500
6000
6500
7000
7500
8000
8500
9000
9500
10000
10500
11000
11500
12000
12500
13000
13500
14000
14500
15000
15500
16000
16500
17000
17500
18000
18500
19000
Distance [μm]

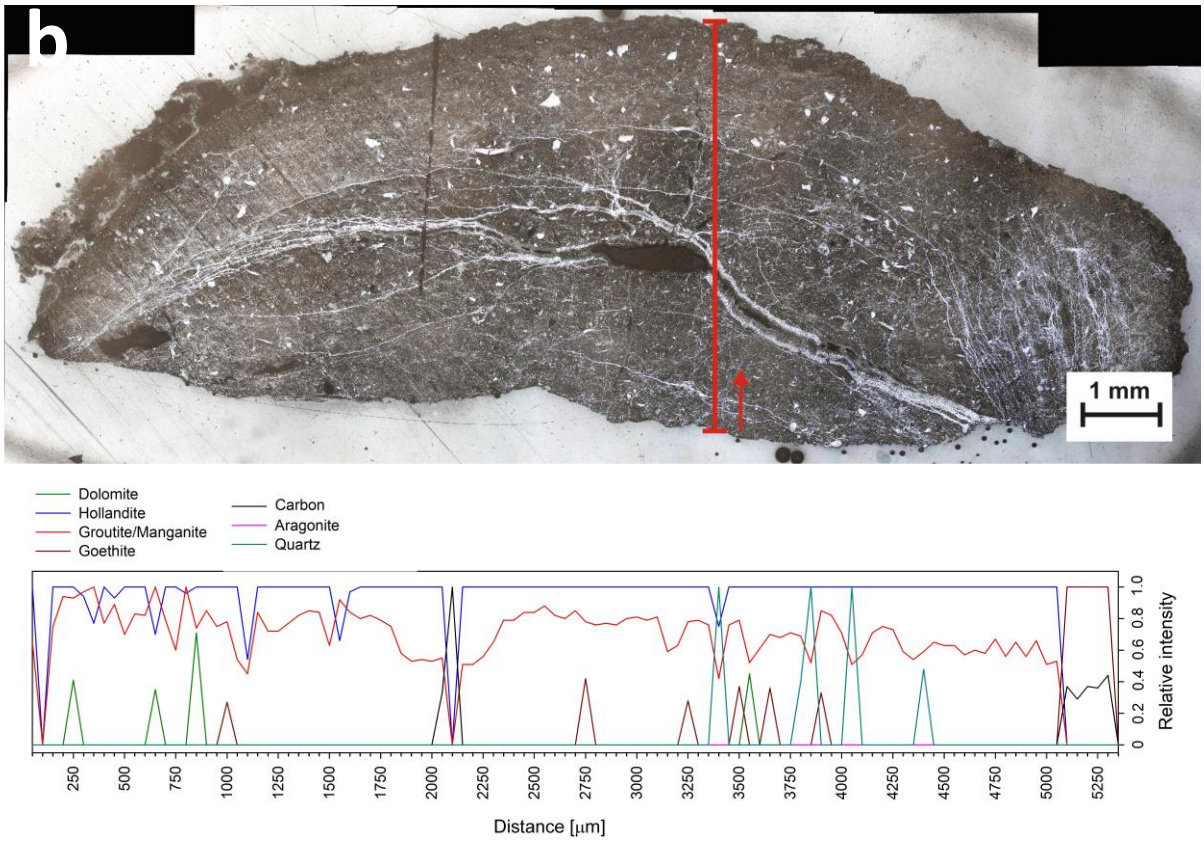
b
1 mm
Dolomite
Hollandite
Groutite/Manganite
Goethite
Carbon
Aragonite
Quartz
Relative intensity
0
0.2
0.4
0.6
0.8
1.0
250
500
750
1000
1250
1500
1750
2000
2250
2500
2750
3000
3250
3500
3750
4000
4250
4500
4750
5000
5250
Distance [μm]

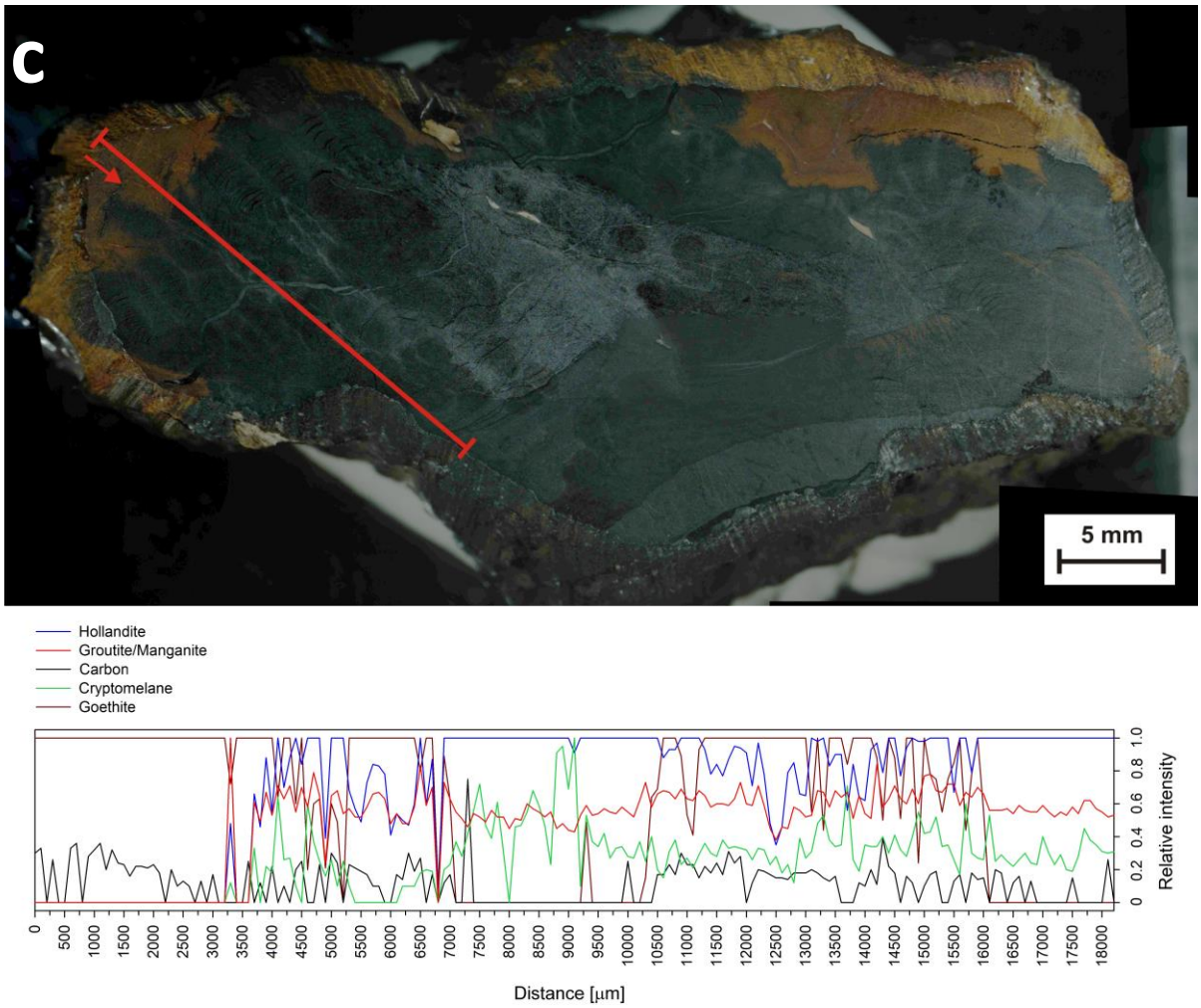
C
5 mm

Hollandite
Groutite/Manganite
Carbon
Cryptomelane
Goethite
Relative intensity
0
0.2
0.4
0.6
0.8
1.0
0
500
1000
1500
2000
2500
3000
3500
4000
4500
5000
5500
6000
6500
7000
7500
8000
8500
9000
9500
10000
10500
11000
11500
12000
12500
13000
13500
14000
14500
15000
15500
16000
16500
17000
17500
18000
Distance [µm]

Table 1A. The identified peaks of organic matter (sample No. 4/D)

1	2	3	4	5	Result	Reference
679	684	679,	679	668	(C-H)	682
	942				CH_3/CH_2	936/950
			974	972	CH_3	972
1330	1326	1325	1315	1300	Organic C in CO_3 group	1300
1596	1600	1597	1608	1608	amorphous C	1600

Legend: The bold numbers are the measured points, the other numbers are the identified and reference peaks (cm^{-1})

136	109	106	94	89	77	71	51	4	Result	Reference
581	579	580	586						aromatic ring (C-C)	579-590
638		637			638			637	ring (C=C)	639
							645		PAH (C-C-C)	642
								819	(C-H)	
						924			CH2	926
								937	CH3/CH2	936/950
						1078			(C-H)	1080
1185								1184	(C=C)	1180
1298							1294	1292	CH2	1287
						1340			organic carbon in CO_3	1300
	1363	1363	1364						heterocyclic aromatic (C=C) (C-N)	1368
1381								1380	heterocyclic aromatic (C=C) (C-N)	1379
		1487							CH2/CH3	1487
	1526					1522			(C=C)	1518
					1580				aromatic ring (C-C-H)	1580
							1597		PAH	1590
			1602						amorphous carbon	1600
1608s	1603	1606		1606				1608	fluorene (aromatic CH)	1607
						1631			PAH	1624

Legend: The bold numbers are the number of the measured points, the normal numbers are the identified and reference peaks (cm^{-1}), PAH – Polycyclic aromatic hydrocarbons

SI. 8. Sediment accumulation and rock formation hierarchy for Mn, Fe, and clay minerals (bold text shows important aspects)

Mn

The Úrkút manganese carbonate deposit was originally an oxide deposit

Structural hierarchy

	Accumulation of sediment		Origin of rock
Sediment/ rock	**Primary formation conditions – palaeoenvironment (pH, Eh, salinity)** Low T aquatic system, normal marine salinity neutrophylic (6-8), obligatory oxic (Eh: +0.4-+1.0 V) conditions, aerobic system with dissolved oxygen, DO > 2 mL/L) Mn-oxide-hydroxide, Fe-oxide-hydroxide, C_{org}, clay matrix, rare debris **microbial - Step 1. (chemolithoautotrophic cycle)** ---------- **Evidence** $\delta^{18}O_{PDB}$ -5.85- +1.61 ‰; µm-scale microbial lamination-determined by chemical analyses, caused by mineralized microbial layering (Mn(II)-microbial oxidation	Sediment composition: Mn-oxide-hydroxide, Fe-oxide (goethite), organic matter, celadonite, smectite	**Burial + early diagenesis (lithification)** fine grained Ca-rhodochrosite – microbially mediated Mn-reduction, heterotrophic suboxic metabiolism neutrophylic (6-8), suboxic oxic (Eh: +0.4-+1.0 V) conditions, with dissolved oxygen through dysoxic (DO 0.2–2.0 mL/L), to suboxic (DO 0–0.2 mL/L) conditions. **microbial - Step 2. (heterotrophic cycle)** ---------- **Evidence** $\delta^{13}C_{PDB}$ -16.8 ‰; C_{org} contribution to carbonate (Ca-rhodochrosite); amorphous organic matter remnants; fine-grained siderite, pyrite	Mn-carbonate ore
Texture		Fine grained, µm-scale microbial lamination, caused by mineralized microbial layering (Mn(II)-microbial oxidation)		Double lamination (mm-scale Fe and µm-scale Mn) + preserved microbial biomat texture, fine grained
Matrix main complex mineralogy (also accompanying minerals are important) authigenic minerals		Goethite in biomats, clay minerals, among them celadonite (Fe-mica), smectite, C_{org}, rare debris (K-feldspar, quartz, etc.)		Goethite, celadonite, nontronite, siderite, pyrite, remnants of C_{org}, rare debris (K-feldspar, quartz, etc.) Preserved manganite
Micro-mineralogy (authigenic minerals)		Mn-bearing minerals: 1. δMnO_2, manganite, todorokite **Authigenic mineralization**		Mn-bearing minerals: 1. Ca-rhodochrosite
Microbial mediation		Chemolithoautotrophic Mn(II) oxidation microbial mediation (Mn(II) $6Mn^{2+} + 0.5O_2 + CO_2 + 16H_2O \rightarrow CH_2O + 6MnOOH_3 + 12\ H^+$		heterotrophic suboxic microbial Mn-reduction via organic matter decomposition microbial mediation – **Ca-rhodochrosite** formation $(Mn^{4+} \rightarrow Mn^{2+})$ $CH_2O + 8H^+ + 4MnO_2 \rightarrow Mn^{2+} + CO_2 + 11H_2O$ $Mn^{2+} + CO_2 + H_2O \rightarrow MnCO_3 + 2H^+$ **Early diagenetic mineralization**
Atom, ion chemistry				
Isotopes (bulk)		$\delta^{18}O_{PDB}$: -5.85- +1.61 ‰		$\delta^{18}O_{PDB}$:-5.85 - +1.61 ‰; $\delta^{13}C_{PDB\ av}$: -16.8 ‰

Time

Fe

Structural hierarchy

Sediment/ rock	**Primary formation conditions - palaeoenvironment** Low T aquatic system, normal marine salinity, neutrophylic (6-8), suboxic (Eh: +0.3 V) conditions, with dissolved oxygen through dysoxic (DO 0.2–2.0 mL/L), to suboxic (DO 0–0.2 mL/L) conditions. Fe-oxide-hydroxide,Mn-oxide-hydroxide, C_{org}, clay matrix, rare debris **microbial - Step 1. (chemolithoautotrophic cycle)** --- **Evidence** $\delta^{18}O_{PDB}$ -5.85- +1.61 ‰; filamentous with an inner pearl-necklace-like texture; micromorphology, type of FeOB metabolism; giving a mm-scale lamination, MMPSS*, series of Fe-rich biomats	Sediment composition: Mn-oxide-hydroxide, Fe-oxide (goethite), organic matter, celadonite, smectite	**Burial + early diagenesis (lithification)** 1. Preserved goethite – microbial texture 2. fine-grained siderite – microbially mediated Fe-reduction. heterotrophic suboxic metabiolism fine-grained siderite; microbially mediated Fe-reduction; heterotrophic suboxic metabolism (Eh: 0-+0.2 V; with dissolved oxygen through dysoxic (DO 0.2–2.0 mL/L), to suboxic (DO 0–0.2 mL/L) conditions. **microbial - Step 2. (heterotrophic cycle)** 3. pyritized biomat – pyritization of goethitic filaments – sulfate reduction – anoxic/anaerobic microbial metabolism (Eh: -0.2 V, pH: 6-8) **3. microbial – Step 3. (heterotrophic cycle)** --- **Evidence** $\delta^{13}C_{PDB}$ -16.8 ‰; C_{org} contribution to carbonate (siderite); amorphous organic matter remnants; fine-grained siderite. pyrite	Mn-carbonate ore
Texture		Fine grained, filamentous microbial forms		Double lamination (mm-scale Fe and μm-scale Mn) + preserved microbial biomat texture, fine grained
Matrix main complex mineralogy (also accompanying minerals are important) authigenic minerals		Mn-oxide-hydroxide (δMnO_2, manganite-MnOOH, todorokite, clay minerals, among them celadonite (Fe-mica), smectite, C_{org}, rare debris (K-feldspar, quartz, etc.)		Ca-rhodochrosite, celadonite, nontronite, siderite, pyrite, remnants of C_{org}, rare debris (K-feldspar, quartz, etc.)
Micro-mineralogy (authigenic minerals)		Fe-bearing minerals: 1. Ferryhydrite - goethite-(hematite) in microbial texture 2. Fe-mica and smectite (details in separate table) **Authigenic mineralization**		Fe-bearing minerals: 1. Bed I: preserved **goethite** biomats 2. Bed II: heterotrophic suboxic microbial Fe-reduction via organic matter decomposition microbial mediation – **siderite** formation ($Fe^{3+} \rightarrow Fe^{2+}$) $CH_2O + 8H^+ + 4Fe(OH)_3 \rightarrow Fe^{2+} + CO_2 + 11H_2O$ $Fe^{2+} + CO_2 + H_2O \rightarrow FeCO_3 + 2H^+$ 3. **pyrite** - pyritized goethitic biomats in sulfate reduction zone 4. **celadonite** and **smectite** (**nontronite**, details in separate table) **Preservation and authigenic mineralization**
Microbial mediation		Chemolithoautotrophic FeOB microbial mediation (Fe(II) $6Fe^{2+} + 0.5O_2 + CO_2 + 16H_2O \rightarrow CH_2O + 6Fe(OH)_3 + 12\ H^+$		
Atom, ion chemistry				
Isotopes (bulk)		$\delta^{18}O_{PDB}$: -5.85- +1.61 ‰		$\delta^{18}O_{PDB}$:-5.85 - +1.61 ‰; $\delta^{13}C_{PDB\ av}$: -16.8 ‰

Accumulation of sediment | **Origin of rock**

Time

Clay minerals

Structural hierarchy

	Accumulation of sediment		Origin of rock	
Sediment/ rock	**Primary formation conditions - palaeoenvironment** Low T aquatic system, normal marine salinity, neutrophylic (6-8), suboxic (Eh: +0.3 V) conditions, with dissolved oxygen through dysoxic (DO 0.2–2.0 mL/L), to suboxic (DO 0–0.2 mL/L) conditions. Celadonite, smectite, Fe-oxide-hydroxide, Mn-oxide-hydroxide, C_{org}, rare detrital debris --- **Evidence** $\delta^{18}O_{PDB}$ -5.85- +1.61 ‰; fine grained green clay matrix, because of diagenetic, and microbial overprinting the primary textural features (probable biogenic character) is not observable	Sediment composition: Mn-oxide-hydroxide, Fe-oxide (goethite), organic matter, celadonite, smectite	**Burial + early diagenesis (lithification)** 3. Preserved celadonite and partly smectite suboxic conditions (Eh: 0-+0.2 V; with dissolved oxygen through dysoxic (DO 0.2–2.0 mL/L), to suboxic (DO 0–0.2 mL/L) conditions. 2. nontronite formation accompanied by goethite pyritization in anoxic/anaerobic microbial metabolism (Eh: -0.2 V, pH: 6-8) --- **Evidence** $\delta^{13}C_{PDB}$ -16.8 ‰; fine-grained green clay matrix, pyrite	Mn-carbonate ore
Texture		Fine-grained matrix		Double lamination (mm-scale Fe and µm-scale Mn) + preserved microbial biomat texture, fine grained
Matrix main complex mineralogy (also accompanying minerals are important) authigenic minerals		Mn-oxide-hydroxide (δMnO_2, manganite-MnOOH, todorokite, clay minerals, among them celadonite (Fe-mica), smectite, C_{org}, rare debris (K-feldspar, quartz, etc.)		Ca-rhodochrosite, goethite, siderite, pyrite, remnants of C_{org}, manganite, rare debris (K-feldspar, quartz, etc.)
Micro-mineralogy (authigenic minerals)		Clay minerals: 1. celadonite 2. smectite **Authigenic mineralization**		Clay minerals: 1. celadonite preserved 2**. nontronite** **Preserved and authigenic mineralization**
Microbial mediation		Celadonite --- Smectite organo-mineralization		Celadonite --- Smectite organo-mineralization
Atom, ion chemistry				
Isotopes (bulk)		$\delta^{18}O_{PDB}$**:** -5.85- +1.61 ‰		$\delta^{18}O_{PDB}$**:**-5.85 - +1.61 ‰; $\delta^{13}C_{PDB\ av}$: -16.8 ‰

Highlights mandatory

- We studied Fe-Mn-oxide of feeder and mound zone of footwall of Úrkút Mn ore deposite.
- Bulk organic matter analysed first time using GC-MS, FTIR-ATR and Raman spectroscopy.
- Metal-bearing fluids infiltered the unconsolidated micritic limemarl.
- Mn oxides appear with Fe oxides in laminated, micro-stromatolite-like structures.